Hybrid Metal/Covalent Organic Frameworks for Solar Fuel Conversion

sizhuo yang
Marquette University

HYBRID METAL/COVALENT ORGANIC FRAMEWORKS FOR SOLAR FUEL CONVERSION

By

Sizhuo Yang

A Dissertation submitted to the Faculty of the Graduate School,

Marquette University,

in Partial Fulfillment of the Requirements

for the Degree of Doctor of Philosophy

Milwaukee, Wisconsin

May 2020

ABSTRACT

HYBRID METAL/COVALENT ORGANIC FRAMEWORKS FOR SOLAR FUEL CONVERSION

Sizhuo Yang

Marquette University 2020

Due to the harsh environment issues such as air pollution and global warming and global energy crisis raised by using fossil fuels, it is urgent to find an alternative sustainable energy source. How to utilize solar energy-the most clean and abundant energy source on earth is challenging. Convert solar energy to clean fuel energy like H_2 or hydrocarbons is ideal energy conversion strategy. Thus, design new materials for hydrogen generation or CO_2 reduction have attract researcher's attention.

The present study focuses on two types of materials of interest, the first of which is Metal Organic Frameworks (MOFs), including enhancing the light harvesting ability of ZIF-67 via energy transfer from RuN3, electron transfer in hybrid Pt-Ru-UIO-67, Co-Ru-UIO-67 and Ce-TCPP MOF. Since MOFs have potential to be used as photocatalytic materials for artificial photosynthesis due to their unique porous structure and ample physicochemical properties of the metal centers and organic ligands in framework, we also examine the photocatalytic activity of these materials for hydrogen generation. By using the combination of X-ray absorption spectroscopy (XTA), transient absorption spectroscopy (TA), the fundamental roles of hybrid MOF that plays during catalysis were uncovered. The second type of materials that we are interested in is Covalent Organic Frameworks (COFs). A 2D COF with incorporated Re complex was designed, which can efficiently reduce CO_2 to form CO under visible light illumination with high electivity (98%). More importantly, using advanced transient optical and X-ray absorption spectroscopy and in situ diffuse reflectance spectroscopy, three key intermediates that are responsible for charge separation (CS), the induction period, and rate limiting step in catalysis were found, which is expected to provide important guidance on designing efficient materials for CO_2 reduction, thus facilitating the development of solar to fuel conversion

ACKNOWLEDGEMENTS

Sizhuo Yang

Time flies, throughout my academic career in Marquette as a PHD candidate, I'm extremely grateful to all of those with whom I have had the pleasure to work during last five and half years. I would like first to extend my deepest gratitude to my adviser, Prof. Jier Huang, for her patient advise during my graduate studies. She convincingly guided and encouraged me to be professional and do the right thing even when the road got tough. Without her persistent help, the goal of my work would not have been realized. I would also like to express my sincere appreciation to the members of our group, for helping me with night shift of synchrotron X-ray absorption experiments in Argonne, without which my work could not be completed.

I'd like to acknowledge the assistance from the excellent faculty in chemistry department that provide a positive and collaborative environment for research. I also wish to thank my committee members, Dr. Reid, Dr. Gardinier and Dr. Timerghazin, for gave me extensive professional guidance and taught me a great deal about scientific research in general. I am also grateful to my friends denan, Yilin and Lingzi, who helped me a lot in daily life, especially at the beginning of my graduate study that I don't have a car.

Many thanks to the staff at Advanced Photon Source of Argonne national lab, specially Xiaoyi Zhang and Cunming Liu, for helping us set up the X-ray absorption experiment, which is really important to our research.

Nobody has been more important to me in the pursuit of this project than the members of my family. I would not be the person that I am without the continues love and support from my parents Zhixian Yang and Jianfang Chen. The view of world, the view of life and values they instilled in me makes me who I am, I thank them for this and much more, words cannot express the depth of my gratitude for the life that I was given by these two, let me experience the beauty of life.

I would like to thank my wife Kun Yan, it would be impossible to do any of these without her encourage and huge sacrifice. There is so much I want to say but so little can be expressed. Although she is not a chemist, she's always the first to hear my difficulty in experiments, and also my presentation. Thank you for your laugh, your patience and the countless hard times you accompanied me to go through.

Finally, I would like to thank my baby girl Emma, you are the angel sent from heaven, every little bit progress of your growth makes my life more meaningful.

TABLE OF CONTENTS

LIST OF TABLES

LIST OF FIGURES

derivative spectra (b). The K-space (c) and Fourier-transformed R-space (d) spectra compared with data as open points and FEFF fits as solid lines. Inset of panel A shows enlarged pre-edge feature.

Figure 5.4 Full EXAFS spectra of Co-UIO-67(bpy) and Co-Ru-UIO-67(bpy) (a) and graphic of EXAFS fit model (b). (Grey=C, Blue=N, Pink=Co, Green=Cl, Red=O, White=H). Hydrogens were excluded from FEFF calculation.

Figure 5.5 Time profile of H_2 generation under optimized condition: without H_2O (black) or TEOA (red), Ru-UIO-67(bpy) (green) and Co-UIO-67(bpy) (pink) as control.

Figure 5.6 Optimization of light-driven H_2 evolution reaction. (a) The amount of H_2 produced using different solvent and sacrificial donor. (b) The amount of H_2 produced as a function of TEOA concentration. (c) The amount of H2 produced as a function of H2O concentration. (d) The amount of H2 produced as a function of Co:Ru ratio.

Figure 5.7 (a) Time profile of H2 production by Co-Ru-UIO-67(bpy) under 447 nm LED illumination at 9 mW in the presence of TEOA (0.3mL) and H2O (0.4 mL) in acetonitrile solution (3 mL). (b) Recycling of Co-Ru-UIO-67(bpy) catalyst after multiple 5 h experiments. (c) Commonly accepted catalytic pathway for photoinduced H2 generation with molecular photosensitizer (PS) and catalysts.

Figure 5.8 XANES region (a) and R-space EXAFS fit figures (b) for Co-Ru-UIO-67(bpy) compared to ex situ sample after 20 hours of catalysis.

Figure 5.9 Femtosecond TA spectra of Ru-UIO-67(bpy) (a) and Co-Ru-UIO-67(bpy) (b). (c) The comparisons of the GSB recovery and ES decay kinetics between Ru-UIO-67(bpy) and Co-Ru-UIO-67(bpy). The GSB recovery kinetics for both Ru-UIO-67(bpy) and Co-Ru-UIO-67(bpy) were inverted for better comparison.

Figure 5.10 Stern-Volmer plot (b) was obtained by using unquenched emission signal divided by the quenched signal (a) against the concentration of quencher. From the slope and the lifetime of Ru-UIO-67, which we extracted from ns-TA GSB decay kinetics (c), the reductive quenching rate is 3.423x105 M-1S-1. Under the optimized condition with TEOA concentration of 0.568 M, the estimated time constant for reduction quenching is 5.14 μs.

Figure 5.11 (a) Time profile of H_2 production by Co-Ru-UIO-67(bpy) under 447 nm LED illumination at 9 mW in the presence of TEOA (0.3 mL) and H2O (0.4 mL) in acetonitrile solution (3 mL). The inset is the duration of induction period as a function of Co-Ru-UIO-67(bpy) concentration and LED power. (b) In situ XANES spectra of Co-Ru-UIO-67(bpy) as a function of irradiation times. The insets are enlarged regions I and II. (c) The offset first derivative of in situ XANES spectra. (d) In situ XANES spectra of Co-Ru-UIO-67(bpy) after LED was switched off to observe change back to

Chapter 1.

INTRODUCTION

1.1 Need for sustainable energy source

Today, more than 80% of the world's energy is supplied by fossil fuels.[1] However, considering the rapid increase of energy demand in the world, the exhausting fossil fuels in the foreseeable future will heavily hinder the sustainable development. Meanwhile, burning fossil fuels also cause environmental issues such as air pollution and emission of carbon dioxide which is one of the major greenhouse gases causing global warming. As a result, the exploration of sustainable clean energy sources to replace fossil fuels is of great interest and is one of the most hot research topics nowadays. Among different renewable energy sources such as wind, biomass, tidal energy and geothermal, solar energy is one of the most promising line for development because of its abundance and sustainability. Sunlight provides 3×10^{24} J of energy per year, which is far beyond the total current global energy consumption (13.7 TW).[2] As a result, efficient conversion of solar energy to other energy sources that can be used by humans offers great chance to address the problems of energy shortage and air pollution. There are two main solar energy conversion strategies, i.e. solar-to-fuel conversion and solar-to-electricity conversion. Direct conversion of sunlight to fuel is an attractive way because the energy can be stored in chemical bonds such as H_2 through water splitting process or high-energy carbon compounds through CO_2 reduction. This strategy mimics the photosynthetic system in nature and is named artificial photosynthesis.[3-4] Direct

conversion of solar energy to electricity is another common approach where the electricity from a photovoltaic cell can be used directly or stored in a secondary device such as batteries.[5]

1.2 Solar to Fuel Conversion through Artificial photosynthesis

Photosynthesis is the chemical process by which plants convert energy from the sun into the form of hydrocarbon that act as fuels. The whole process can be break down into two stages- the light and dark reactions. Organic energy molecules (ATP and NADPH) are generated during light reaction as fuel to produce hydrocarbons in the dark reaction. Figure 1.1 illustrates the photosynthesis process in nature, which undergoes light harvesting, charge separation, water oxidation and fuel production to complete the circle.[6] In photosystem II (PS II), antenna pigment molecules (mostly chlorophyll and/or carotene) absorb sunlight and transfer the energy to the reaction center where charge separation occurs.[7] The positive charges are used to oxidize water, while the electrons are passed to photosystem I (PS I) via cytochrome bf. In PS I, a second light-harvesting process occurs and provides additional energy to the electrons, which raises electrons to a more negative redox potential. This is followed by electron transfer to ferredoxin and reduce $NADP^+$ to NADPH. The transport of electron from water to $NADP^+$ generate a pH gradient across the thylakoid membrane. This proton motive force is used to drive the synthesis of ATP, which works together with NADPH to produce carbohydrate fuel.[8-9]

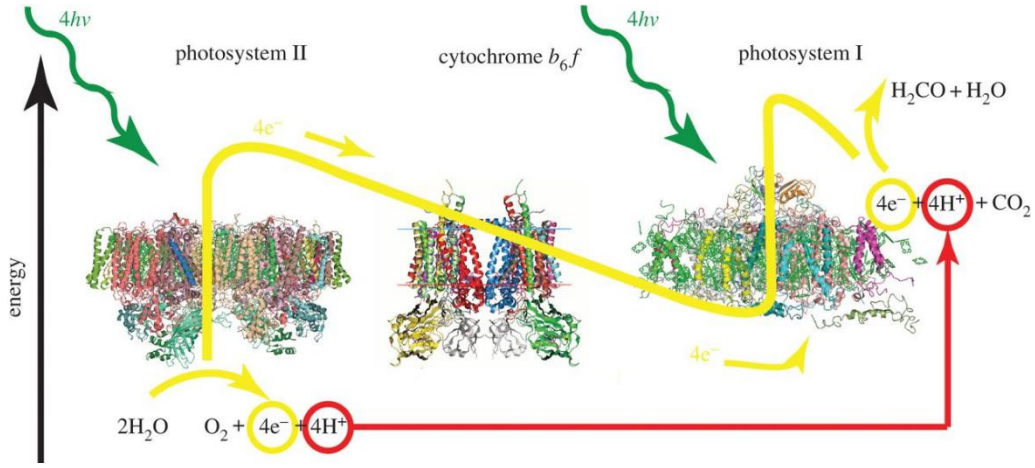

Figure 1.1 A schematic diagram of natural photosynthesis showing light absorption, charge separation, water oxidation and fuel production. The path of the yellow line indicates the approximate energy of the electrons in analogy to the Z -scheme. [6]

Motivated by the natural photosynthesis, researchers have developed artificial systems to perform similar photochemical reactions. Two types of strategies are commonly used for artificial photosynthesis systems. One of them (Figure 1.2a) is featured by a single component photosensitizer (either molecular dye or semiconductor) with electron donors on one side and electron acceptors on the other side. The absorption wavelength is tunable by modifying the dye structure or designing the electronic structure of semiconductor. To complete the whole process, electron donor and acceptor need to meet two requirements. First, the energy level of donor (acceptor) should between water oxidation (reduction) potential and reduction (oxidation) potential of the photosensitizer. Second, fast electron transfer must occur before the excited photosensitizer returns to its ground state. However, there are several drawbacks of this single photosensitizer setup. Considering the water oxidation (+1.23V vs. NHE) and reduction potential (0V vs. NHE), there are limited choice of

photosensitizers. Meanwhile, only a fraction of sunlight can be used

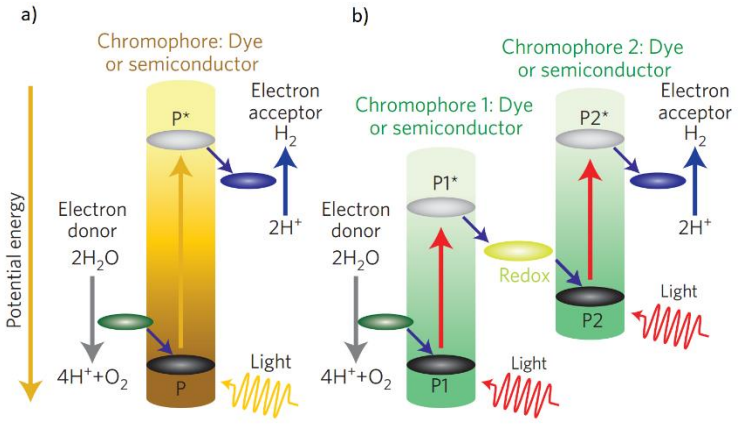

Figure 1.2 Artificial photosynthesis charge separation process: (a) one step and (b) two step reactions.[10]

to drive such reaction simultaneously. An alternative strategy that includes two photosensitizers is shown in Figure 1.2b. This strategy is more analogous to natural photosynthesis, where two chromophores absorb different part of the solar spectrum to drive water oxidation and H_2 generation reaction in tandem. In this way, the number of photons absorbed by the artificial photosynthesis system can be maximized.[11] However, it is more difficult to control the kinetic balance of electron transfer between the two steps. Hence, many efforts have been focused on the half reactions such as hydrogen generation reaction (HER), oxygen generation reaction (OER), and CO_2 reduction reaction to gain insight of these half reactions before the overall process of artificial photosynthesis can be understood.[12-14]

There are three key steps in artificial photosynthesis systems, 1) appropriate light harvesting materials that can absorb significant portion of sunlight, 2) efficient charge

separation and sequential charge migration to the reaction centers, 3) utilization of charge carriers to drive photocatalytic reactions. The first example of artificial photosynthesis can be traced back to 1972 and reported by Fujishima,[15] where TiO_2 was used as photoanode to perform water splitting reaction. Since then, various systems for artificial photosynthesis have been developed in the past decades. These systems can be mainly divided into two categories, homogeneous molecular system and heterogeneous semiconductor based photocatalytic systems. Homogeneous solution-based systems comprising molecular photosensitizer (PS) and catalysts have naturally attracted much attention because of their merit in synthetic control over functional tunability and selectivity (Figure 1.3).[16-18] However, their limitation on stability and efficiency remain a major challenge. In contrast, heterogeneous systems such as Ti-, Zr-, Nb-, Ta-, W-, Mo- based oxides[19-22] have shown beneficial features in long-term durability and high catalytic activity. However, these materials not only lack design flexibility but also suffer from the difficulty of characterizing their mechanistic functions, rendering poor understanding of the origins behind their remarkable catalytic efficiency.

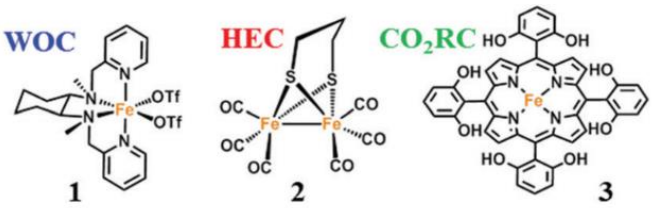

Figure 1.3 Molecular structures of Fe complexes 1, 2, and 3 as molecular catalysts for water-oxidation, hydrogen-evolution and CO2 reduction. [23]

1.3 Metal Organic Frameworks as Emerging Photocatalytic Materials

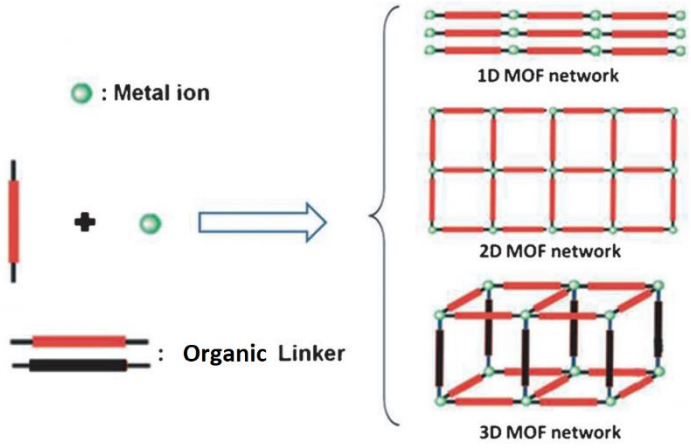

Figure 1.4 Design strategy for MOFs with 1D, 2D, and 3D network structures. [24]

To integrate the beneficial features and overcome the drawbacks of homogeneous and heterogeneous photocatalytic systems, it is not surprising that metal organic frameworks (MOFs) and covalent organic frameworks (COFs) have attracted intensive attention as photocatalytic materials owing to their capability to incorporate photosensitizer and/or catalysts to the frameworks with retained heterogeneity.

Metal Organic Frameworks (MOFs) represent a novel class of porous crystalline materials constructed from metal-containing units [secondary building units (SBUs)] and organic linkers as bridge.[25-28] The assembly of these networks are illustrated in Figure 1.4. The metal centers act as lattice nodes and are held in place by coordinating to rigid organic linkers. In many cases, the frameworks are stable enough to remove the solvent or other guest molecules, which makes crystallinity and porosity the main characteristics of MOFs. The pores in the MOFs can be tuned by replacing the ligand with different length to form 1D, 2D or 3D networks, which results in the high surface

area of such materials. The versatility of organic linkers and metal nodes, together with large surface area and the porosity make MOFs an ideal material for various applications, including gas storage, drug delivery, catalysis, molecular sieves,[29-31] as well as photoactive materials for H_2 generation and CO_2 reduction.[32-33] (Figure 1.5)

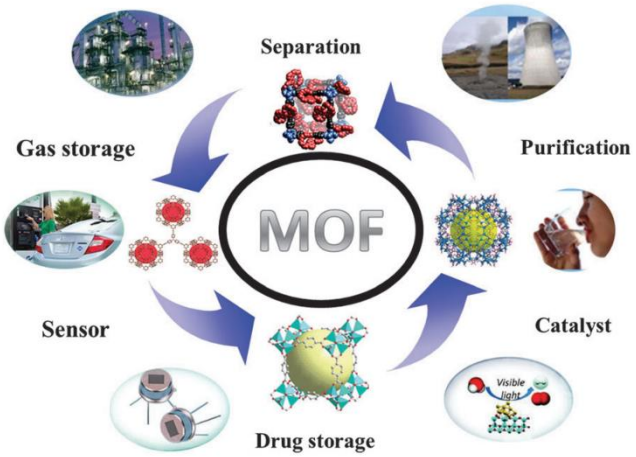

Figure 1.5 Potential applications of MOFs for gas storage and separation, drug delivery, chemical sensor, catalysis and so on. [34]

1.3.1 MOFs as light harvesting materials for artificial photosynthesis

Inspired by natural photosynthesis, two strategies have been developed to enhance light harvesting property of MOFs: (1) incorporating light-harvesting chromophores into MOFs framework and (2) introducing light harvesting guest materials to the cavity or on the surface of MOFs (Figure 1.6).

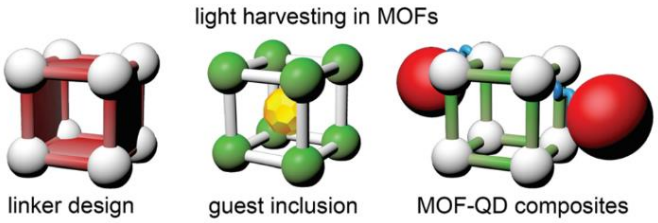

Figure 1.6 Approaches for the enhancement of light-harvesting properties of MOFs. Yellow and red spheres represent the guest molecule and QD, respectively. [35]

Organic or metal organic chromophores as building blocks

Since light absorption by the photosensitizer is the first step for rational design of a photocatalytic system, it is highly desirable to have building blocks in MOFs that can directly absorb light in the visible region.

The linkers in MOFs are generally aromatic units functionalized with carboxylate groups for metal-ligand coordination. The aromatic units often have intense absorption above 250 nm or can extend to the visible region due to n-π* and/or π- π* transition. Therefore, it is possible to have MOFs with visible light responses. Indeed, MOFs with incorporated organic and metal-organic chromophores that demonstrate visible light response such as porphyrin, phthalocyanines and polypyridyl metal complexes have been reported and many of them showed good photocatalytic performance. Since these organic linkers are stabilized in MOFs, it has been shown that their non-radiative decay rates was reduced, which caused the increase of their fluorescence lifetime. In addition, the molecules are closely packed in MOF framework which enables charge transfer among organic ligands, resulting in the shift

of their spectra, the broadening of the emission, and loss of fine structure. By means of the appropriate substitution of aromatic linkers, it is possible to shift photo-responses of MOFs towards visible region.

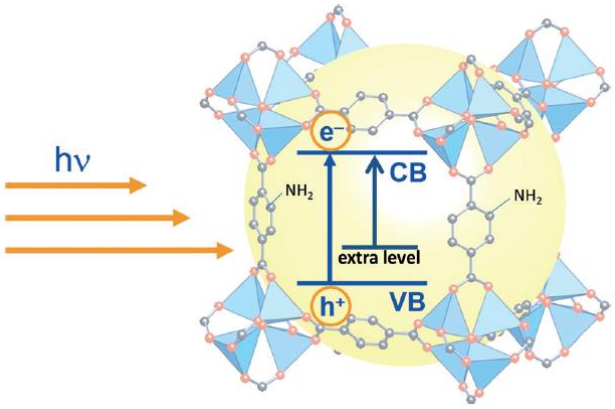

Figure 1.7 An illustration of the effect of -NH_2 substitution which adds an additional energy level to the band gap of MOFs. [36]

One example that illustrates the influence of substitution on the optical properties of MOFs is the use of the –NH_2 group (Figure 1.7) as a substitute of 1,4 benzenedicarboxylic acid (bdc), where it introduces a new band around 400 nm in the aminated MOF. [36-38] Similar strategy has also been used in uio-66 Zr-MOF. By modifying linkage with -NH2 functional group, uio-66-NH2 shows absorption ability in visible region, which can be used as photosensitizer for H_2 evolution reaction.[39] Moreover, it is possible to incorporate a complementary pair of chromophores as struts, which may result in energy transfer from the incorporated chromophore and relay energy to MOFs to enhance the light absorption ability. As shown in Figure 1.8, Hupp's group reported energy transfer between different ligands of the so-called BOP

MOF.[40] By replacing dipyridyl boron dipyrromethene in BOB MOF with tetra-acid porphyrin, strut to strut energy transfer occurs within the framework, which shifts the emission of BOP MOF from green to red.

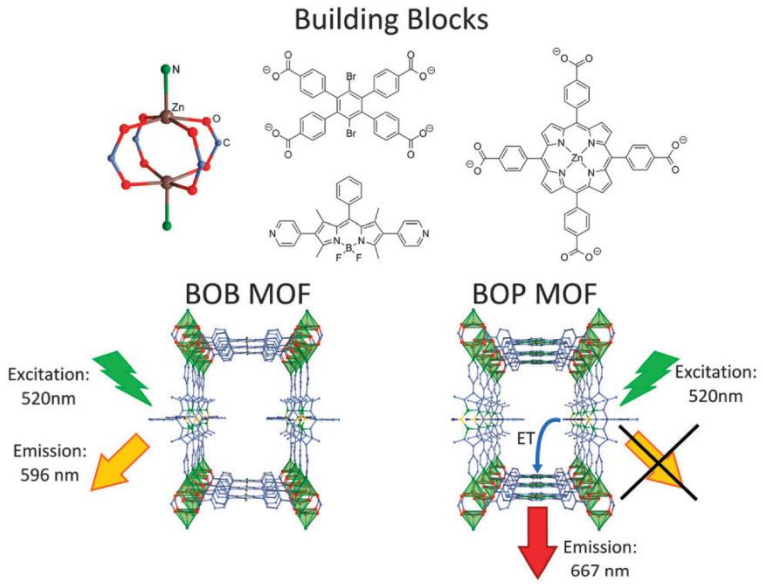

Figure 1.8 BOB and BOP MOF: building blocks, structures and photophysical processes of excitation, emission and energy transfer (ET). [40]

Lanthanide based MOF is another type of photoactive MOFs which are widely used in biological analysis. Lanthanide ions are characterized by a gradual filling of the 4f orbitals, from $4f_0$ to $4f_{14}$. The valence 4f electrons of trivalent lanthanide ions are well shielded from the environment by the outer core 5s and 5p electrons. The lanthanide ions suffer from weak light absorption due to the forbidden f-f transitions, making the direct excitation of metals inefficient. This problem can be overcome by coupling ligands that can participate in energy transfer processes, known as antenna effect. The mechanism of photoactive process within lanthanide based MOF is

comprised of three steps: (1) light is absorbed by the organic ligands around the lanthanide ions; (2) energy is transferred from the organic ligands to lanthanide ions through intramolecular energy transfer; (3) luminescence is generated from the lanthanide ions via radiative process. Figure 1.9 shows an example of Eu based MOF, where energy transfer occurs from ligand to Eu after photoexcitation of dicarboxylic ligand, which is followed by emission from Eu^{3+}.[41]

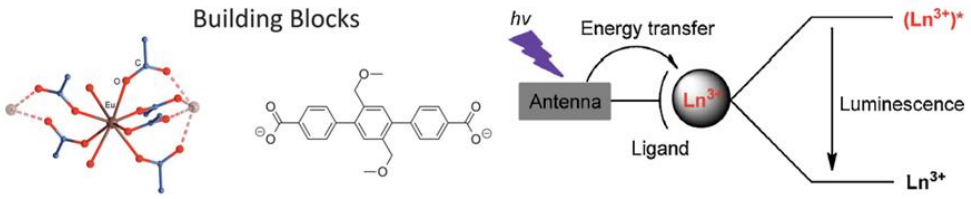

Figure 1.9 Antenna effect of Ln MOF. [41]

Encapsulating light harvesting guest nanoparticles in the cavity of MOFs

Owing to their large pore size, MOFs can offer a unique platform to encapsulate luminescent species. A variety of nanoparticles, including Au, Ag, Pt, CdTe, Fe_3O_4, NaYF4,[42-44] have been successfully encapsulated to MOFs. For example, semiconductor nanoparticles (CdSe quantum dots) with emission bands that have overlap with the absorption bands of MOFs have been encapsulated to F-ZnP and DA-ZnP MOF. Monitoring the change of kinetics of quantum dot emission when quantum dots were bound to the surface of MOF, the energy transfer from quantum dots to MOF occurs with 80% efficiency (Figure 1.10).[45] Another example is that Jiang's group developed a core-shell MOF-5-ZnO, which shows a blue shift in green

emission and intensity reduction in UV emission compared with that of pure ZnO arrays.[46]

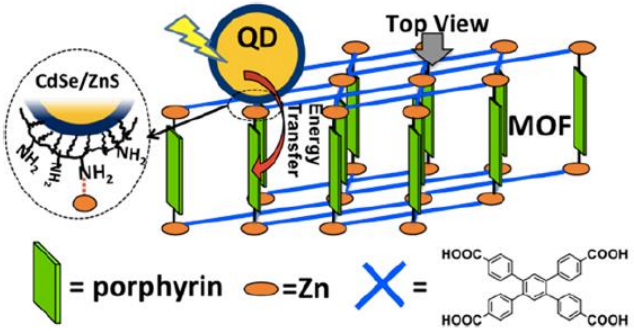

Figure 1.10 Schematic diagram of a QD−MOF complex. [45]

1.3.2 MOFs as photocatalysts

Recently, the use of MOFs as catalysts for various reactions have become an emerging field. Similar to photoactive MOFs, three strategies are used to introduce catalytic sites to the framework: (1) Linker functionalization by in-situ growth or post

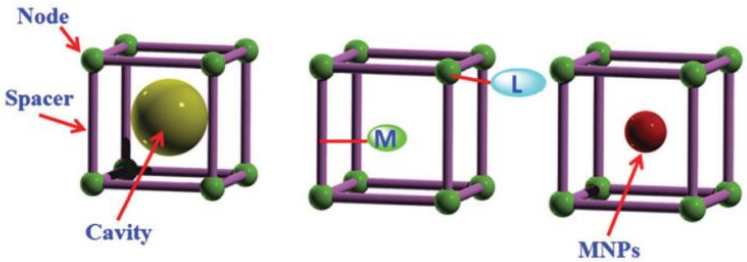

Figure 1.11 The potential catalytic sites of MOFs. [47]

synthetic modification, (2) Use metal nodes (clusters) as active sites, (3) Nanoconfinement of particles within the pore of MOFs as catalysts (Figure 1.11).

Examples of the applications of these MOF based systems for organic reactions include H-KUST-1 and chromium terephthalate MIL-101 for cyanosilylation,[48] Yb-RPF-5 for hydrodesulfurization,[49] IRMOF-1 and IR-MOF-8 for the alkylation of aromatics,[50] photooxidation of alcohols to the corresponding aldehydes by NH_2-MIL-101,[51] and core-shell Au@ZIF-8 for photoreduction of nitrobenzene[52] etc. In addition to catalyze organic reactions, MOFs can also be used as photocatalysts for H_2 generation and CO_2 reduction. Examples of MOFs as photocatalysts for H_2 generation and CO_2 reduction are summarized in Table 1.

Table 1.1 Summary of photocatalytic reactions on H_2 generation and CO_2 reduction with various MOFs.

Photocatalyst	Light source (sacrificial	Photoactivity
Photocatalytic H_2 evolution		
Al-ATA-Ni MOF	UV–Visible	36 μmol h^{-1}(30mg) [53]
Pt@MOF-1 or Pt@MOF-2	450W Xe-lamp (TEA),	3400 or 7000 TON [54]
$H_2TCPP[AlOH]_2(DMF_3$-	300W Xe lamp (EDTA),	200 μmol $g^{-1}h^{-1}$ [55]
MOF-253-Pt	300W Xe lamp (TEOA),	3000 μmol [56]
Pt/NH2-UiO-66	200W Xe-doped Hg lam	2.8 mL [57]
RhB/UiO-66(Zr)-100*	300W Xe lamp (TEOA)	33.9 μmol $g^{-1}h^{-1}$ [32]
Pt-UiO-66-30	300W xenon lamp (20%	37 μmol [58]
Fe_2O_3@TiO_2/Pt	Xe lamp (TEA)	0.8 μmol [59]
Co@NH2-MIL-125(Ti)	500W Xe/Hg lamp	37 μmol [60]
CdS/MIL-101(10)/Pt	Xe (10 vol% lactic acid)	75.5 mmol h^{-1} [61]
Ni/MIL-101	Xe (0.5 m ammonia borane)	TOF: 3238 h^{-1} [62]
UiO-66- [FeFe] (dcbdt)$(CO)_6$	Blue LED (ascorbic acid)	3.5 μmol (0.59 μmol catalyst)
Photocatalytic CO2		
NH_2-MIL-125(Ti)	Xe lamp (CH_3CN/TEOA)	8.14 μmol $HCOO^-$ [64]
NH_2-UiO-66	500W Xe lamp (TEOA)	13.2 μmol $HCOO^-$ [65]
MIL-101(Fe) or NH_2-MIL-	300W Xe lamp(CH_3CN/	59 or 178 μmol $HCOO^-$ [33]
MOF-253-Ru$(CO)_2Cl_2$	Xe lamp (CH_3CN and TEOA)	0.67 μmol $HCOO^-$ [66]
Cp*Rh@UiO-67	300 W Xe lamp (TEOA)	47 TON [67]
CdS/Co-ZIF-9	300 W Xe lamp (TEOA)	CO (50.4 μmolh^{-1}) [68]

ZIF-8/Zn_2GeO_4	500 W Xe lamp	2.44 μmol g^{-1} CH_3OH[69]
UiO-67 BPDC with Ru (II)	Xe (TEOA)	30.4 $HCOO^-$, 10.9 CO [70]

All these examples show the great potential of MOFs in photocatalytic application. However, majority of these works are centered on their catalytic performance and stability rather than fundamental mechanism. As light harvesting, charge separation and the utilization of separated charges carriers for catalytic reaction are key steps in photocatalytic systems, it is important to fully understand the roles that MOFs play during catalysis to further improve the catalytic performance.

1.4 Covalent Organic Frameworks as Novel Photocatalytic Materials

Although MOFs are suitable for photocatalysis due to the multifunctionality, their stability under catalytic condition remains a challenge. Covalent Organic Frameworks (COFs) have attracted attention as another class of porous materials owing to their high porosity and chemical stability. In contrast to MOFs, COFs comprise of pure organic building blocks linked via strong covalent bonds.

1.4.1 Design of Covalent Organic Frameworks

The design of Covalent Organic Frameworks considers the topology because it describes the connectedness of the material. The concept of topology originated from Euler in 18th century, which is given as the polyhedron formula:[71]

$$V-E+F=2 \qquad (1)$$

Where V, E and F are the number of vertices, edges, and faces of a polyhedron, respectively. The left side of the equation 1 is called Euler characteristic (χ) and can be represented as

$$\chi = V-E+F \qquad (2)$$

For any convex polyhedron χ =2. The study of topology helps to understand the connection between the building blocks of COFs which gives more insight of the pore structure of materials.

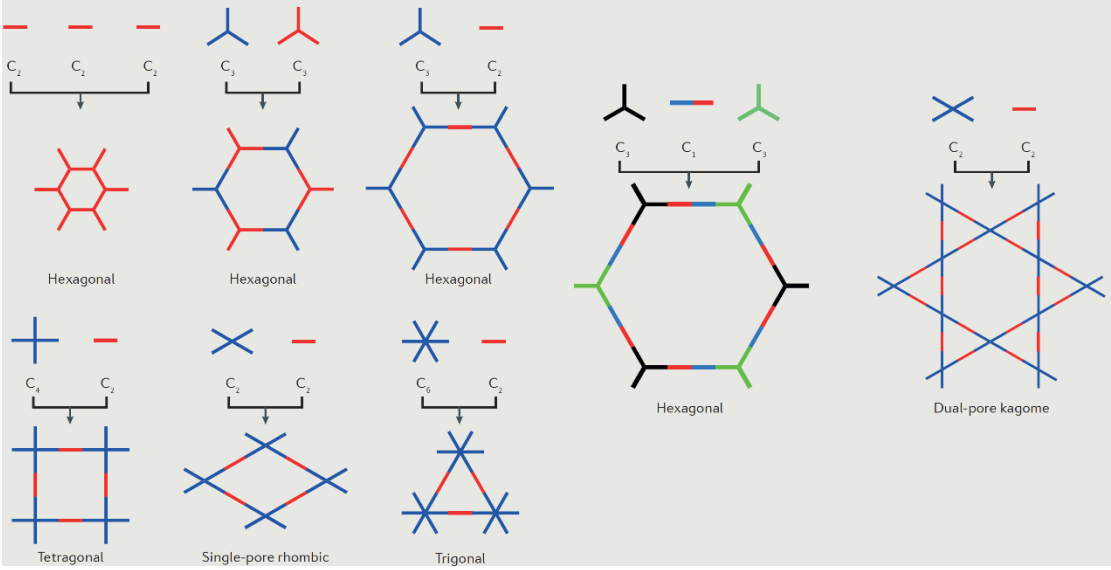

Figure 1.12 Topology diagrams of COFs representing the relationship between the pore structures and blocks. [72]

The polygon structure of COFs usually consists of knots and linkers, Figure 1.12 shows the topology diagrams. The combination of C3 knots and C2 linkers (C3+C2) always form hexagonal structure.[73-74] Using other combinations such as self-condensation of C2 units or C3+C3 linkers also generate hexagonal COFs,[75-76] where the only difference is that C2 units are located at knot while C3 units occupy the

vertices. Hexagonal topology can also be built from 3-component system C3+C1+C3 linker. Among all the topologies, the combination of C4+C2 and C6+C2 usually exhibit extended π conjugation,[77-80] where the former leads to tetragonal frameworks while the later has trigonal structure with highest density of π units and smallest pore size. Exploring tetragonal and hexagonal topology are useful in designing mesopore COFs, whereas trigonal geometry usually leads to microporous frameworks. The development of C2+C2 linkers can generate two types of different structures: the single-pore rhombic topology[81-82] and dual-pore kagome shape[83-84] with different pore volume in the materials.

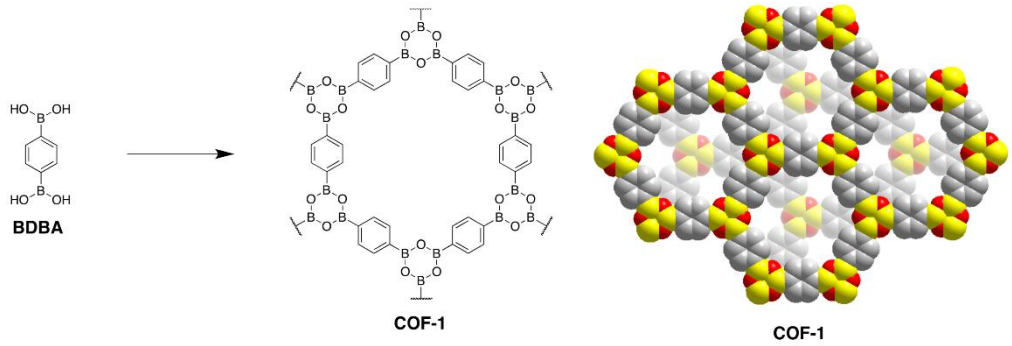

Figure 1.13 Self-condensation of boronic acid to form COF. Structure of one pore and space-filling diagram of COF-1. [85]

Unlike amorphous polymers, COFs are crystalline materials with short and long-range order. To ensure the extended crystallinity, chemical reactions involved in the formation of linkages should be reservable, which can thus provide self-healing ability for COFs to correct the defects. COFs were pioneered by Yaghi's group. As shown in Figure 1.13, first COF [85] was synthesized by the self-condensation of 1,4-

phenylenediboronic acid (BDBA) in the form of B_3O_3 rings to produce staggered structure with surface area of 711m^2/g and 15Å pore diameter. In addition to self-condensation, boronic acids can also react with catechols to form boronate esters. Those boronate COFs are thermally stable but degrade in the presence of H_2O and alcohols. To enhance the structure stability, COFs have been synthesized via C-N linkage. The first example is COF-300 (Figure 1.14) [86], in which imine condensation of tetra-(4-anilyl) methane (TAM) and terephthaldehyde (BDA) results in crystal

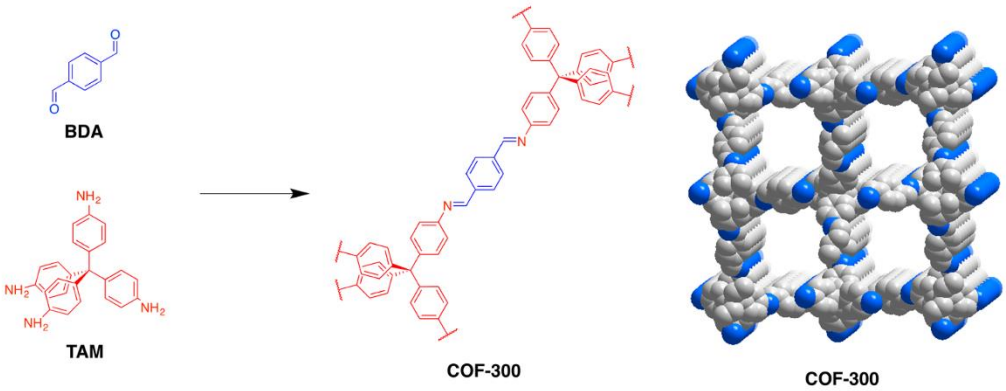

Figure 1.14 Example of first imine COF, the structure of COF-300 fragment. [86]

structure with 5-folder interpenetrated dia topology and surface area of 1360m^2/g. Imine COFs show less crystallinity compared to that of boronate COFs, whereas the stability enhanced significantly in H_2O and alcohols. Similar strategies have been applied between aldehyde and hydrazide or hydrazine to form hydrazone-linked COFs or azine-linked COFs.[81, 87] Hydrazone-linked COFs usually shows remarkable stability because of the hydrogen bonding between oxygen in the alkoxyl chains and hydrogen in N-H unit, which stabilized the whole framework. Other COFs prepared

via C-N bond include squaraine-linked COFs, phenazine-linked COFs, imide COFs and triazine COFs (Figure 1.15).[88-90]

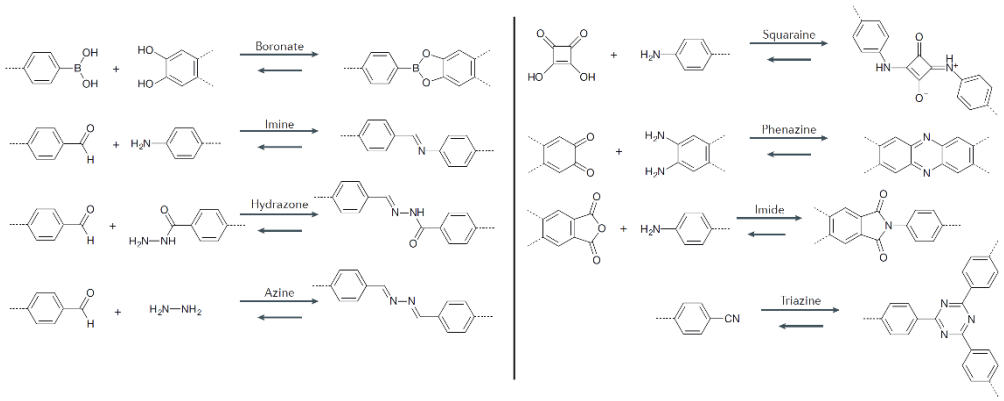

Figure 1.15 Diversity of linkages for the formation of COFs. [72]

The formation of C=C bonds has also been reported to prepare carbon-conjugated COFs. As shown in Figure 1.16, Jiang's group reported the first sp^2 c-COF

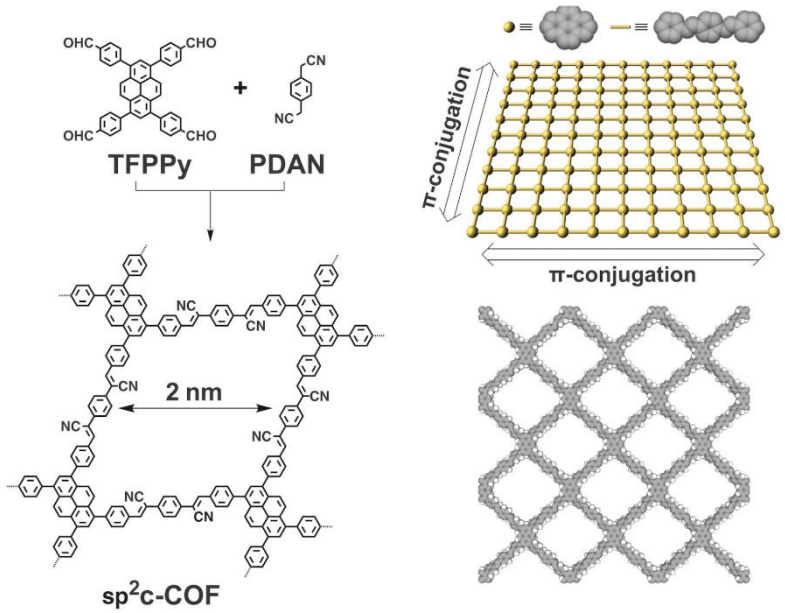

Figure 1.16 Chemical and lattice structures of a crystalline porous sp^2 c-COF. [91]

constructed from aryl acetonitriles and aromatic aldehydes via Knoevenagel

condensation reaction.[91] Another strategy is forming olefin linkage via aldol condensation between 1,3,5-triazine and aryl aldehydes.[92] Compare to imine, hydrazine and azine-linked COFs and sp^2 c-COFs afford fully π conjugation which enables efficient exciton migration over the framework. Due to the low polarity of the C=C bonds, sp^2 c-COFs shows pronounced stability even in acid or basic condition.

1.4.2 Covalent Organic Frameworks for catalysis

In recent years, applying COFs for catalytic reaction becomes a hot topic. For example, Wang's group reported imine-linked COF LZU-1 for Suzuki-Miyaura coupling reaction (Figure 1.17).[93] By post treatment with $Pd(OAc)_2$, Pd^{2+} can be inserted between two layers of LZU-1. The hybrid Pd/COF LZU-1 showed excellent yield of Suzuki coupling reaction, which is attributed to the easy access to the active sites of COFs and the fast diffusion of reactants within large pores. Other than C-C coupling, COFs have been used in various catalytic reactions include oxidation reactions,[94] ethylene oligomerization reaction,[95-96] reduction reactions,[97] asymmetric synthesis[98] et al.

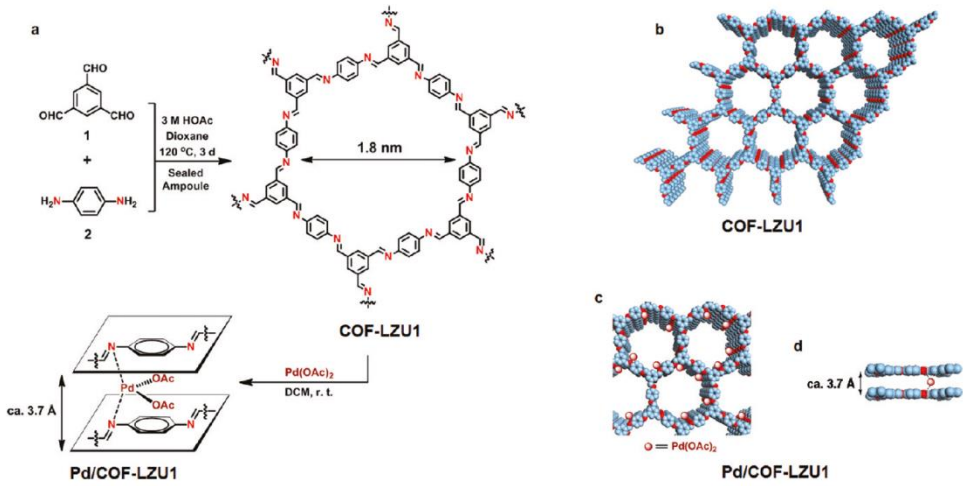

Figure 1.17 Schematic representation for the synthesis of COF-LZU1 and Pd/COF-LZU1 materials (a). Proposed structures of COF-LZU1 (b) and Pd/COF-LZU1 (c, d) possessing regular microporous channels (diameter of∼1.8 nm), simulated with a 2D eclipsed layered-sheet arrangement. [93]

In addition to the chemical reactions, light absorption ability in visible region and easy treatment of ligands make COFs an ideal platform for photocatalysis. However, only few COFs have been applied in solar to fuel conversion. Lotsch's group synthesized a series of azine-linked COFs for H_2 generation with Pt as cocatalysts.[99] The performance of H_2 evolution was related to the number of nitrogen atoms of N_x core in COFs. The same group also reported the use of N_2-COF as photosensitizer and chloro(pyridine)cobaloxime as co-catalyst for H_2 evolution with H_2 generation rate 782 μmol/h/g.[100] By modifying the linker of N3-COF, Cooper's group reported sulfone-containing N_3-COF with high HER efficiency and good stability up to 50 hours.[101] More recently, several sp2 c-COFs have been exploited for H_2 generation. Zhang's group reported 2D sp^2 g-Cx-N3-COF for visible light water splitting with apparent quantum efficiency of 4.84% at $\lambda = 420$ nm.[102] Jiang's group studied the key

factors that affect the HER efficiency of sp^2 c-COFs.[103] The frameworks can combine stability, crystallinity, porosity, and π conjugation in one material, which improve the light harvesting and charge migration during catalysis.

In nearly all those examples, hybrid MOFs/ COFs with built in photosensitizer and catalysts simultaneously are rare. Moreover, there is no clear understanding of the actual role of MOFs/COFs play, not to mention the structure function relationship of MOFs/COFs during catalysis. The further development of hybrid MOFs/COFs for solar to fuel conversion is largely hampered by the lack of fundamental study of photophysical events after excitation and the difficulty of controlling the structure precisely during catalysis.

1.5 Summary of Research

The research in my graduate study aims to develop hybrid MOFs/COFs materials and unravel their structure-function relationships for their applications in solar energy conversion. In chapter 3, I will discuss the adsorption of a molecular chromophore (RuN3) onto the surface zeolitic imidazolate frameworks (ZIF-67), where the absorption of the former compensates the latter. We show that energy transfer can occur from RuN3 to ZIF-67 with ~86.9% efficiency, which facilitated the light harvesting ability of ZIF-67. More importantly, this RuN3/ZIF-67 hybrid system exhibits significantly enhanced photocatalytic activity for H_2 production from water, which can be attributed to efficient energy transfer from RuN3 to ZIF-67 However, this system has relatively low efficiency compared to other Co based photocatalysts

for H_2 generation and poor stability due to the degradation of RuN3 photosensitizer.

In order to further improve the H_2 evolution efficiency and overcome the stability issue of the molecular photosensitizers, we designed two hybrid MOF systems (Pt-Ru-UIO-67 and Co-Ru-UIO-67) as single-site catalysts for H_2 generation with built in photosensitizer and molecular catalysts, which were discussed chapter 4 and chapter 5. Using the combination of optical transient absorption spectroscopy and transient X-ray absorption spectroscopy/in-situ X-ray absorption spectroscopy, we not only unraveled the photophysical events happened after photoexcitation but also captured the key intermediate species in the catalytic cycle, providing important insight into the catalysis mechanism of these single-site MOFs photocatalysts. In chapter 6, we report the fundamental photophysical study of a porphyrin-based Ce-TCPP MOF using the combination of optical transient absorption (OTA) and X-ray transient absorption (XTA) spectroscopy. We found that ultrafast electron transfer occurs from porphyrin ligand to Ce center, resulting in the formation of long-lived charge separated state with ligand-to-metal cluster charge transfer (LCCT) character. These findings imply the large promise of using Ce-TCPP as light harvesting and charge separation materials for solar energy conversion.

In chapter 7, a newly designed 2D COF with incorporated Re complex was reported. This hybrid system can efficiently reduce CO_2 to form CO under visible light illumination with high electivity (98%). More importantly, using advanced transient optical and X-ray absorption spectroscopy and in situ diffuse reflectance spectroscopy, three key intermediates that are responsible for charge separation (CS),

the induction period, and rate limiting step in catalysis were found. This study not only demonstrates the potential of COFs as next generation photocatalysts for solar fuel conversion but also provided unprecedented insight into the mechanistic origins for light-driven CO_2 reduction.

Chapter 2

EXPERIMENTAL AND CHARACTERIZATION

In this chapter, the experimental details of sample preparation and characterization will be discussed. The samples in these works include RuN_3 sensitized zeolitic imidazolate frameworks (ZIFs), Ce-TCPP MOF, hybrid UIO-67 MOFs with incorporated photosensitizers and catalysts, and Re-COF. Standard characterization techniques used to determine the structure and morphology of these samples include powder X-ray diffraction (XRD), scanning electron microscope (SEM), Fourier-transform infrared (FT-IR) spectroscopy. Advanced time-resolved spectroscopic techniques including time-resolved optical and X-ray absorption spectroscopy were used to examine the charge separation and structural dynamics associated with it. Furthermore, in situ spectroscopic techniques such as in situ diffuse reflectance spectrum and X-ray absorption spectrum that were used to probe the catalytic mechanism during catalysis. The photocatalytic activities of these hybrid ZIFs, MOFs and COFs for H_2 production or CO_2 reduction were also performed, where their experimental details are discussed here.

2.1. Characterization and General Procedure.

UV-Visible absorption and diffuse reflectance spectra were taken using an Agilent 8453 spectrometer equipped with Internal DRA 2500 accessories. Powder XRD data

were collected by using Rigaku Miniflex II XRD diffractometer with Cu Kα radiation. Scanning Electron Microscope (SEM) were taken by JSM 6510-LV (JEOL Ltd, Tokyo). Fourier-transform infrared (FT-IR) spectroscopy were measured with Nicolet iS5 FT-IR spectrometer. Gas adsorption isotherms were performed by using the surface area analyzer ASAP-2020. N_2 gas adsorption isotherms were measured at 77K using a liquid N_2 bath. To make MOF films, the mixture of MOF with ethanol (1mg/0.5mL) was sonicated for 2 hours and then dispersed evenly on piranha-etched glass. The films were dried in air.

Femtosecond Transient Optical Absorption Spectroscopy (OTA).

The OTA spectroscopy is based on a regenerative amplified Ti-Sapphire laser system (Solstice, 800nm, < 100 fs FWHM, 3.5 mJ/pulse, 1 KHz repetition rate). The tunable pump (235-1100nm), chopped at 500Hz, is generated in TOPAS from 75% of the split output from the Ti-Sapphire laser. The other 25% generated tunable UV-visible probe pulses by while light generation in a CaF_2 window (330-720 nm) on a translation stage. Helios ultrafast spectrometer (Ultrafast Systems LLC) was used to collect the spectra. The power of the pump pulse on the sample is 0.15 mW/pulse. The film samples were continuously translated to avoid heating and permanent degradation.

Steady State X-ray Absorption (XAS) spectroscopy.

XAS spectra were measured at the beamline 12BM-B at the Advanced Photon Source (APS) in Argonne National Laboratory. The XAS spectra were collected under room temperature with fluorescence mode. The detector was based on 13-element germanium. One ion chamber is placed before the sample and used as the incident X-ray flux reference signal. There are two ion chambers (second and third chambers) after the sample. The CeO_2 foil is placed between the second and third ion chambers and used for energy calibration and collecting Ce^{4+} spectrum. The solid samples were dispersed on Kapton tape for XAS measurement.

X-ray transient absorption (XTA) spectroscopy.

XTA spectroscopy was performed at the beamline 11ID-D, APS, Argonne National Laboratory. Samples were prepared by suspending 30 mg MOFs in 70 mL acetonitrile, which is followed by sonicating for 30 mins. The desired laser pump was generated by using TOPOS, which was pumped by the 800 nm from the ultrafast Ti: Sapphire laser amplifler system. The laser pump and X-ray probe intersect at a flowing sample stream with 550 μm in diameter. The X-ray fluorescence signals were collected at 90˚ angle on both sides of the incident X-ray beam by two avalanche photodiodes(APDs). A soller slits/Ti filter combination, which was custom designed for the specific sample chamber configuration and the distance between the sample and the detector, was inserted between the sample stream and the APD detectors. The emitted Ce X-ray fluorescence collected at certain delay time after the laser pump pulse excitation was used to build the laser-on spectrum in APS hybrid mode.

2.2. Experimental Details for Chapter 3

Materials.

Methanol (Certified ACS, > 99.8%) was purchased from Fisher Chemical and 2-methylimidazole ($C_4H_6N_2$, 97%) was purchased from Alfa Aesar. Cobalt Nitrate Hexahydrate ($Co(NO_3)_2 \cdot 6H_2O$, 99%) was obtained from Acros Organics. Ruthenizer 535($C_{26}H_{16}O_8N_6S_2Ru$, 99%) (RuN3) was purchased from Solaronix. Quartz substrate (3”x1”, 1mm thick) was purchased from Ted Pella Inc.

The Synthesis of ZIF-67 Thin Film.

ZIF-67 was synthesized according to the published procedure. Two precursor solutions were individually prepared by adding 0.73g $Co(NO_3)_2 \cdot 6H_2O$ into 50 mL methanol and 1.65 g 2-methylimidazole into 50 mL methanol. After that, equal volume of the precursor solutions was mixed. The mixture was allowed to precipitate at room temperature for about 1 hour. ZIF-67 film was prepared by immersing a piranha-etched substrate into the above mixture, where ZIF-67 crystals directly precipitated on the substrate. This procedure was repeated 3 times. The film made after each cycle was rinsed with ethanol. The as-synthesized film was dried in air before characterization.

ZIF-67 suspension was made a large volume (100mL each solution) in the absence of a substrate. The precipitated ZIF-67 was washed thoroughly with methanol via

centrifugation to remove excess ligand and supernatant species. The precipitate was then re-suspended in methanol without being allowed to dry to preserve particle size.

The Synthesis of Al_2O_3 thin films.

Al_2O_3 nanoparticles were made using precursor Sol-gel method. Briefly, 1.8 g of $Al(NO_3)_3 \bullet 9H_2O$ was added to 15 ml isopropanol, which was followed by stirring for 1 h at room temperature. The obtained colloid was transferred to an autoclave and heated at 200^oC for 16h. The resulting white precipitate was washed with ethanol 3 times and then mixed with ethanol and 3 drops of Triton X-100 under magnetic stirring. To make Al_2O_3 film, the above mixture was spin-coated to piranha-etched substrate, which is then annealed at 450^oC for 1.5 h.

The Synthesis of RuN3/ZIF-67 and RuN3/Al_2O_3 thin films.

RuN_3/ZIF-67 and RuN_3/Al_2O_3 films were prepared using dye-sensitized approach, where ZIF-67 and Al_2O_3 films were immersed into to 1mg/mL RuN_3 in methanol solution for ~20 min and 3h, respectively. The obtained RuN3 sensitized films were rinsed with ethanol to remove the physically adsorbed RuN3. The film was allowed to dry in air before characterization.

Photocatalytic Hydrogen Production Reaction.

Samples for photocatalytic hydrogen production were prepared in 6 mL septum-sealed glass vials. Each sample was made up to a volume of 4 mL, including1mg of ZIF-67, 3 mL of CH_3CN, and 0.2 mL of H_2O. 0.3 mL of TEOA (triethanolamine) was added and used as the sacrificial reducing agent. 0.1 mL $2x10^{-4}$ M RuN3 in acetonitrile was added to the mixture and used as photosensitizer. The mixture was purged with N_2 for 15 mins before irradiation by a blue LED (405 nm) lamp. The mixture was kept stirring during photocatalytic reaction. The amount of H_2 generated was quantified using Agilent 490 micro gas chromatograph (5 Å molecular sieve column) by analyzing 200 µL of the headspace of the vial.

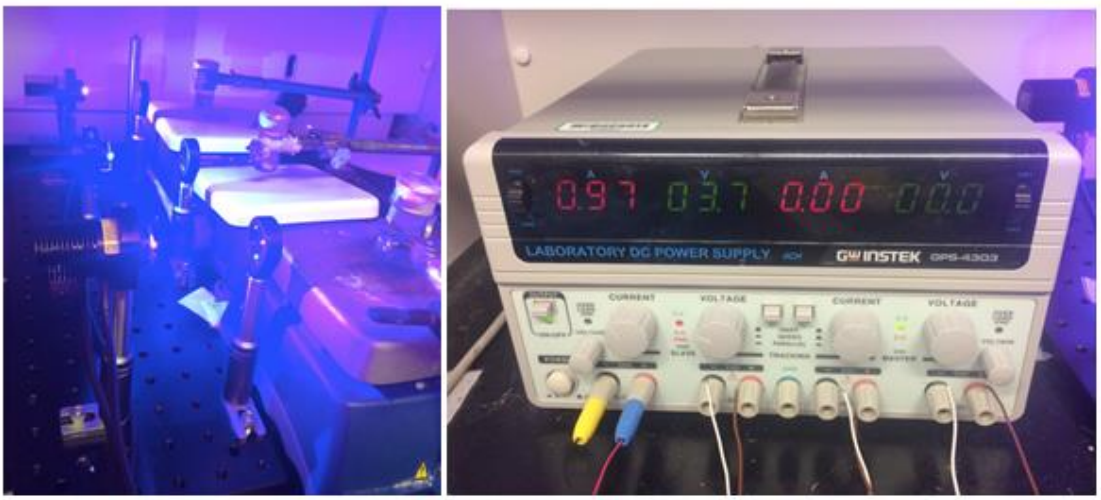

Figure 2.1 LED setup during catalytic run

Shown in Figure 2.1 is the setup for ZIF-67 HER (hydrogen evolution reaction), which includes a LED lamp for illumination, focusing lens, and reaction vials on stirring plate. LED lamp, lens and magnetic stir are aligned in a way such that the catalytic conditions are same for multiple setups. The LEDs were powered by a

separate circuit with a variable voltage power supply (GW Instek GPS-4303), the current was kept 1A during each catalytic run.

2.3. Experimental Details for Chapter 4

Materials.

$ZrCl_4$ (> 99.5%, Strem Chemicals), 2,2-bipyridine-5,5-dicarboxylic acid (H_2bpdcy) (97%, Ark Pharm), 2, 2-dipyridyl (>99%, Acros Organics), 4,4-biphenyldicarboxylic acid (bpdc) (98%, Acros Organics), glacial acetic acid (regent ACS, Acros Organics). cis-[$Ru(bpy)_2Cl_2$], [Ru(dcbpy)$(bpy)_2$]Cl_2 (Rudcbpy) and Pt(dcbpy)Cl_2 (PtDCBPY) was synthesized based on literature reported procedure. [104-105]

The synthesis of Ru-UIO-67, Pt-UIO-67 and Pt-Ru-UIO-67. Ru-UIO-67:

$ZrCl_4$ (30.0 mg, 0.13 mmol), biphenyldicarboxylic acid (H_2bpdc) (24.6 mg, 0.1 mmol), Rudcbpy (10.0 mg, 0.012 mmol), and glacial acetic acid (250 μL, 4.37 mmol) were dispersed in DMF (4.5 mL) and transferred to 20 mL autoclave. The mixture was sonicated for 20 mins and placed in an oven. The temperature of the oven was set at 120 °C for 24 hours. After the oven cools down to room temperature, the resulting solid was isolated by centrifugation, and then washed with methanol several times before being dried under vacuum.

Pt-UIO-67:

$ZrCl_4$ (30.0 mg, 0.13 mmol), biphenyldicarboxylic acid (H_2bpdc) (24.6 mg, 0.1 mmol), Ptdcbpy (8.0 mg, 0.013 mmol), and glacial acetic acid (250 μL, 4.37 mmol) were dispersed in DMF (4.5 mL) and then transferred to 20 mL autoclave. The sample was sonicated for 20 mins and placed in an oven. The temperature was set at 120 °C for 24 hours. After cooling down to room temperature, the resulting solid was isolated by centrifugation, and was washed with methanol repeatedly before being dried under vacuum.

Pt-Ru-UIO-67:

$ZrCl_4$ (30.0 mg, 0.13 mmol), biphenyldicarboxylic acid (H_2bpdc) (24.6 mg, 0.1 mmol), Rudcbpy (10.0 mg, 0.012 mmol), Ptdcbpy (8mg, 0.013mmol), and glacial acetic acid (250 μL, 4.37 mmol) were dispersed in DMF (4.5 mL), and then transferred to 20mL autoclave. The sample was sonicated for 20 mins and placed in an oven. The temperature was set at 120 °C for 24 hours. After cooling down to room temperature, the resulting solid was isolated by centrifugation, and was washed with methanol repeatedly before being dried under vacuum.

2.4. Experimental Details for Chapter 5

Materials.

$ZrCl_4$ (> 99.5%, Strem Chemicals), 2,2-bipyridine-5,5-dicarboxylic acid(H_2bpdcy) (97%, Ark Pharm), 2, 2'-dipyridyl (>99%, Acros Organics), $CoCl_2$(97% anhydrous,

Acros Organics), glacial acetic acid (ACS reagent, Acros Organics).

The synthesis of Ru-UIO-67(bpy), Co-UIO-67(bpy) and Co-Ru-UIO-67(bpy)

Ru-UIO-67(bpy):

$ZrCl_4$ (50.0 mg, 0.21 mmol), 2,2-bipyridine-5,5-dicarboxylic acid (H_2bpdcy) (45.0 mg, 0.19 mmol), Rudcbpy (10.0 mg, 0.012 mmol), and glacial acetic acid (930 μL, 16 mmol) were dispersed in DMF (20 mL), transferred to autoclave, sonicate for 20min and placed in an oven. The temperature was kept at 120 °C for 24 hours. After cooling down to room temperature, the resulting solid was isolated by centrifugation, and was washed with methanol repeatedly before being dried under vacuum.

Co-UIO-67(bpy):

$ZrCl_4$ (50.0 mg, 0.21 mmol), 2,2-bipyridine-5,5-dicarboxylic acid (H_2bpdcy) (45.0 mg, 0.19 mmol), $CoCl_2$ (25.0 mg, 0.19 mmol), and glacial acetic acid (930 μL, 16 mmol) were dispersed in DMF (20 mL), and then transferred to autoclave, the sample was sonicated for 20 mins and placed in an oven. The temperature was set at 120 °C for 24 hours. After cooling down to room temperature, the resulting solid was isolated by centrifugation, and was washed with methanol repeatedly before being dried under vacuum.

Co-Ru-UIO-67:

$ZrCl_4$ (50.0 mg, 0.21 mmol), 2,2-bipyridine-5,5-dicarboxylic acid (H_2bpdcy) (45.0 mg, 0.19 mmol), Rudcbpy (10.0 mg, 0.012 mmol), $CoCl_2$(25.0mg, 0.19mmol) and glacial acetic acid (930 μL, 16 mmol) were dispersed in DMF (20 mL), and then transferred to autoclave, the sample was sonicated for 20 mins and placed in an oven. The temperature was kept at 120 °C for 24 hours. After cooling down to room temperature, the resulting solid was isolated by centrifugation, and was washed with methanol several times before being dried under vacuum.

The synthesis of hybrid MOF films.

To make hybrid MOF films, 1 mg MOF was mixed with 0.5 mL Nafion (5% w/w in water and 1-propanol). The mixture was sonicated for 2 hours and then dispersed evenly on piranha-etched glass. The films were dried in the air.

Photocatalytic hydrogen evolution reaction (HER) for Co-Ru-UIO-67

Samples for HER were prepared in 11 mL septum-sealed glass vials. Each sample was made up to a volume of 4mL, including1 mg of MOF, 3 mL of CH_3CN, and 0.4 mL of H_2O. 0.3 mL of TEOA (triethanolamine) was added and used as the sacrificial reducing agent. The mixture was purged with N_2 for 15 mins before irradiation by a blue LED (447 nm) lamp. The mixture was kept stirring during photocatalytic reaction. The amount of H_2 generated was quantified using Agilent 490 micro gas chromatograph (5 Å molecular sieve column) by analyzing 200 μL of the headspace

of the vial.

In situ XAS

In situ XAS spectra at Co K-edge were collected at beamline 12-BM at Advanced Photon Source, Argonne National laboratory. The experiments were performed in a custom designed Teflon cell equipped with Kapton front window for X-ray irradiation and quartz rear window for LED lamp illumination. All reactants were same as optimized HER experiment except five times more Co-Ru-UIO(bpy) (5 mg) was used in the in-situ experiment to obtain decent XAS signal.

2.5. Experimental Details for Chapter 6

Materials.

$(NH_4)_2Ce(NO_3)_6$ (> 99.5%, Alfa Aesar), Tetrakis(4-carboxyphenyl)porphyrin (TCPP) (97%, TCI), benzoic acid (99%, Alfa Aesar), N,N-Dimethylformamide (DMF) (Certified ACS, Fisher Chemical).

The Synthesis of Ce-TCPP.

Ce-TCPP is synthesized by mixing $(NH_4)_2Ce(NO_3)_6$ (83.2 mg, 0.15 mmol), Tetrakis(4-carboxyphenyl)porphyrin (60 mg, 0.076 mmol), and benzoic acid (490 mg, 4 mmol) in DMF (6 mL) with 0.3 mL H_2O in a pressure tube. The mixture was

degassed and then sonicated for 10 mins. The pressure tube was kept in oil bath at 120 °C for 48 hours. After cooling down to room temperature, the resulting solid was isolated by centrifugation and washed with acetone 3 times. The samples were dried under vacuum before measurement. The formation of Ce-TCPP is confirmed by XRD, FT-IR and SEM.

2.6. Experimental Details for Chapter 7

Materials.

2,2-bipyridyl-5,5-dialdehyde (97%, Amadis Chemical), Rhenium pentacarbonyl chloride (98%, Acros Organics), Mesitylene (99%, Acros Organics), p-Dioxane(anhydrous, EMD Milipore Corporation), glacial acetic acid (ACS reagent, Acros Organics).

Synthesis of $Re(bpy)(CO)_3Cl$.

$Re(CO)_5Cl$ (0.3020 g, 0.83 mmol) and 2,2-bipyridine(0.130 g, 0.83 mmol) was dissolved in 50 mL of hot toluene. The mixture was stirred and refluxed for 1h to get yellow product. ^1H NMR (acetonitrile-d3): δ 7.44 (t, 2H), δ 8.00 (t, 2H), δ 8.23 (d, 2H), δ 8.82 (d, 2H).

Synthesis of COF.

In a 10 mL pressure tube, 4,4',4''-(1,3,5-triazine-2,4,6-triyl)trianiline (TTA) (92 mg) and 2,2-bipyridyl-5,5-dialdehyde (82.68 mg) were dispersed in a mixture of mesitylene(5.1 mL), dioxane(0.9 mL) and glacial acetic acid(0.2 mL). After degassing, the tube was sealed and heated to 120 ℃ for 3 days. The resulting solid was collected by centrifugation and washed with THF repeatedly to remove the trapped guest molecules. The powder was then dried under vacuum to produce COF in an isolated yield of 85%.

Synthesis of Re-COF.

COF (50 mg) and $Re(CO)_5Cl$ (20 mg, 0.055 mmol) were dispersed in 20 mL toluene. After refluxing for 40 mins with stirring, the orange products were filtered and washed with methanol for 3 times. The Re content in Re-COF is determined by ICP-MS to be 5.58 wt%.

CO_2 reduction for Re-COF.

Samples for CO_2 reduction were prepared in 11 mL septum-sealed glass vials. Each sample was made up to a volume of 4 mL, including 0.9 mg of Re-COF, 3 mL of CH_3CN, and 0.2 mL of TEOA (triethanolamine). The mixture was purged with CO_2 for 15 mins before irradiation by a 225W Xe lamp (420 nm cut off). The mixture was kept stirring during photocatalytic reaction. The amount of CO generated was quantified using Agilent 490 micro gas chromatograph (5 Å molecular sieve column)

by analyzing 200 μL of the headspace. Recycling experiment was performed by centrifuging Re-COF, which is then washed with acetonitrile for 3 times. andThe photocatalytic reaction was then run under the same conditions mentioned above.

In situ diffuse reflectance UV-visible spectra

Figure 2.2 In-situ diffuse reflectance spectroscopy set up 1: flow-through cuvette 2: mini-pump 3: reaction vial

Figure 2.2 shows the set up for in situ diffuse reflectance spectroscopic experiment. A mini-pump was used to pump sample for measurement during catalysis. A flow-through cuvette was connected to the reaction vial by PTFE pipes. The reaction system was purged with CO_2 for 30 mins before measurement.

Structure Simulation and Powder X-Ray Diffraction Analysis of COF

Molecular modeling of COF was simulated using Materials Studio (8.0) program. The initial lattice was created with space Group P1. The proposed structure of COF is analogous to that of COF 10, while each edge of the hexagonal ring was substituted by the framework of (1E,1'E)-1,1'-([2,2'-bipyridine]-5,5'-diyl)bis(N-(4-(1,3,5-triazin-2-yl)phenyl)methanimine). The geometry of COF was optimized with MS DMol3

module and symmetry was promoted to P6/m. Then the lattice model was geometry optimized using the MS Forcite molecular dynamics module (Universal force fields, Ewald summations), where the output results into the simulated structure. Finally, Pawley refinement was applied to define the lattice parameters, producing the refined PXRD profile with lattice parameters of a = b = 43.658 Å and c = 3.534 Å. R_{wp} and R_p values converged to 2.51% and 1.92%, respectively (Line broadening from the crystallite size and lattice strain were both concerned).

Table 2.1 Fractional atomic coordinates for the unit cell of triazine COF

COF Space group: P6/m (No. 175)							
a = b = 43.658 Å; c = 3.534 Å α = β = 90°, γ = 120°							
Atom	**x (Å)**	**y (Å)**	**z (Å)**	**Atom**	**x (Å)**	**y (Å)**	**z (Å)**
C1	-0.09036	-0.53291	0	C13	0.2398	-0.4048	0
C2	-0.07474	-0.5542	0	C14	0.20346	-0.42218	0
N3	-0.04033	-0.54151	0	C15	0.2977	-0.34971	0
C4	-0.01902	-0.50627	0	N16	0.31345	-0.36931	0
C5	-0.03188	-0.48281	0	H17	-0.09218	-0.58302	0
C6	-0.06794	-0.49639	0	H18	-0.01272	-0.45444	0
C7	0.12812	-0.4512	0	H19	-0.07923	-0.47888	0
N8	0.14914	-0.4177	0	H20	0.1375	-0.47065	0
C9	0.1855	-0.4031	0	H21	0.19059	-0.35194	0
C10	0.20527	-0.36619	0	H22	0.25754	-0.31983	0
C11	0.24167	-0.34873	0	H23	0.25434	-0.41922	0
C12	0.2593	-0.36791	0	H24	0.18871	-0.45115	0

Chapter 3.

PHOTOACTIVE ZEOLITIC IMIDAZOLATE FRAMEWORK AS INTRINSIC HETEROGENEOUS CATALYSIS FOR LIGHT-DRIVEN HYDROGEN GENERATION

3.1 Introduction

Metal organic frameworks (MOFs) are an emerging class of nanoporous crystalline materials consisting of metal nodes coordinated by bridging organic linkers.[106-113] Their inherent porous nature, large surface area, and tunable cavities have led to various applications including gas separation and storage,[114-116] chemical sensing,[30, 59, 117] and heterogeneous catalysis.[118-124] Zeolitic Imidazolate Frameworks (ZIFs) are a subclass of MOFs which are particularly attractive for catalysis application due to their exceptional thermal and chemical stability.[125-126] Recent works have demonstrated their catalytic applications for a variety of reactions including organic transformations,[127-131] as well as gas phase CO oxidation and hydrogenation.[132-133] Furthermore, by embedding photoactive guests into the structure, photocatalytic applications of ZIFs have been demonstrated for dye and phenol degradation and CO_2 reduction.[134-137]

While these examples evidently demonstrate the great promise of ZIFs in heterogeneous catalysis, ZIFs in these systems are largely treated as inert hosts for reaction substrates or/and catalytic active species, resembling the roles of zeolites in

catalysis.[138] In contrast to these studies, our recent findings show that the framework of ZIF-67 exhibits an intrinsic photochemical response, featured by multiple absorption bands in UV-Visible-Near IR region and an exceptionally long-lived excited state due to the formation of a charge separated state.[139] While our studies largely promise the application of ZIFs as intrinsic photocatalytic materials, the efficiency for visible light driven photocatalysis of ZIF-67 is expected to be low using single component ZIF-67 because of the limited absorption in the solar spectrum due to relatively small extinction coefficients of Co^{2+} d-d transitions (~100-1000 $mol \cdot L^{-1} \cdot cm^{-1}$). One desirable strategy to improve its light harvesting ability is to expand the absorption spectrum of ZIF-67 by encapsulating a chromophore into the framework, such that broader region of the solar spectrum can be absorbed and relayed to ZIF-67 through energy transfer (ENT). Although this approach has been used to improve the light harvesting properties of MOFs,[140-143] no such studies have been reported in ZIFs, yet enhancing their light absorption ability is critical for their photocatalytic and solar energy conversion application.

In this project, we investigated light harvesting and photocatalytic properties of ZIF-67 through ENT process from an sensitized chromophore, i.e. RuN3 (cis-diisothiocyanato-bis(2,2'-bipyridyl-4,4'-dicarboxylic acid) ruthenium(II)). We show that efficient ENT occurs from excited RuN3 to ZIF-67 using transient absorption (TA) spectroscopy. We also successfully demonstrate the enhanced photocatalytic activity of ZIF-67 for light-driven H_2 generation from water in the presence of RuN3, which can be attributed to the enhanced light harvesting ability of ZIF-67 through

ENT. RuN3 is chosen as a chromophore in this study because of its multifold benefits as a photosensitizer. First, it can absorb visible light < 550 nm with large extinction coefficient ($\mathcal{E}_{534nm} = 1.42x10^4\ M^{-1}cm^{-1}$)[144] where ZIF-67 has negligible absorption, and thus compensates the absorption spectrum of ZIF-67 (Figure 1a). Second, the emission spectrum of RuN3 has overlap with the ZIF-67 absorption in near IR region attributed to the lower-lying d-d transition of Co^{2+} ($^4A_2(F)$-$^4T_1(F)$, the inset of Figure 1a),[139] which makes ENT process from RuN3 to ZIF-67 practically feasible. Finally, RuN3 is a widely used photosensitizer for solar energy conversion and has well-known optical properties, which can facilitate our optical studies in this work.

3.2 Results and discussion

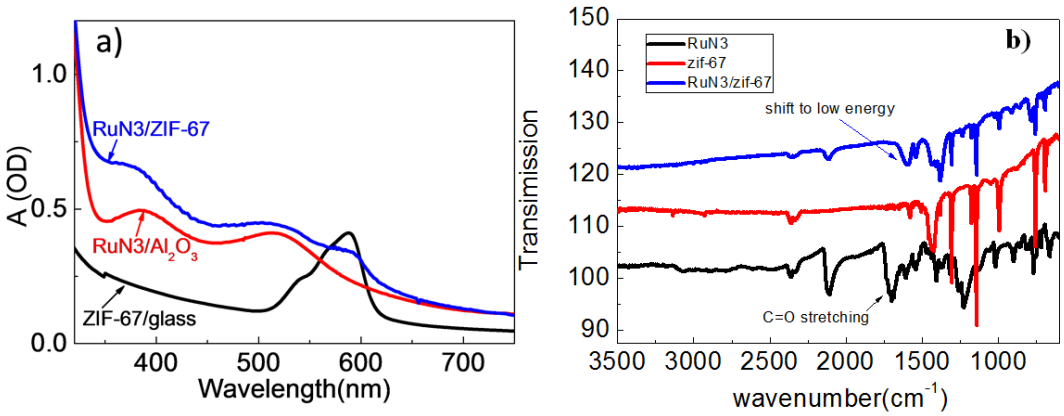

Figure 3.1 (a) UV-visible absorption spectra of ZIF-67, RuN_3/ZIF-67, and RuN_3/Al_2O_3 thin films. (b) IR spectra of RuN3, zif-67 and RuN3/zif-67 powder.

The synthesis of ZIF-67 thin films follows a direct-growth approach which is described in chapter 2.[145] The Initial characterization of RuN3/ZIF-67 was performed with UV-visible absorption spectroscopy and Powder XRD. Figure 3.1a shows the

steady state UV-Visible absorption spectra of ZIF-67, RuN3/Al_2O_3 and RuN_3/ZIF-67 thin films. The UV-Visible absorption spectrum of ZIF-67 is featured by a prominent visible band centered at 585 nm, which is consistent with previous results and can be assigned to the spin-allowed d-d transition of Co^{2+} ion in tetrahedral geometry. Compared to the spectrum of ZIF-67, the spectrum of RuN3/ZIF-67 exhibit two additional absorption bands centered at 385nm and 535nm (blue curve, Figure 3.1a) in addition to the feature due to ZIF-67. These two additional features are consistent with the metal to ligand charge transfer (MLCT) bands of RuN_3 [146] in the spectrum of RuN_3/Al_2O_3 (red curve, Figure 3.1a), and thus can be assigned to the absorption of RuN3 in RuN_3/ZIF-67 film. Because the size of RuN_3 is much larger than the aperture size of ZIF-67 (~ 3.4 Å),[125] we believe that RuN_3 molecules are directly attached to the surface of ZIF-67 thin film rather than being encapsulated inside the cavities. We use RuN_3 sensitized Al_2O_3 thin film as a control sample to account for the intrinsic effect of porous structure on the optical properties of RuN_3 because of its well-known inert nature, i.e. large bandgap with sufficiently negative conduction band and positive valence band prevents charge/energy transfer from most light harvesting chromophores that we are interested in. The adsorption of RuN_3 on the surface of ZIF-67 thin film is believed to be through –COOH anchoring group in RuN_3, which is supported by the shift of C=O stretching mode in IR absorption spectra upon binding. [147] As shown in Figure 3.1 b, the C=O stretching of RuN3 occurs in ~1690cm, while that in RuN3/ZIF shifts to ~1600cm. The similar frequency shift of C=O has been observed previously in RuN3 sensitized TiO_2 semiconductor nanocrystals and was

attributed to the anchoring of RuN3 to the surface of TiO_2 through –COOH group. As a result, we also attributed the frequency shift of C=O in RuN3/ZIF-67 to the attachment of RuN3 to ZIF-67 surface thorough –COOH group.

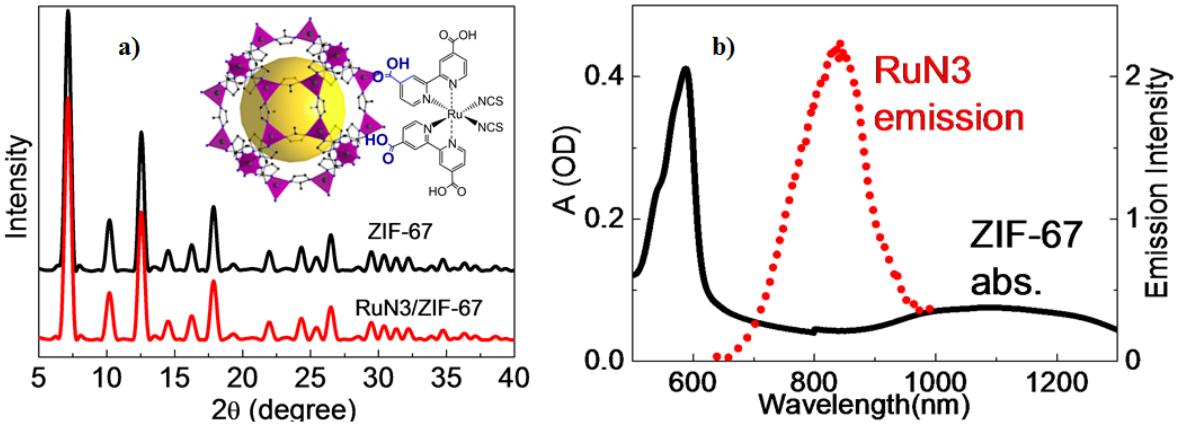

Figure 3.2 (a) Powder XRD patterns of ZIF-67 and RuN_3/ZIF-67. The inset shows the cartoon of energy transfer dynamics from RuN_3 to ZIF-67. The yellow ball indicates the cavity in the framework. (b) The spectral overlap between the absorption spectrum of ZIF-67 and emission spectrum of RuN_3

Figure 3.2a shows the XRD patterns of ZIF-67 and RuN_3/ZIF-67. The XRD patterns of RuN3/ZIF-67 strongly resemble that of ZIF-67, both of which agree well with the literature results of ZIF-67 with SOD topology, [148] suggesting that the crystal structure of ZIF-67 retains after RuN_3 binding. One critical criterion for efficient ENT from RuN3 to ZIF-67 is that the emission spectrum of RuN3 needs to have sufficient overlap with the absorption spectrum of ZIF-67. Figure 3.2b shows the emission spectrum of RuN_3 as well as the absorption spectrum of ZIF-67. It can be seen that these spectra have overlap in near IR region, suggesting that ENT from RuN_3 to ZIF-67 is feasible.

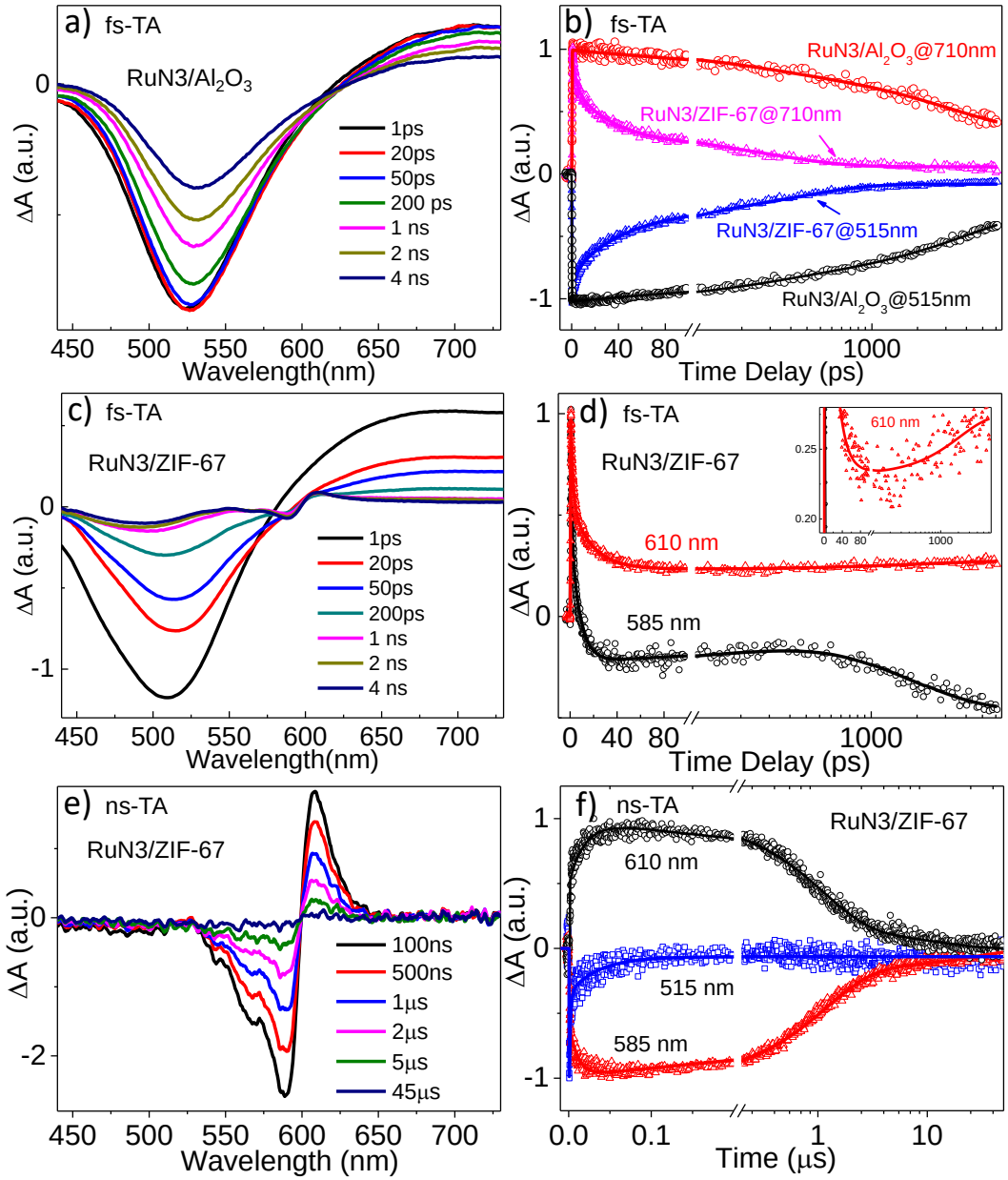

Figure 3.3 Femtosecond transient absorption (fs-TA) spectra of RuN3/ZIF-67 (a) and RuN3/Al2O3 (c) thin films. (b) The comparison of excited state decay (710 nm) and ground state bleach recovery (515 nm) of RuN3 in RuN3/ZIF-67 and RuN3/Al2O3 thin films. (d) The fs-kinetic traces of RuN3/ZIF-67 thin film at 610 nm and 585 nm, demonstrating the formation of excited state ZIF-67. (e) Nanosecond transient absorption (ns-TA) spectra of RuN3/ZIF-67 film. (f) The ns-kinetics traces of RuN3/ZIF-67 at 610 nm, 515 nm, and 585 nm.

Transient absorption (TA) spectroscopy was used to examine ENT dynamics from RuN_3 to ZIF-67. To account for intrinsic effect of porous surface on excite state

dynamics, we examined the excited state (ES) dynamics of RuN3 on Al_2O_3 thin film, which represents a non-ENT and non-charge transfer model. As shown in Figure 3.3a, the femtosecond TA (fs-TA) spectra of RuN3/Al_2O_3 thin film consist of a negative band centered at 525 nm and a broad absorption feature > 615 nm. These features have been observed previously[149] and can be assigned to the photoinduced ground state bleach (GSB) and ES absorption of RuN3, respectively. The recovery of GSB (red open circles, Figure 3.3 b) and the decay of ES (black open circles, Figure 3.3 b) occur with same kinetics with the presence of an isosbestic point at 622 nm (Figure 3.3 a), suggesting that the recovery of GS molecules from ES is the only relaxation process responsible for the observed ES dynamics.

Compared to the fs-TA spectra of RuN3/Al_2O_3, dramatic difference was observed in the spectra of RuN3/ZIF-67 (Figure 3.3 c). First, the recovery of GSB and the decay of ES absorption of RuN_3 were simultaneously enhanced, which can be further clearly seen from their kinetic traces (pink and blue open triangles, Figure 3.3b). These features are accompanied by the formation of a new negative band centered at 589 nm and an absorption band centered at 606 nm. The formation of these new features is further confirmed from their kinetic traces at 585 nm and 610 nm, where a rising component was clearly observed in each kinetic trace at later time (> 1 ns) (Figure 3.3d and inset). Because these new features closely resemble the derivative-like feature observed previously in ZIF-67 after direct excitation of d-d transition,[139] they can be attributed to the formation of ES of ZIF-67. We can exclude the possibility that ES of ZIF-67 is due to the direct excitation of ZIF-67 as negligible fs-

TA signals were observed in ZIF-67 following 410 nm excitation under the same experimental conditions. The formation of ES ZIF-67 due to photoexcitation of RuN3, along with the simultaneously enhanced GSB recovery and ES decay of RuN3, all support that ENT process occurs from excited RuN3 to ZIF-67.

Because the only spectral features after ~100 ns observed in nanosecond TA (ns-TA) spectra of RuN3/ZIF-67 (Figure 3.3 e) arise from ZIF-67, we can rule out the possibility of charge (electron or hole) transfer process from RuN3 to ZIF-67. As electron/hole transfer process leads to the formation of oxidized/reduced state of RuN3, the GSB of RuN3 should be expected in ns-TA spectra if it occurs. The negligible contribution from the GSB of RuN3 in ns-TA spectra of RuN3/ZIF-67 thus suggests that ENT is the only process accounting for the spectral change of RuN3/ZIF-67 from RuN3/Al_2O_3. Consequently, the ENT rate from RuN3 to ZIF-67 can be directly measured by probing the kinetic traces of GSB recovery of RuN3, ES decay of RuN3, or the formation of ES ZIF-67. Due to the spectral overlap of ES ZIF-67 with RuN3 GSB and ES at where ES ZIF-67 occurs, the ENT rate in this work was quantified by fitting the fs- and ns-kinetic traces of GSB of RuN3 using multiple-exponential decay functions, from which we obtained an average ENT rate of 1.2 ns with fitting parameters 11.2 ps (38.4%), 159 ps (51.8%), and 11.6 ns (9.8%) (Table 3.1). Given the average recovery time of RuN3 GSB in RuN3/Al_2O_3 (7.5 ns, Figure 3.4), the quantum yield of ENT process can be estimated according to the equation $\eta = k_{ENT}/(k_{ENT} + k_i)$, where k_{ENT} and k_i are the rate constants for ENT and intrinsic GSB recovery of RuN3, respectively. The obtained quantum yield of ENT is ~ 86%,

suggesting an efficient ENT process from RuN3 to ZIF-67.

Table 3.1 Femtosecond transient absorption multi-exponential fit results.

Excitation	Probe	τ_1,ps(A1,%)	τ_2,ps(A2,%)	τ_3,ns(A3,%)
410nm	515nm	11.2(38.4)	159(51.8)	11.6(9.8)

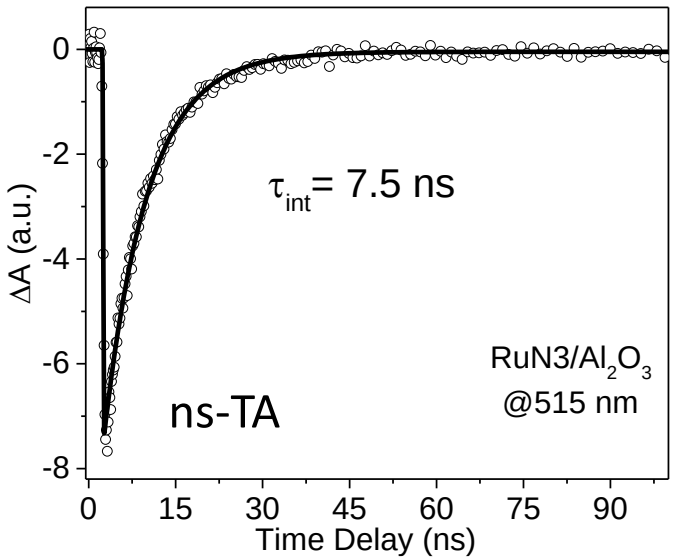

Figure 3.4 The ground state bleach recovery kinetics of RuN3/Al_2O_3 film measured by nanosecond transient absorption spectroscopy

With the understanding of ENT dynamics, we proceeded to examine the photocatalytic properties of ZIF-67 for light-driven H_2 generation from water. The photocatalytic reactions were performed in the presence of triethanolamine (TEOA) as sacrificial electron donor and H_2O as proton source in acetonitrile solution. Experiments using other sacrificial donors, proton sources, and solvents were also carried out, which either results in less amount of H_2 production or faster degradation

of ZIF-67 (Table 3.2). Upon illumination with 405 nm LED lamp (280 mW), which selectively excites RuN3 only, a notable amount of H_2 was generated in RuN3/ZIF-67 mixture in acetonitrile solution (Table 1). Under the optimized conditions, i. e. RuN3 (0.02 μmol), ZIF-67 (1 mg), TEOA (0.3 mL), and H_2O (0.2 mL) in acetonitrile solution, the amount of H_2 generated reaches a final value of 48.5 mol after 10 h (Figure 3a and Table 1). In contrast, no hydrogen can be detected after 10 h when either ZIF-67 or H_2O is omitted in the catalytic reaction (Table 1), suggesting that ZIF-67 and H_2O are the key components for photodriven H_2 generation, which act as the catalyst and proton source, respectively. Meanwhile, a negligible amount of hydrogen can be detected in the absence of RuN3, which is expected as ZIF-67 has negligible absorption at 405 nm and unambiguously confirms that the enhanced activity of RuN3/ZIF-67 system for H_2 production is attributed to the efficient ENT process from RuN3 to ZIF-67.

Table 3.2 Photocatalytic Hydrogen Production with RuN_3/ZIF-67

Variables	Trials	H_2 (μmol/g)	time
Proton source[a]	TEA·HCl (30 μmol)	2.2	< 1 h
	HCl with varying pH	0	< 1 h
	H_2O (0.2 mL)	48.5	10 h
	MeOH	15	3.5 h
RuN3 concentrations[b]	0.02 μmol of RuN3	48.5	10 h
	0.06 μmol of RuN3	43.2	10 h
	0.1 μmol of RuN3	10.8	10 h
	No ZIF-67	0	10 h

Control experiment	No H_2O	0	10 h
	No RuN3	0	10 h
	No RuN3	0	10 h

General conditions: the reaction was run in acetonitrile solution in the presence of TEOA, 1 mg of ZIF-67. All samples were irradiated with 405 nm LED lamp (280 mW). [a]RuN3 (0.02 μmol); [a]RuN3 (0.02 μmol); [b]H_2O (0.2 mL).

An induction period was observed in the first 2 hours before H_2 evolution commences (Figure 3.5 b). Induction periods have been reported in other H_2 generation systems based on Co molecular catalysts, [150-151]and are typically attributed to the multiple equilibriums that require the conversion of Co^{III}/Co^{II} to their reduced intermediates or hydrides for H_2 production. While these molecular photosensitizer/Co molecular catalyst systems involve the reductive/oxidative quenching of the photosensitizers, which appears to be different from the current RuN3/ZIF-67 system in which RuN3 only participate ENT process, the mechanistic origins of induction period in these systems may share the similarity in terms of the catalysts. We have previously shown that photoexcitation of ZIF-67 leads to the reduction of Co^{II} center via ligand-to-metal charge transfer (LMCT) process.[139] Given that ENT is the only available process occurring upon RuN3 excitation, which leads to the formation of the same LMCT state based on our TA results, we believe that the resulting LMCT is likely the intermediate state for H_2 production. As a result, the induction period in current system may result from the conversion of Co^{II} center to this LMCT intermediate state or other intermediates formed afterwards. (Figure 3.5 a). fs-TA spectra of RuN_3/Al_2O_3 in the presence of TEOA further confirms the

mechanism (Figure 3.6), as electron transfer from TEOA to RuN3 will not competing with energy transfer process, which evident by the formation of ZIF-67 ES accompanied by the simultaneously faster GSB and ES decay for RuN_3.

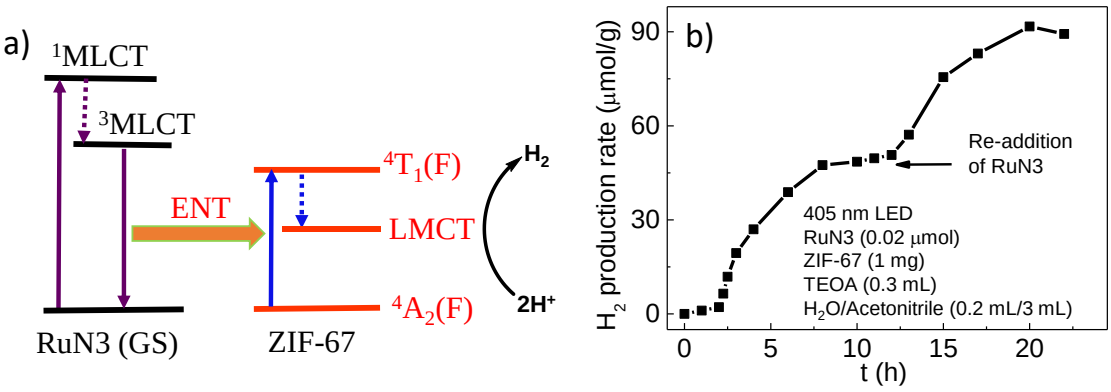

Figure 3.5 (a) Jablonski diagram of energy transfer process from RuN3 to ZIF-67, followed by the formation of charge-separated state with LMCT nature in ZIF-67, which eventually results in hydrogen evolution. (b) H_2 evolution profile of RuN3/ZIF-67 in H_2O/acetonitrile, TEOA (0.3 mL), irradiated at 405 nm. The profile after 10 hours is obtained after adding a fresh batch of RuN3 to the inactive system.

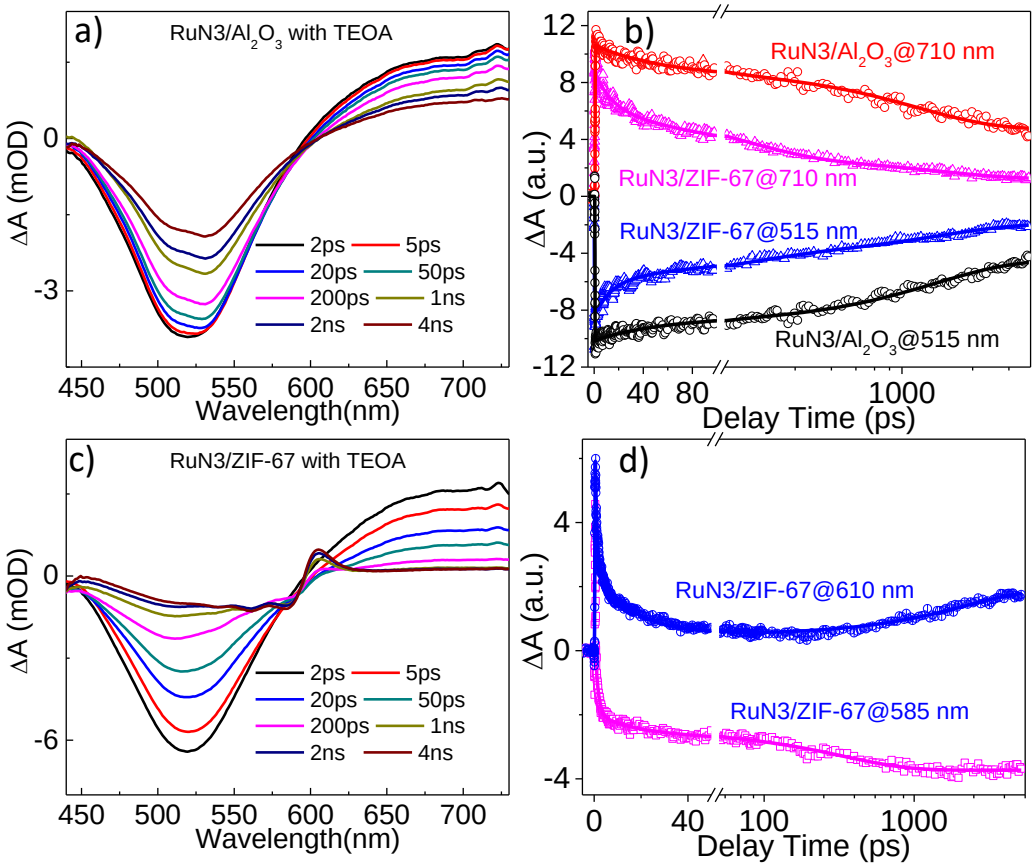

Figure 3.6 Femtosecond transient absorption (fs-TA) spectra of RuN3/Al_2O_3 (a) and RuN3/ZIF-67 (c) thin films in the presence of TEOA in acetonitrile solution following 410 nm excitation. (b) The comparison of excited state decay (710 nm) and ground state bleach recovery (515 nm) of RuN3 in RuN3/ZIF-67 and RuN3/Al_2O_3 thin films. (d) The fs-kinetic traces of RuN3/ZIF-67 thin film at 610 nm and 585 nm, demonstrating the formation of excited state ZIF-67.

The reason for the cease of H_2 generation after 10h was investigated by reactivation of the RuN3/ZIF-67 system after photocatalysis. As shown in Figure 3.5b, the addition of the same amount of fresh RuN3 restores the photocatalytic reaction and recovers ~ 93% of the efficiency. In contrast, the addition of ZIF-67 cannot restore the reaction, which is consistent with the results from XRD and X-ray absorption spectroscopy (Figure 3.7), where ZIF-67 retains its structure during

photocatalysis.

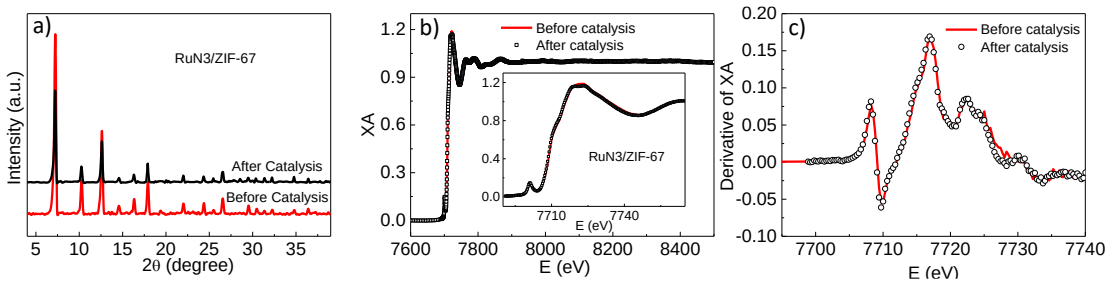

Figure 3.7 The comparison of powder XRD patterns (a), X-ray absorption spectra at Co K-edge (b), and the derivative of X-ray absorption spectra (c) of RuN3/ZIF-67 before and after catalysis.

Furthermore, it is notable that the supernatant solution after photocatalysis becomes brown-yellow (typical color for Ru complex) in contrast to colorless solution before photocatalysis, suggesting that RuN3 have detached from ZIF-67. The UV-visible spectrum of the supernatant solution after the catalysis appears to be different from RuN3 (Figure 3.8), suggesting that RuN3 has been permanently degraded. These results together suggest that degradation of RuN3 is the limiting factor for the deactivation of H_2 production. The turn over number for H_2 generation in this system is estimated to be 4.85 in terms of RuN3.

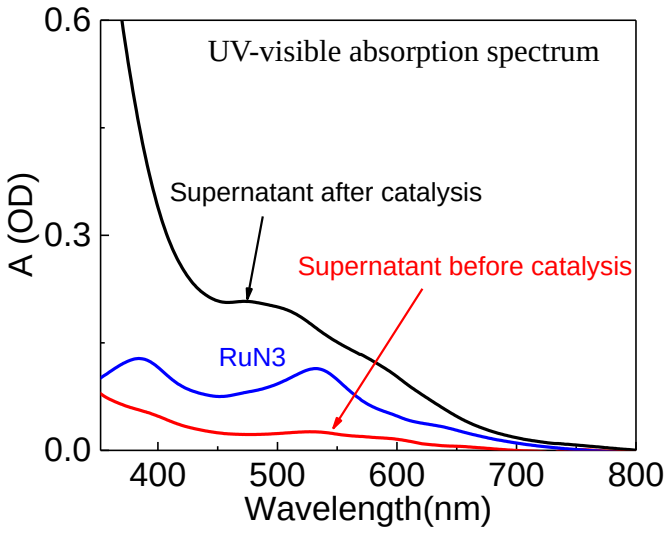

Figure 3.8 The comparison of the UV-visible absorption spectra of the supernatant solution of RuN3/ZIF-67 catalytic system before and after photocatalysis.

While higher activity for H_2 evolution has been reported using other MOFs doped with cocatalyst,[54, 56-57, 152-154] it is unfair to compare the current RuN_3/ZIF-67 system with these systems as their activities were mainly boosted by the cocatalysts. Indeed, the photoactivity of RuN3/ZIF-67 for H_2 evolution (48.5 mol/g) compares well with these systems in the absence of cocatalysts (0-10^2 mol/g).[54, 56-57, 152-154] These findings, together with the significantly enhanced photocatalytic activity due to ENT from RuN_3, suggest the potential of ZIF-67 as photocatalysts for light-driven fuel generation.

In summary, we have designed a new porous hybrid system by sensitizing RuN_3 photosensitizer to ZIF-67. Using transient absorption spectroscopy, we show that efficient ENT process occurs from RuN_3 to ZIF-67 after selectively exciting RuN_3, which ultimately leads to significantly enhanced light-driven H_2 production from H_2O. These findings not only establish the capability to enhance the light harvesting

properties of ZIFs by encapsulating photosensitizers via ENT but also demonstrate the potential of ZIF-67 as an intrinsic photocatalyst for solar fuel conversion.

3.3. Conclusion and future work

In this work, we investigated a new hybrid system, i.e. RuN3/ZIF-67 by sensitizing RuN3 to the surface of ZIF-67. The ENT process between RuN_3 and ZIF-67 was examined using transient absorption spectroscopy following selectively exciting RuN_3 at 410 nm. We show that highly efficient ENT occurs from excited RuN3 to ZIF-67, which finally leads to the enhanced light-driving H_2 generation from H_2O. These results not only suggest that the light-harvesting capability of ZIF-67 was enhanced by sensitizing RuN3 photosensitizer to ZIF-67 but also reveal the potential of ZIF-67 as an intrinsic photocatalyst for solar energy conversion.

Due to the limited pore aperture (3.4 Å) in ZIF-67, RuN_3 in current work can only be sensitized onto the surface of ZIF-67, which largely limits the direct interaction of ZIF-67 with RuN3 and thus the efficiency of ENT and solar fuel generation. With a goal to utilize the porous structure of ZIFs and develop ZIF materials as efficient single site catalyst for solar fuel conversion, it is necessary to encapsulate chromophores into the cavity of ZIF-67 or directly incorporate the chromophore to the framework of ZIF-67. Therefore, the future work will focus on developing approaches to either encapsulate chromophores into the cavity of ZIFs or incorporate them into ZIF-67 framework.

Chapter 4.

ELUCIDATING CHARGE SEPARATION DYNAMICS IN A HYBRID METAL-ORGANIC FRAMEWORK PHOTOCATALYST FOR LIGHT-DRIVEN H_2 EVOLUTION

4.1 Introduction

The utilization of solar energy to drive hydrogen generation from water is one of the best solutions to address the global energy and environmental problems.[155-156] In the past decades, diverse photocatalytic systems for H_2 generation including homogeneous and semiconductor based/metal doped heterogeneous systems have been developed, which typically consist of light harvesting materials, catalysts, and proton and electron sources.[157-160] However, the performance of these systems for H_2 generation in terms of both activity and stability is far from satisfactory. In addition to poor stability and efficiency, the homogeneous molecular systems suffer from the difficulty in recycling from the reaction system.[161-164] While heterogeneous systems have shown potential in long-term stability and high activity, these materials suffer from two major limitations that hamper their further use as photocatalytic materials: (1) the lack of design flexibility and (2) the poor understanding of the catalytic active species.[165-169]

To integrate the beneficial features and overcome the drawbacks of homogeneous and heterogeneous photocatalytic systems for H_2 generation, metal organic

frameworks (MOFs), an emerging class of porous crystalline materials, could be a judicious choice. MOFs are constructed from metal ions/clusters covalently interconnected to multidentate organic linkers.[106-111, 113, 170] The versatility of these components not only offers the capability to tune their cavity but also allows incorporation of molecular functional units into its heterogeneous crystal matrix, opening up the possibility to address the stability issues and allow high resolution studies of the incorporated catalytic active sites using a suite of physical characterization methods.[67, 171-177]

Due to these reasons, recent efforts on MOF photocatalysis have extended to incorporate molecular photosensitizers or/and catalysts into MOFs structure. While a large number of functionalized MOF systems with either molecular photosensitizers (PSs) or catalysts incorporated into the framework have been reported recently toward versatile applications,[55, 60, 67, 141-142, 171-173, 178-191] there are only two examples that integrate both PS and catalysts for photocatalytic H_2 generation. One example includes the incorporation of $[Ru(dcbpy)(bpy)_2]^{2+}$(dcbpy = 2,2′-bipyridyl-5,5′-dicarboxylic acid) and $Pt(dcbpy)Cl_2$ complex to the MOFs scaffold (UIO-67), which can serve as PSs and catalysts, respectively, for photocatalytic H_2 generation from water.[184] The second example reported the successful incorporation of Ir(III) complex as PS and Pt(II) complex as catalyst into UIO-67 MOFs, which demonstrated significant increase in both H_2 evolution activity and robustness compared to its homogeneous counterpart.[192] While these examples demonstrate the potential of MOFs as versatile platform for incorporating molecular modules necessary for

photocatalytic applications, the fundamental aspects with regard to light harvesting and charge separation (CS) dynamics of these molecular functional units in MOFs remain less explored,[63, 193-200] yet it is essential for further development of these materials. Herein, we report the CS dynamics in $[Ru(dcbpy)(bpy)_2]^{2+}$ and $Pt(dcbpy)Cl_2$ functionalized UIO-67 MOF (Ru-Pt-UIO-67, Figure 1a) which demonstrates efficient H_2 generation from water using the combination of optical transient absorption (OTA) and X-ray transient absorption (XTA) spectroscopy. The direct correlation of the fundamental insights into the CS dynamics with their function for photocatalysis provides important guidance in rational design of new and efficient photocatalytic MOF systems.

4.2 Results and discussion

Ru-Pt-UIO-67 and control samples including Pt-UIO-67, Ru-UIO-67, and UIO-67 were synthesized according to previously published literature protocols.[63, 187] The morphology of these MOF samples was examined by SEM. As shown in Figure 4.1b, Ru-Pt-UIO-67 MOF particles show octahedral or quasi-octahedral shape with sizes ranging from 500 to 1000 nm, which are similar to the morphology of Pt-UIO-67 and Ru-UIO-67 MOF particles (Figure 4.2a, 4.2b). The surface area and pore size of Ru-Pt-UIO-67 are 1504 m^2/g and 1.65 nm (Figure 4.2c), respectively, which are comparable to literature data,[54, 184] suggesting the porous structure of Ru-Pt-UIO-67 MOF. Figure 4.1c shows the XRD patterns of the above four MOFs. All of the peaks that correspond to UIO-67 occur in Pt or/and Ru incorporated MOFs, suggesting the

retention of parent framework after incorporating molecular moieties. The incorporation of Ru and Pt moieties was confirmed by diffuse reflectance UV−visible spectroscopy. As shown in Figure 4.1d, compared to the absorption spectrum of UIO-67, an additional broad band (~400−600 nm) was observed in the spectrum of Ru-Pt-UIO-67. This broad band is consistent with the combined absorption of Pt complex in Pt-UIO-67 and Ru complexes in Ru-UIO-67 and thus can be attributed to the absorption resulting from Pt and Ru moieties incorporated into UIO-67. EDX analysis in random areas suggested that Zr, Ru, Pt elements were abundantly distributed in Ru-Pt-UIO-67 with elemental ratio of Ru/Pt about 1.4.

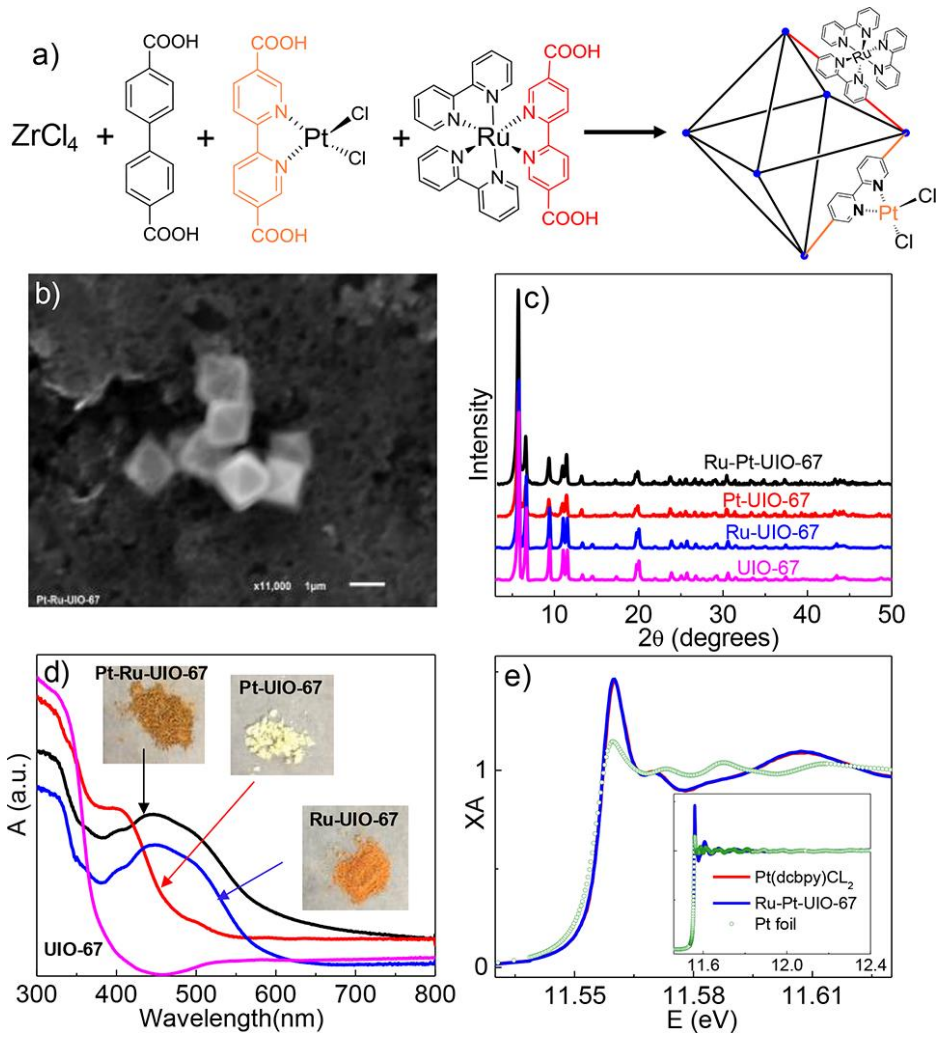

Figure 4.1 (a) Synthetic scheme (a) and SEM image of Ru-Pt-UIO-67 MOF. XRD patterns (c) and reflectance UV−visible spectra (d) of Ru-Pt-UIO-67, Pt-UIO-67, Ru-UIO-67, and UIO-67. (e) XANES spectra of Ru-Pt-UIO-67, Pt(dcbpy)Cl_2, and Pt foil at Pt L3-edge. The inset shows their EXAFS spectra.

In addition to the bulk structure, the local coordination environment of Pt center was examined by steady-state X-ray absorption spectroscopy (XAS). Figure 4.1e shows the X-ray absorption near edge structure (XANES) spectra of Ru-Pt-UIO-67 collected at Pt L3-edge. For comparison, the XANES spectra of Pt foil and molecular Pt(dcbpy)Cl_2 complex were also shown in Figure 4.1e as reference spectra. As shown in Figure 4.1e, the white line intensity of Ru-Pt-UIO-67 at 11.568keV, corresponding to $2p_{2/3}$ to 5d transition, is significantly higher than that of Pt foil while it remains similar to that of Pt(dcbpy)Cl_2 sample. As the white line intensity of Pt center is directly related to its density of unoccupied d states,[201-202] the similar amplitude of this transition among Ru-Pt-UIO-67 MOF and Pt(dcbpy)Cl_2 complex, which is much larger than that of Pt foil, suggests that Pt-moiety incorporated into MOF structure retains its Pt^{II} oxidation state as that in molecular Pt(dcbpy)Cl_2.To gain insight on the local coordination structure of Pt in MOF samples, we quantitatively analyzed the extended X-ray absorption fine structure (EXAFS) spectra of these samples using FEFF model (Figure 4.3). The resulting fitting parameters are listed in Table 4.1. It is found that the coordination numbers and bond distances of Pt to N atoms in dcbpy and Pt to Cl atoms remain the same among both samples, further supporting that the structure of Pt(dcbpy)Cl_2 is retained during MOF synthesis.

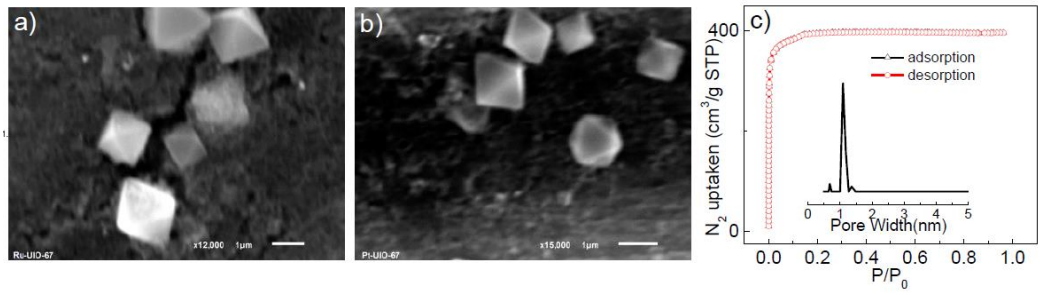

Figure 4.2 SEM of Ru-UIO-67 (a) and Pt-UIO-67 (b). c) N_2 adsorption isotherm and pore size distribution (inset) of Ru-Pt-UIO-67.

The photocatalytic performance of Ru-Pt-UIO-67 MOF for light-driven H_2 generation was examined under illumination of a broad band Xe lamp, where the IR and UV light from the Xe lamp was extensively filtered by water filter and 420 nm long-pass filter, respectively. The experimental parameters such as the sacrificial donors, solvents and the amount of proton source and MOF particles were systematically varied to find the conditions that can generate the maximum amount of H_2 per gram of catalyst (Figure 4.4). On the basis of these experiments, the optimized condition for the Ru-Pt-UIO-67 photocatalytic system is under Pt-Ru-UIO-67 (0.5 mg), 0.3 mL of H_2O, and 0.3 mL of DMA (N,N-dimethylaniline) in 3 mL of acetonitrile solution. Control experiments (Figure 4.4c) in the absence of either DMA or H_2O do not produce H_2, suggesting their key roles as sacrificial donor and proton source, respectively. The systems using Pt-UIO-67 or Ru-UIO-67 with the same metal loading as that in Ru-Pt-UIO-67 produce negligible amount of H_2, suggesting that both Ru and Pt moieties are essential for H_2 generation. Shown in Figure 4.4a is the full time-profile of H_2 generation collected under the optimum condition. The system produces H_2 steadily for at least 30 h, achieving 34 000 μmol H_2/g of MOF,

corresponding to TON of 801 in terms of Pt. As shown in our optimization experiments (Table 4.2), the performance of Ru-Pt-UIO-67 for H_2 generation can be easily affected by a number of experimental parameters, and we attributed the significantly enhanced H_2 activity and elongated duration in current system with respect to the previous results [184] to the difference of the catalytic conditions, suggesting the necessity of performing optimization experiments carefully.

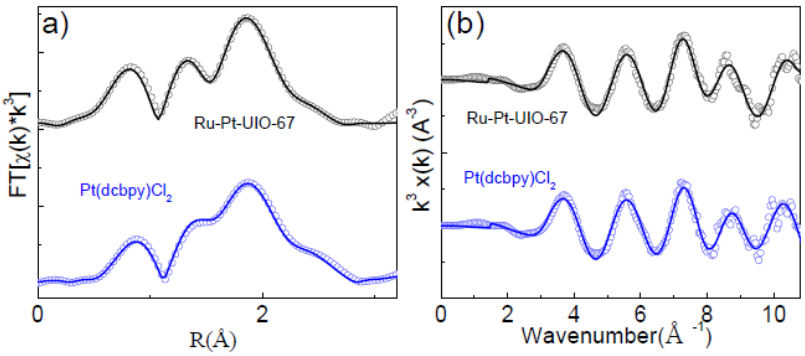

Figure 4.3 The Fourier transformed R space (a) and k space (b) spectra of Ru-Pt-UIO-67 and $Pt(dcbpy)Cl_2$ model complex. The data are shown as open points and FEFF fits as solid lines.

Table 4.1 The EXAFS fitting parameters of Ru-Pt-UIO 67, $Pt(dcbpy)Cl_2$ and reported single crystal data. Additional parameters: $\Delta E_0 = 8.008$, $S_0^2 = 0.934$ (all paths) for both samples

		Ru-Pt-UIO-67		$Pt(dcbpy)Cl_2$		$Pt(dcbpy)Cl_2$ [1]
vector	N	R(Å)	$\sigma^2 x\ 10^{-3}(Å^2)$	R(Å)	$\sigma^2 x\ 10^{-3}(Å^2)$	R(Å)
N	2	1.97(+/- 0.02)	1	1.98(+/- 0.02)	1.4	2.00, 2.01
Cl	2	2.29(+/- 0.02)	1.2	2.29(+/- 0.02)	1.7	2.28, 2.30
C_1	2	2.97(+/- 0.02)	10	2.93(+/- 0.02)	6.4	2.86
C_2	2	2.97(+/- 0.02)	3.8	2.95(+/- 0.02)	2.4	3.00

To gain insight into the recyclability of the system, we stopped the reaction every 10 h and collected Ru-Pt-UIO MOFs from the reaction mixture via centrifugation. The

resulting Ru-Pt-UIO-67 MOFs were washed with acetonitrile and redispersed in a fresh catalysis mixture for H_2 generation experiment. As shown in Figure 4.4b, the catalytic activity of the system does not decrease for at least three cycles of experiments, suggesting that Ru-Pt-UIO-67 MOF catalysts are recyclable.

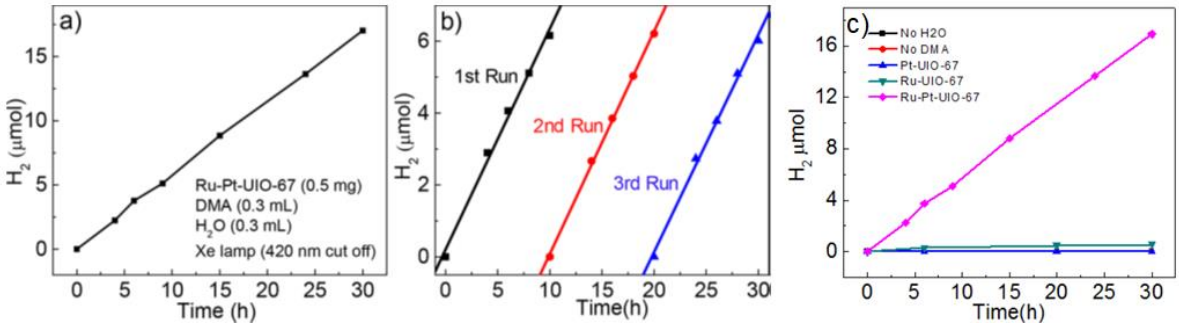

Figure 4.4 (a) Time profile of H_2 production by Ru-Pt-UIO-67 under Xe lamp illumination in the presence of DMA (0.3 mL) and H_2O (0.3 mL) in acetonitrile solution (3 mL). (b) Recycling of Ru-Pt-UIO-67 catalyst after multiple 10 h experiments.

Table 4.2 Optimization of light driven H_2 evolution reaction. The amount of H_2 produced using different sacrificial donors and solvents, as a function of MOF concentration, H_2O concentration, and DMA concentration.

Conditions	Varying parameters	H_2(μmol/g)
1mg Ru-Pt-UIO-67	3mL CH_3CN, 0.3mL TEA	7065
0.3mL H_2O	3mL CH_3CN, 0.3mL TEOA	8675
420nm cut off Xe lamp	3mL CH_3CN,0.3mL DMA	17021
30h	3mL DMF, 0.3mL DMA	593
3mL CH_3CN	0.25mg Ru-Pt-UIO-67	17350
0.3mL DMA	0.5mg Ru-Pt-UIO-67	33634
0.3mL H_2O	0.75mg Ru-Pt-UIO-67	25127
420nm cut off Xe lamp 30h	1mg Ru-Pt-UIO-67	16915
0.5mg Ru-Pt-UIO-67	0mL H_2O	0
3mL CH_3CN	0.3mL H_2O	34000
0.3mL DMA	0.7mL H_2O	33965
420nm cut off Xe lamp 30h		
0.5mg Ru-Pt-UIO-67	0mL DMA	0
3mL CH_3CN	0.3mL DMA	34000
0.3mL H_2O	0.5mL DMA	33556
420nm cut off Xe lamp 30h	0.7mL DMA	34112

While the photocatalytic experiments above successfully demonstrate the capability of Ru-Pt UIO-67 MOF as efficient and robust photocatalysts for H_2 generation and both Ru and Pt moieties play important roles in catalysis, it is essential to examine the CS dynamics to unravel the specific roles these moieties play in catalysis. The CS dynamics in Ru-Pt-UIO-67 MOF was examined using optical transient absorption (OTA) spectroscopy. Due to the spectral overlap between Ru and Pt moieties in the UV−visible region (Figure 4.1d), 480 nm pump light was used as excitation source such that majority of the excitation light was absorbed by the Ru-moiety. Indeed, the direct excitation of Pt-UIO-67 MOFs yields negligible OTA signals, and we can thus exclude the contribution of Pt-moiety to the OTA signals in the spectra of Ru-Pt-UIO-67 due to direct excitation of Pt-moiety. Figure 4.5a and Figure 4.5b show the femtosecond OTA spectra of Ru-UIO-67 and Ru-Pt-UIO-67, respectively. The OTA spectra of Ru-UIO-67 were used as control to illustrate the intrinsic excited state (ES) dynamics of Ru-moiety in MOF framework in the absence of Pt-moiety. As shown in Figure 4.5a, the OTA spectra of Ru-UIO-67 consist of a negative band centered at ~514 nm and a broad absorption

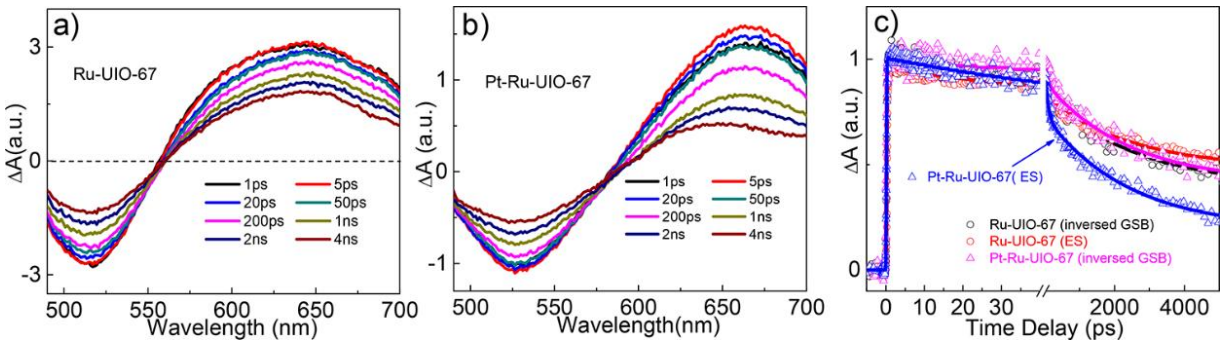

Figure 4.5 Femtosecond OTA spectra of Ru-UIO-67 (a) and Ru-Pt-UIO-67 (b). (c) Comparisons of the ground state bleach (GSB) recovery and excited state decay kinetics between Ru-UIO-67 and Ru-Pt-UIO-67. The GSB recovery kinetics for both Ru-UIO-

67 and Ru-Pt-UIO-67 were inverted for better comparison.

band at ~634 nm, which can be attributed to the ground state bleach (GSB) and ES absorption of Ru-moiety, respectively. The recovery of GSB and decay of ES follow the same kinetics (Figure 4.5c), as well as the presence of a clear isosbestic point at 554 nm between these two spectral features, suggesting that the recovery/decay kinetics of these two species represent the same recombination process, i.e., the intrinsic recovery of GS molecules from ES. While the similar GSB and ES absorption were observed in the OTA spectra of Ru-Pt-UIO-67, distinct differences were observed between two spectra. As shown in Figure 4.5c, while the GSB recovery kinetics of Ru-Pt-UIO-67 remains similar to that of Ru-UIO-67, the ES absorption in Ru-Pt-UIO-67 decays much faster than that in Ru-UIO-67. These results are consistent with the spectral features when electron transfer (ET) process occurs, suggesting that ET from Ru- to Pt-moiety in Ru-Pt-UIO-67 is responsible for the enhanced ES decay in Ru-Pt-UIO-67 MOF. As shown in Table 4.3, the GSB recovery and ES decay kinetic traces of Ru-UIO-67 as well as GSB recovery of Ru-Pt-UIO-67 can all be fit by the same three-exponential decay function. The ES decay kinetic trace of Ru moiety in Ru-Pt-UIO-67 can also be fit by a three-exponential decay function. However, due to the presence of a long-lived decay component ($\gg$5 ns) which is beyond our OTA time window, we are not able to accurately determine the ET time from the fitting results. Instead, we compared the half lifetime of ES decay dynamics of Ru-moiety in both samples, which is 4.9 and 1.2 ns for Ru-UIO-67 and Ru-Pt-UIO-

67, respectively. The much shorter half lifetime of Ru-moiety ES in Ru-Pt-UIO-67 than Ru-UIO-67 suggests that ET occurs from excited Ru to Pt-moiety. Moreover, the half lifetime of GSB of Ru-moiety in Ru-Pt-UIO-67 (~4.9 ns) is longer than its ES decay, suggesting that the charge recombination process between the reduced Pt-moiety and the oxidized Ru-moiety is slower than ET process.

Table 4.3 Multiexponential fit parameters for TA experiments corresponding to the fits shown in Figure 4.5c.

	wavelength	A_1(%)	τ_1(ps)	A_2(%)	τ_2(ps)	A_3(%)	τ_3
Ru-UIO-67	514 nm 634 nm	14.7	63.6	33.8	2440	51.5	>>5ns
Ru-Pt-UIO-67	525 nm 654 nm	14.7 26.1	63.6 74.2	33.8 52.5	2440 2130	51.5 21.4	>>5ns

The formation of the charge separated state in Ru-Pt-UIO-67 MOF due to ET from Ru- to Pt-moiety was further supported by probing the photoinduced electron density change at Pt center following the excitation of Ru-moiety using X-ray transient absorption (XTA) spectroscopy. Figure 4.6 shows the Pt L_3-edge XANES spectra of Ru-Pt-UIO-67 before (laser-

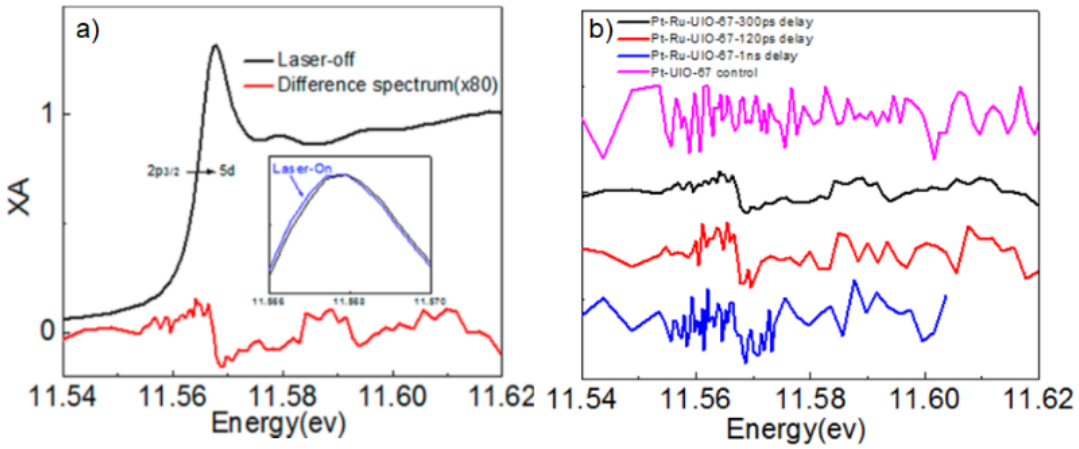

Figure 4.6 (a) XANES spectrum of Ru-Pt-UIO-67 at Pt L3-edge (black plot). The difference XANES spectrum (red plot), obtained by subtracting the laser-off spectrum from laser-on spectrum (300 ps after excitation), is also shown in the figure. Inset shows enlarged laser-on and laser-off spectrum. (b) The difference XANES spectrum of Pt-UIO-67(pink , ave 12 scan) and Ru-Pt-UIO 67 at 120ps (red, ave 30 scan), 300ps (black, ave 55 scan), 1ns(blue, ave 12 scan) delay

off spectrum, black plot) and 300 ps (laser-on spectrum, not shown) after 480 nm excitation. The transient signal due to laser excitation was clearly observed in the difference spectrum (red plot) obtained after subtracting the laser-off spectrum from the laser-on spectrum. The positive feature at 11.565 keV where $2p_{2/3}$ to 5d transition occurs indicates that the edge of Pt center shifts to lower energy, supporting the formation of reduced Pt center. The reduction of Pt center due to photoexcitation of Ru-moiety is further confirmed by the negative signal at 11.568 keV which corresponds to the reduced intensity of the white line amplitude, i.e., decreased oxidation state of Pt due to photoexcitation. As shown in Figure 4.6b, similar difference shows up at different delay times while no difference was observed for Pt-UIO-67 control sample. These results unambiguously confirm the ET process from excited Ru to Pt-moiety, consistent with OTA results above.

4.3 Conclusion

In summary, we have synthesized a hybrid Zr-MOF with simultaneously incorporated molecular Ru-photosensitizer and Pt-catalyst, which is highly active, robust, and recyclable for catalyzing proton reduction to generate H_2 reaction. Using the

combination of advanced ultrafast OTA and XTA spectroscopy, we investigated the CS dynamics in this hybrid MOF. We show that CS in Ru-Pt-UIO-67 MOF occurs through ET from excited Ru- to Pt-moiety, which unambiguously unraveled the fundamental roles of the incorporated homogeneous components in the heterogeneous MOF matrix for photocatalytic reaction, providing important guidance in rational design of hybrid MOF systems for solar to fuel conversion.

Chapter 5.

REAL-TIME VISUALIZATION OF ACTIVE SPECIES IN A SINGLE-SITE METAL-ORGANIC FRAMEWORK PHOTOCATALYST

5.1 Introduction

The direct conversion of solar energy to clean fuel as alternatives to fossil fuels is a desirable approach to address the global energy and environmental problems.[203-207] Hydrogen generation through water splitting is an emerging strategy of doing so that has attracted great attention, yet its development is largely hampered by the difficulty in efficient integration of multiple resource-intensive processes, i.e., light absorption, charge separation, and finally utilization of the photogenerated carriers to drive water splitting. Homogeneous solution-based systems comprising molecular photosensitizer (PS) and catalysts have naturally attracted much attention because of their merit in synthetic control over functional tunability and selectivity.[161, 208-211] However, their limited stability and efficiency remain a major challenge. In contrast, heterogeneous systems have shown beneficial features in long term durability and high catalytic activity.[166, 168-169] However, these materials not only lack design flexibility but also suffer from the difficulty of characterizing their mechanistic functions, rendering poor understanding of the origins behind their remarkable catalytic efficiency.

Because of their unique capability in combining the most advantageous features of

heterogeneous and homogeneous catalysts, metal organic frameworks (MOFs) are one of the best solutions to the above-mentioned stability and efficiency issues.[25, 27, 212-214] MOFs have the ability to incorporate homogeneous catalytic components in their heterogeneous matrix to achieve isolated active sites.[67, 171-173, 215] As such, MOFs can offer the same level of advantages as homogeneous catalysts while the robustness of the catalysts are increased. In addition, MOFs are built from periodic organic bridging ligands and inorganic nodes with tunable pore structure and functional components, which not only allows precise determination of the nature of the incorporated catalytic active sites but also opens up the possibility to engineer MOF catalytic sites in a defined manner.[175, 216-217]

For these reasons, an increasing number of systems that demonstrate successful application of MOFs in photocatalysis, with either a molecular PS or a molecular catalyst incorporated in the structure, have emerged. For example, photosensitizers such as porphyrin,[141, 178-180, 217] Ru complexes,[142, 182-184] tetraphenylethylene,[185] etc. have been successfully incorporated into MOFs for their beneficial photophysical properties. Meanwhile, molecular catalysts based on Ru,[186] Re,[187-188] Ir,[173, 187] Co,[60, 171-172] Fe,[189-190] Rh,[67, 218] Pt,[55, 184, 191] Pd,[219] have been introduced into the MOF structure and demonstrated catalytic activities. Despite this progress, there are only two examples that reported the immobilization of both molecular photosensitizers (RuDCBPY,[184] Ir(III)DCBPY[191]) and molecular catalysts (PtDCBPY) into the framework structure, both of which indeed showed enhanced activities for H_2 generation compared to their corresponding homogeneous counterpart. Offering their

large potential as efficient photocatalytic systems for solar fuel conversion as well as the ease for fundamental studies of MOF structure−catalytic function relationships, such single solid platform are especially ripe targets for further development.

In this work, we report a new single-site MOF system that incorporates a molecular catalyst based on earth-abundant metal and Ru-based PS to UIO-67(bpy), which not only demonstrates exceptional catalytic activities but also is recyclable and reusable for H_2 evolution reaction (HER). More importantly, we established the fundamental structure−function relationships of this system for HER examined under standard catalytic conditions. Using in situ X-ray absorption spectroscopy, we identified the intermediate species that determines the rate-limiting step and unraveled the origins of induction period, a complication that has long plagued mechanistic investigations in catalysis. Using time-resolved absorption spectroscopy, we elucidated the fundamental origins of light harvesting and charge-transfer dynamics, the properties that essentially dictate the function of this system for photocatalysis.

5.2 Results and discussion

As shown in Figure 5.1a, Co-Ru-UIO-67(bpy) was synthesized according to previous published protocols[220-221] by mixing $ZrCl_4$ (50.0 mg, 0.21 mmol), 2,2-bipyridine-5,5-dicarboxylic acid (H_2bpdcy) (45.0 mg, 0.19 mmol), Rudcbpy ($[Ru(dcbpy)\text{-}(bpy)_2]Cl_2$ （10.0 mg, 0.012 mmol), $CoCl_2$(25.0 mg, 0.19 mmol), and glacial acetic acid (93 μL, 1.6 mmol) in DMF (20 mL). Rudcbpy was prepared according to the previously published method.[222] As controls, UIO-67(bpy), Ru-UIO-

67(bpy), and Co-UIO-67(bpy) were also synthesized under similar conditions.

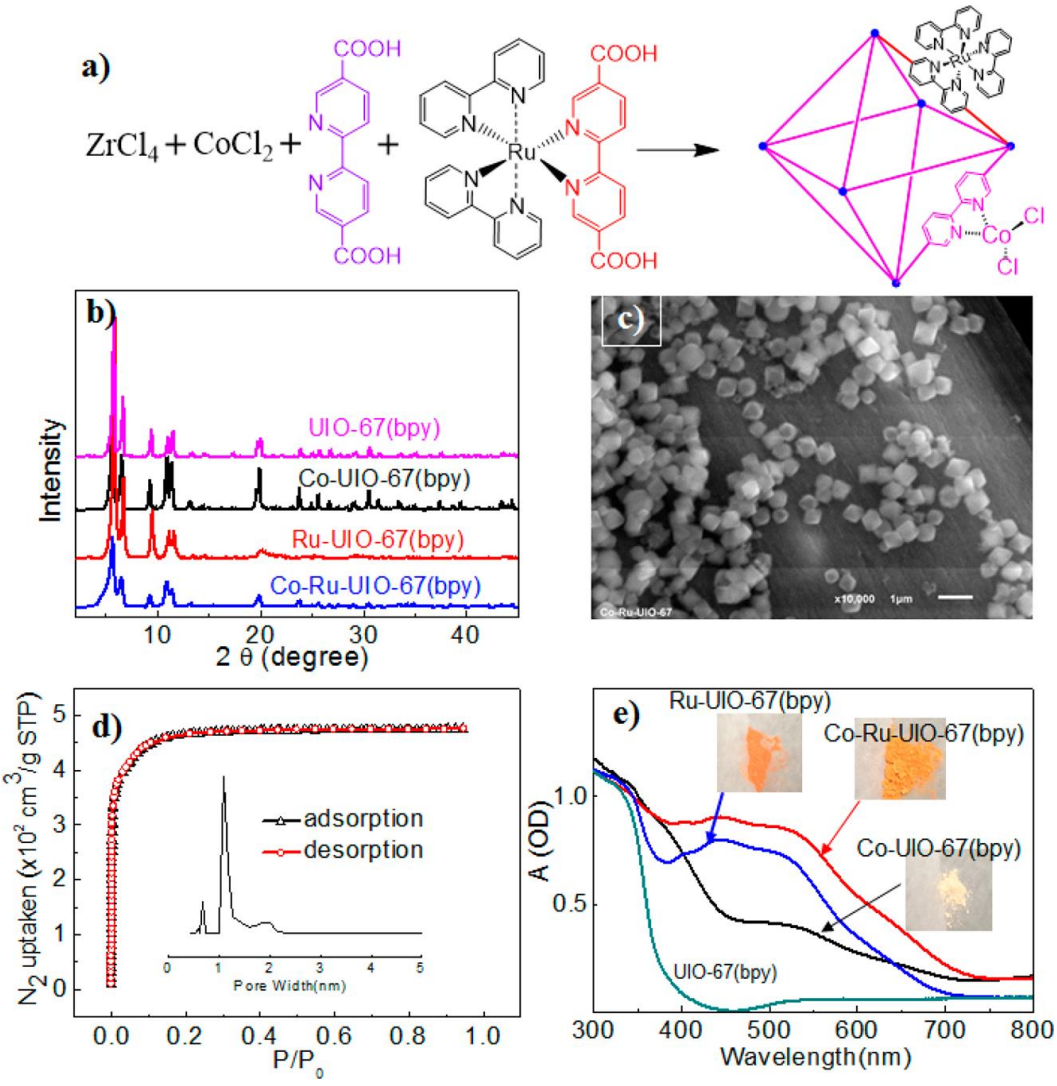

Figure 5.1 (a) Synthetic scheme of Co-Ru-UIO-67(bpy). XRD patterns (b) and diffuse reflectance spectra (e) for UIO-67(bpy), Co-UIO(bpy), Ru-UIO(bpy), and Co-Ru-UIO(bpy). (c) SEM image of Co-Ru-UIO-67(bpy). (d) N_2 adsorption isotherm and pore size distribution (inset) of Co-Ru-UIO-67(bpy).

The X-ray diffraction (XRD) patterns of these MOFs (Figure 5.1b) agree well with the patterns for UIO-67, suggesting that the crystallinity of these MOFs is retained after incorporation of molecular complexes.[223] Scanninge electron microscopy (SEM)

images of Co-Ru-UIO-67(bpy) (Figure 5.1c) show that the sample exhibits an octahedral crystalline structure with particle size ~500 nm. The porous structure of Co-Ru-UIO-67(bpy) was confirmed by Brunauer−Emmett−Teller (BET) analysis. As shown in Figure 1d, the surface area and pore size of Co-Ru-UIO-67(bpy) are 1781 m^2/g and 1.65 nm, respectively, which are close to those of UIO-67(bpy) (Figure 5.2) and comparable to literature data.[224] The presence of Ru and Co complexes was supported by diffuse reflectance ultraviolet−visible spectroscopy. As shown in Figure 5.1e, the additional broad absorption in the range of 350−700 nm in Co-Ru-UIO-67(bpy) compared to that of UIO-67(bpy) is consistent with the absorption features of Co complex in Co-UIO-67(bpy) and Ru complexes in Ru-UIO-67(bpy) and thus can be attributed to the absorption resulting from Co- and Ru-complexes incorporated into UIO-67(bpy). The concentrations of Co measured by inductively coupled plasma mass spectrometry (ICP-MS) and Ru measured by atomic absorption spectroscopy in Co-Ru-UIO-67(bpy) are 5.68×10^{-7} and 1.08 × 10−7 mol/mg, respectively, corresponding to the elemental ratio of Co:Ru = 5.26.

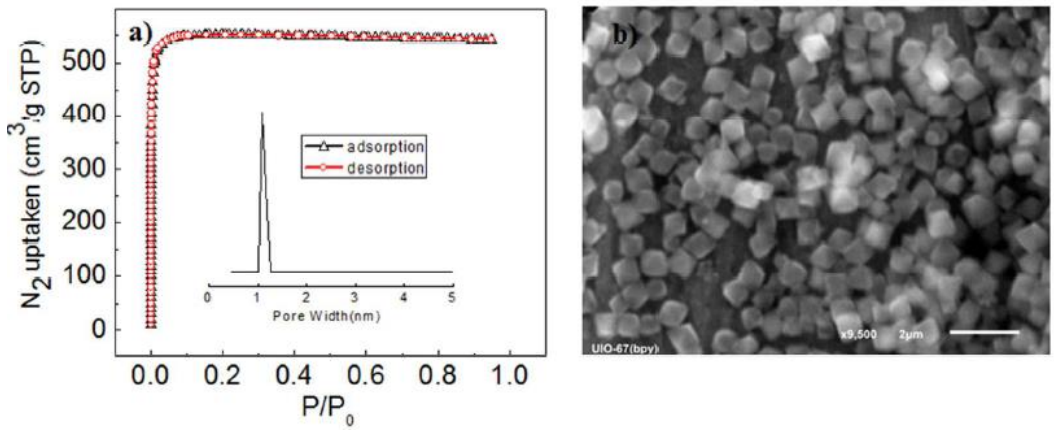

Figure 5.2 (a) N2 adsorption isotherm and pore size distribution (inset) of UIO-67(bpy). (b) SEM image of UIO-67(bpy).

The direct incorporation of Co complex into UIO-67(bpy) structure as well as its local structure at Co center was confirmed by steady-state X-ray absorption spectroscopy (XAS) measured at Advanced Photon Source, Argonne National Laboratory. Figure 5.3a compares X-ray absorption near-edge structure (XANES) spectra for Co-UIO-67(bpy) and Co-Ru-UIO-67(bpy) at Co K-edge. The XANES spectra of two reference samples with different geometry, i.e., the distorted tetrahedral Co complex (Co(6,6′-dimethyl-2,2′-bipyridine)Cl_2, abbreviated as Co(dmbpy)Cl_2), and CoO (octahedrally coordinated Co center), are also shown in Figure 5.3a in order

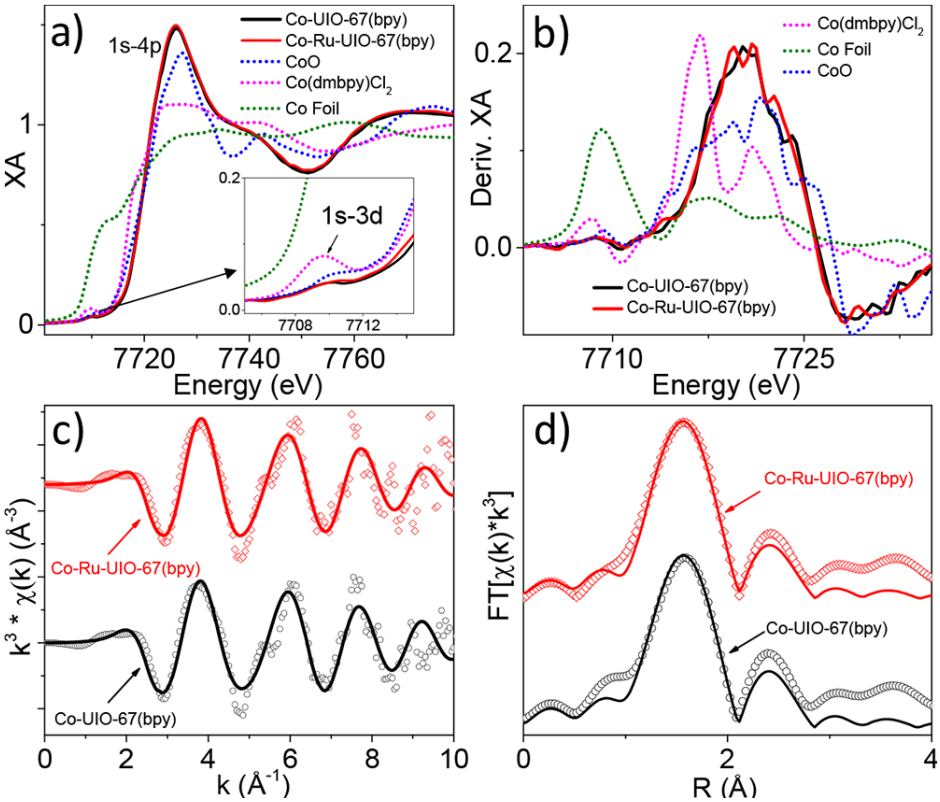

Figure 5.3 Co K-edge XANES spectra of Co-UIO-67(bpy) and Co-Ru-UO-67(bpy) samples (solid lines) and Co^{II}, Co^0 reference compounds (dotted lines) (a) and their first derivative spectra (b). The K-space (c) and Fourier-transformed R-space (d) spectra compared with data as open points and FEFF fits as solid lines. Inset of panel A shows enlarged pre-edge feature.

to correlate the spectral shape with local structure. The spectrum of Co(dmbpy)Cl_2 exhibits a prominent pre-edge feature corresponding to the dipole-forbidden 1s−3d transition (inset of Figure 5.3a), supporting the non-centrosymmetric geometry about Co due to distorted tetrahedral structure.[139] In contrast, the XANES spectrum of octahedral CoO presents a relatively weak pre-edge feature due to centrosymmetric geometry at Co center.[225-226] Both Co-UIO-67(bpy) and Co-Ru-UIO-67(bpy), which have XANES spectra that are nearly identical to one another, show XANES features similar to those of CoO, suggesting that Co centers in both samples likely possess octahedral geometry. Moreover, the edge energy of the XANES spectra of both MOF samples, as shown in the first derivative XANES spectra (Figure 5.3b), show excellent agreement with the edge position of CoO reference, suggesting that Co centers in MOF samples retain +2 oxidation state.

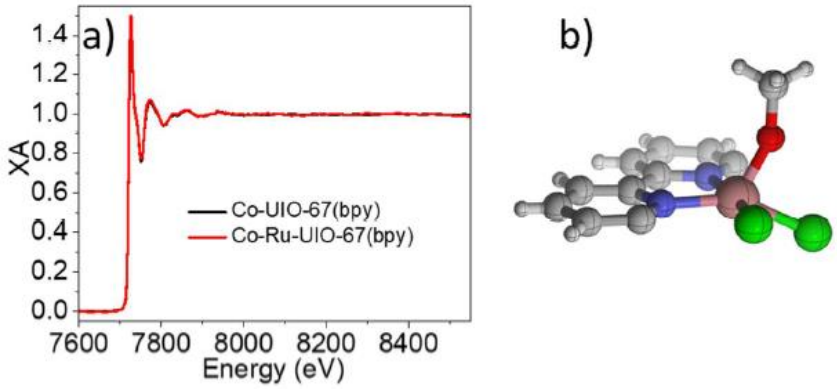

Figure 5.4 Full EXAFS spectra of Co-UIO-67(bpy) and Co-Ru-UIO-67(bpy) (a) and graphic of EXAFS fit model (b). (Grey=C, Blue=N, Pink=Co, Green=Cl, Red=O, White=H). Hydrogens were excluded from FEFF calculation.

The local geometry of Co^{II} center in Co-UIO-67(bpy) and Co-Ru-UIO-67(bpy) samples, revealed by the XANES studies detailed above, indicates that Co is coordinated by more than four atoms, implying that solvents may have participated in coordination to Co center in the $Co(bpy)Cl_2$ moiety. This assignment is further supported by a recent literature report,[227] in which single-crystal X-ray diffraction data confirmed the presence of 5- and 6-coordinated Co sites in a Zr-based MOF with $CoCl_2$ metalation of its bipyridine linkers due to coordination of Co to either one or two solvent molecules. In order to quantitatively support this assignment, the full EXAFS energy range spectra (Figure 5.4a) were fit using the Demeter X-ray absorption analysis package.[228] The FEFF input model was built from the crystal structure of $Co(dmbpy)Cl_2$ by adding an additional solvent molecule (methanol) coordinated to Co. The scattering amplitude of the Co-solvent single scattering vector in the first shell of atoms about Co was parametrized to allow its variation with the other fitting parameters and was interpreted as the average solvent coordination number. The EXAFS fitting parameters are listed in Table 5.1 and a graphic of the fitting model in Figure 5.4b. The EXAFS data and the resulting best fits in K-space and R-space are shown in panels c and d of Figure 5.3, respectively. From the best fitting results, the bond distance of Co to N atoms on bipyridine in Co-UIO-67(bpy) and Co-Ru-UIO-67(bpy) is determined to be 2.08 and 2.09 Å, respectively, and the Co−Cl distance for both samples is 2.29 Å. The Co-to solvent atom distance is 1.92 Å with coordination number of approximately 1.1 for both samples. The Co−N distances are within the range of distances reported in the literature (2.09 and 2.17 for 5-

coordinate Co; 2.01 and 2.13 for 6-coordiate Co),[227] as are the Co−Cl distances (2.27 and 2.31 for 5- coordinate Co; 2.27 and 2.33 for 6-coordinate Co), suggesting the validity of our fitting model. With these insights into the structure and properties of Co-Ru-UIO-67(bpy), in the following sections, we investigate its catalysis activity for HER and fundamentally characterize its catalytic mechanism.

Table 5.1 EXAFS fitting results for powder Co-UIO-67(bpy) and Co-Ru-UIO-67(bpy) samples corresponding to the fit figures in Figure 5.3 c,d. The asterisk on Co-Solv. coordination number indicates that it was fit along with the distance parameters as discussed in the main text. The bottom two entries (Co-C single scattering path and Co-C-N obtuse triangle path) were included due to high rank in the FEFF calculation and each include two paths separated by commas (one for each C atom adjacent to the N in bipyridine) which were fit with the same fit parameters. (R ± 0.02 Å; σ2 ± 0.001 Å2). Fit model is visualized in Figure 5.4b. Additional parameters: ΔEo = -4.386, S02 = 1 (all paths) for both samples.

	Co-UIO-67(bpy)			Co-Ru-UIO-67(bpy)		
Vector	N	R(Å)	σ^2x10^{-3} (Å^2)	N	R(Å)	σ^2x10^{-3} (Å^2)
Co-N	2	2.09	1	2	2.08	1.5
Co-Solv.	1.14*	1.91	1	1.10*	1.92	1.5
Co-Cl	2	2.29	9	2	2.29	9
Co-C	2,2	2.82,2.98	1	2,2	2.79,2.95	1
Co-C-N	4,4	3.30,3.37	1	4,4	3.27,3.34	1

The photocatalytic performance of Co-Ru-UIO-67(bpy) for HER was tested under the illumination of a 447 nm LED lamp in the mixture of H_2O and acetonitrile solution. The reaction conditions, including sacrificial donors, the concentrations of sacrificial donors and MOFs, proton sources, the ratios of catalyst to PS, and LED powers were systematically optimized to reach the maximum amount of H_2 per gram of catalyst (Figure 5.6). The optimized conditions for the Co-Ru-UIO-67(bpy)

photocatalytic system is under Co:Ru = 5.26:1 of Co-Ru-UIO-67(bpy) (1.0 mg), 0.4 mL of H_2O, 0.3 mL of TEOA, and 9 mW LED power in 3 mL acetonitrile solution. Control experiments omitting TEOA or H_2O did not yield H_2, suggesting their key roles as sacrificial donor and proton source (Figure 5.5). For comparison, Co-UIO-67(bpy) or Ru-UIO-67(bpy) with the same metal loading as that in Co-Ru-UIO-67(bpy) yields only minimal amount of H_2 under identical conditions (Figure 5.5), indicating incorporating both Ru PS and Co catalysts into the MOF structure is essential for HER. Under these conditions, the HER activity of Co-Ru-UIO-67(bpy) achieves 27853 μmol H_2/g of MOF after 40 h (Figure 5.7a), which accounts for TON of 99 based on Co and is comparable to previous MOF systems containing Pt complexes as catalysts.[184, 192] The current system, however, benefits from the use of earth-abundant Co complex as catalysts.

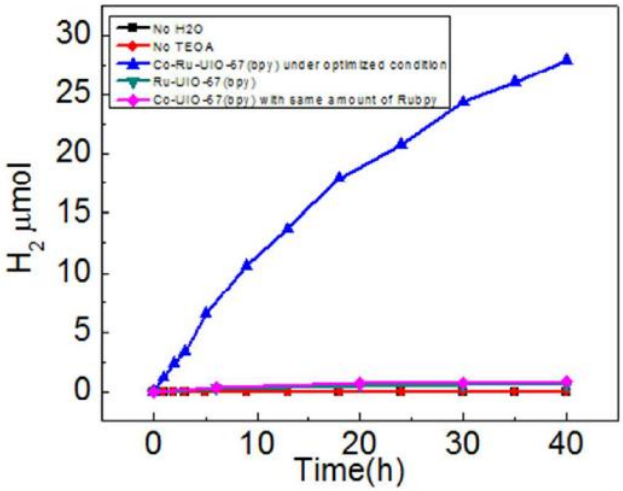

Figure 5.5 Time profile of H_2 generation under optimized condition: without H_2O (black) or TEOA (red), Ru-UIO-67(bpy) (green) and Co-UIO-67(bpy) (pink) as control.

To evaluate the duration of the Co-Ru-UIO-67(bpy) catalytic system, the recycling

tests were explored by collecting MOFs after each 5 h illumination via centrifugation and dispersal in a fresh catalysis solution. Remarkably, Co-Ru-UIO-67(bpy) shows unchanged activity during the recycling experiments for at least three runs.

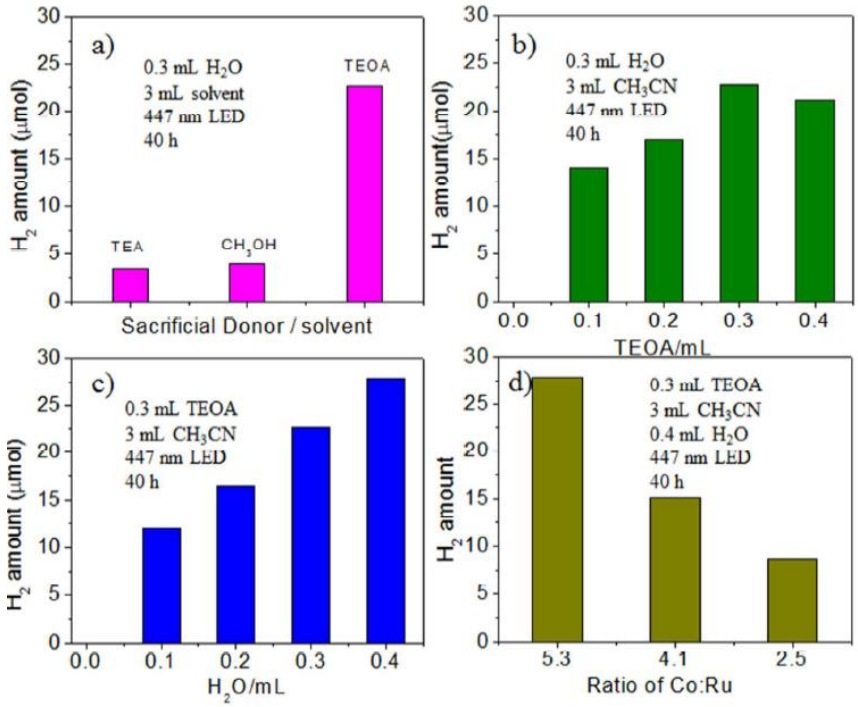

Figure 5.6 Optimization of light-driven H_2 evolution reaction. (a) The amount of H_2 produced using different solvent and sacrificial donor. (b) The amount of H_2 produced as a function of TEOA concentration. (c) The amount of H_2 produced as a function of H_2O concentration. (d) The amount of H2 produced as a function of Co:Ru ratio.

Furthermore, the concentration of Co in the supernatant solution before and after catalysis was measured using ICP-MS to examine the possibility of Co leaching. While ~3.2% of Co is leached during catalysis process, HER experiments using supernatant solution under the same conditions did not yield detectable amount of H_2, ruling out the possibility that the observed activity is due to leached Co. To further confirm the integrity of the MOF photocatalyst after catalysis, ex situ XAS was

performed in which the MOF photocatalyst was removed from the catalysis solution after 20 h and washed via centrifugation. The XANES and EXAFS results (Figure 5.8 and Table 5.2) indicate that the local structure of Co remains unchanged after catalysis. The significantly improved activity and stability suggest the important role of the framework in both boosting the catalytic activity of molecular catalysts and stabilizing the catalytic species, which prompted us to investigate the mechanistic origins of its catalytic function.

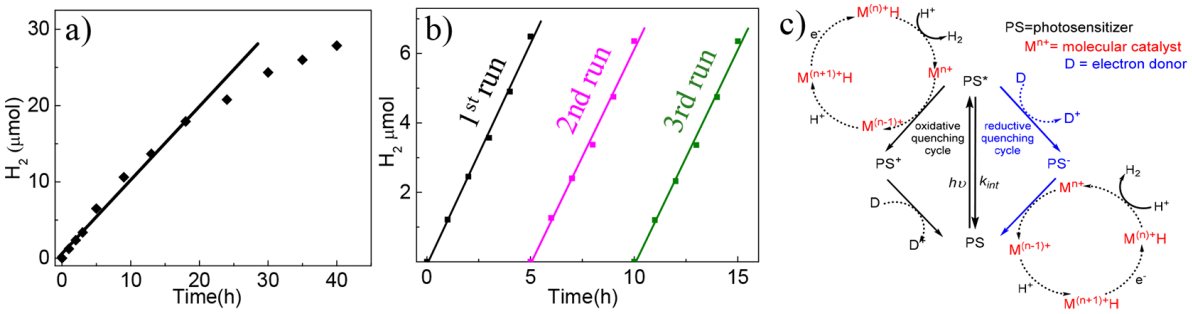

Figure 5.7 (a) Time profile of H2 production by Co-Ru-UIO-67(bpy) under 447 nm LED illumination at 9 mW in the presence of TEOA (0.3mL) and H2O (0.4 mL) in acetonitrile solution (3 mL). (b) Recycling of Co-Ru-UIO-67(bpy) catalyst after multiple 5 h experiments. (c) Commonly accepted catalytic pathway for photoinduced H2 generation with molecular photosensitizer (PS) and catalysts.

As shown in Figure 5.7c, a commonly accepted scheme for photoinduced proton reduction is initiated with light absorption by PS, which is followed by two sequential charge separation (CS) processes, where the electrons in the excited PS transfer to the catalyst and holes are extracted to electron donors through either the reductive or oxidative cycle. Consequently, it is crucial to have a systematic study of these light-harvesting and CS dynamics in Co-Ru-UIO-67(bpy) to gain mechanistic insight of its

function for catalysis.

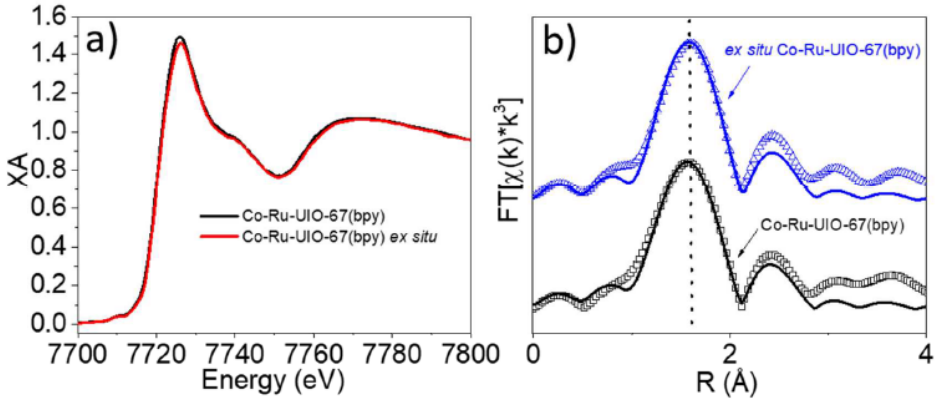

Figure 5.8 XANES region (a) and R-space EXAFS fit figures (b) for Co-Ru-UIO-67(bpy) compared to ex situ sample after 20 hours of catalysis.

Table 5.2 EXAFS fit results for ex situ Co-Ru-UIO-67(bpy) after catalysis using the same model described in Table 5.1 heading. The corresponding fit figure is shown in Figure S5. Additional parameters: ΔEo = -4.386, S02 = 1 (all paths).

	***ex situ* Co-Ru-UIO-67(bpy)**		
Vector	N	R(Å)	$\sigma^2 x10^{-3}$ (Å^2)
Co-N	2	2.08	1.5
Co-Solv.	1.10*	1.92	1.5
Co-Cl	2	2.28	7
Co-C	2,2	2.80,2.96	1
Co-C-N	4,4	3.27,3.34	1

Transient absorption (TA) spectroscopy was used to investigate the excited state (ES) and CS dynamics of the Co-Ru-UIO-67(bpy) MOFs. Panels a and b of Figure 5.9 show the femtosecond TA spectra of Ru-UIO-67(bpy) and Co-Ru-UIO-67(bpy), respectively, following 447 nm excitation. Ru-UIO-67(bpy) was used as control sample to illustrate the intrinsic ES dynamics of Ru complex in UIO-67(bpy) framework without the presence of Co catalyst species. The TA spectra of Ru-UIO-

67(bpy) show two main spectral features, i.e., a negative band centered at 513 nm and a broad absorption band at >560 nm, which can be attributed to the ground-state bleach (GSB) and ES absorption of Ru complex, respectively. GSB recovery follows the same kinetics as ES decay (Figure 5.9c), together with the presence of an isosbestic point at 556 nm, suggesting that decay of ES molecules to their GS is the only recombination process. The TA spectra of Co-Ru-UIO-67(bpy) (Figure 4b) also show a GSB band and a broad ES band. However, the center of the GSB band in the spectra of Co-Ru-UIO-67(bpy) shows a prominent blue shift with respect to that of Ru-UIO-67(bpy). This blue shift cannot result from the direct excitation of Co complex as negligible TA features were observed in the TA spectra of Co-UIO-67(bpy) following excitation under the same conditions. Instead, we attributed this blue shift to the formation of a CS state between Ru- and Co-moieties, which was based on not only the literature reports with similar spectral shifts observed in many donor−acceptor systems,[229] but also our experimental observations discussed below.

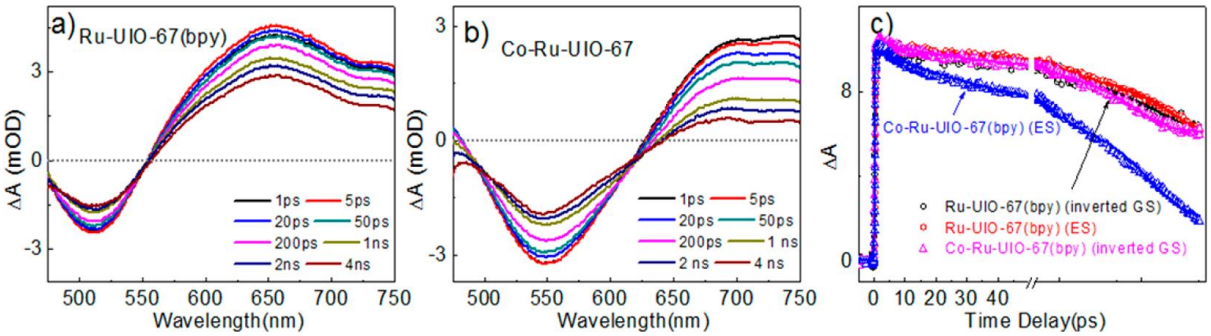

Figure 5.9 Femtosecond TA spectra of Ru-UIO-67(bpy) (a) and Co-Ru-UIO-67(bpy) (b). (c) The comparisons of the GSB recovery and ES decay kinetics between Ru-UIO-67(bpy) and Co-Ru-UIO-67(bpy). The GSB recovery kinetics for both Ru-UIO-67(bpy) and Co-Ru-UIO-67(bpy) were inverted for better comparison.

As shown in Figure 5.9c, while the kinetics of GSB recovery and ES decay is similar in the TA spectra of Ru-UIO-67(bpy), ES kinetics decays much faster than the ESB recovery in the spectra of Co-Ru-UIO-67(bpy). Moreover, while the GSB kinetics in Co-Ru-UIO-67(bpy) remains similar to that in Ru-UIO-67(bpy), the ES kinetics is much faster in the former than the latter (Figure 5.9c). These results, similar to the typical features accounting for ET process from Ru complex to electron donors reported previously,[230] suggest that the ET process occurs from Ru complex to Co complex in Co-Ru-UIO-67(bpy). The kinetics traces for ES decay and GSB recovery of Ru-UIO-67(bpy) as well as the GSB recovery of Co-Ru-UIO-67(bpy) can be fit by the same three-exponential decay function with fitting parameters listed in Table 5.3. The ES decay of Co-Ru-UIO-67(bpy) can also be fit by a three-exponential decay function (Table 5.3). Unfortunately, we are not able to accurately determine the ET time from the fitting results because of the presence of a long-lived decay component (≫5 ns) which is beyond our TA time window. Nevertheless, we can conclude that the ET process is much faster than the charge recombination process, as can be seen from Figure 5.9c where the ES decays much faster than the inverted GSB of the Ru complex in Co-Ru-UIO-67(bpy).

Table 5.3 Multiexponential fit parameters for TA experiments corresponding to the fits shown in Figure 5.8c, 5.8d.

	Wavelength (nm)	A_1(%)	τ_1(ps)	A_2(%)	τ_2(ps)	A_3(%)	τ_3
Ru-UIO-67(bpy)	510nm 650nm	13.7	111	30.3	2880	56	>>5ns
Co-Ru-UIO-67(bpy)	550nm	13.7	111	30.3	2880	56	>>5ns
	693nm	32.1	49.3	47.6	1300	20.3	

Furthermore, the Stern−Volmer experiment (Figure 5.10) indicates that reductive quenching of Ru-UIO-67(bpy) by TOEA occurs on a microsecond time scale (~5 μs), which is much slower than the ET process from Ru complex to Co complex in Co-Ru-UIO-67(bpy). Following the scheme in Figure 5.7c, we believe that the oxidative quenching cycle is preferred after photoexcitation of Co-Ru-UIO-67(bpy) under catalysis conditions.

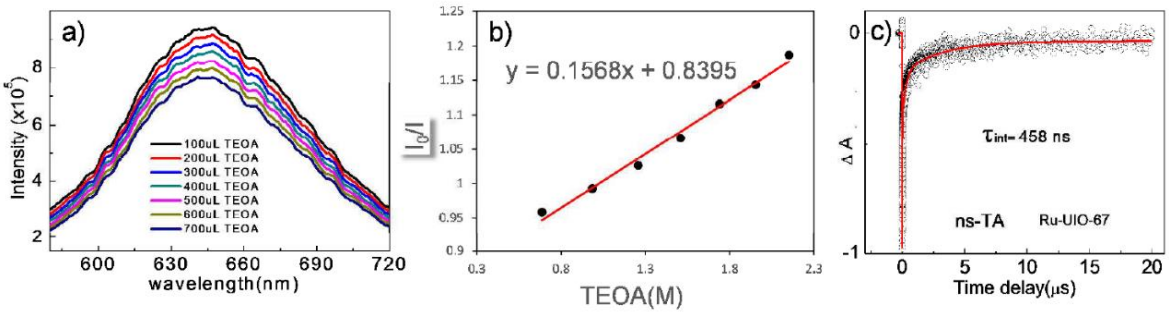

Figure 5.10 Stern-Volmer plot (b) was obtained by using unquenched emission signal divided by the quenched signal (a) against the concentration of quencher. From the slope and the lifetime of Ru-UIO-67, which we extracted from ns-TA GSB decay kinetics (c), the reductive quenching rate is 3.423x105 M-1S-1. Under the optimized condition with TEOA concentration of 0.568 M, the estimated time constant for reduction quenching is 5.14 μs.

While the CS process above is certainly the first step that initiates the photocatalytic reaction, the complete catalytic cycle includes more critical steps that lead to ultimate H_2 generation. As shown in Figure 5.7c, following the CS process, the catalytic pathway includes three more steps including two protonation processes and one reduction process. It is essential to identify the transient species involved in these processes in order to fully understand the catalytic mechanism. In this context, in situ XAS, a powerful tool that can directly reveal the oxidation state and structural change

of Co catalysts, was used to measure the intermediate species under the standard catalytic conditions.

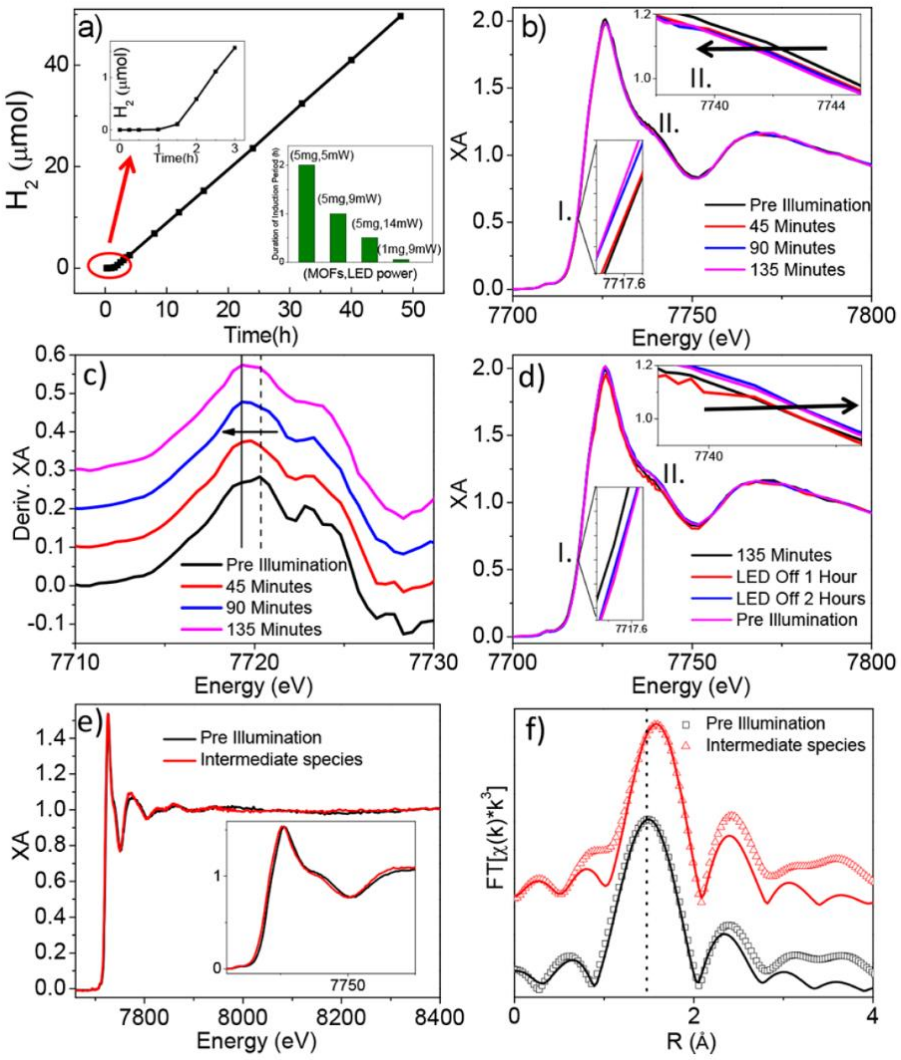

Figure 5.11 (a) Time profile of H_2 production by Co-Ru-UIO-67(bpy) under 447 nm LED illumination at 9 mW in the presence of TEOA (0.3 mL) and H2O (0.4 mL) in acetonitrile solution (3 mL). The inset is the duration of induction period as a function of Co-Ru-UIO-67(bpy) concentration and LED power. (b) In situ XANES spectra of Co-Ru-UIO-67(bpy) as a function of irradiation times. The insets are enlarged regions I and II. (c) The offset first derivative of in situ XANES spectra. (d) In situ XANES spectra of Co-Ru-UIO-67(bpy) after LED was switched off to observe change back to original spectrum. The comparison of XANES (e), EXAFS (inset of e), and EXAFS spectra in R space (f) of Co-Ru-UIO-67(bpy) before illumination and the intermediate species formed after induction period ends.

In situ XAS spectra at Co K-edge were collected at beamline 12-BM at Advanced Photon Source, Argonne National laboratory. The experiments were performed in a custom designed Teflon cell equipped with a Kapton front window for X-ray irradiation and quartz rear window for LED lamp illumination, and 5 mg of Co-Ru-UIO-67(bpy) was used in the in situ experiment to obtain an appropriate level of XAS signal in fluorescence mode. Under these conditions, an induction period (~2 h) was observed before the production of H_2 (Figure 5.11a). The induction period can be observed only under certain conditions; as shown in Figure 5.11a (inset), the induction period is strongly dependent on LED power and MOF concentration, where high LED power and low MOF concentration decrease the duration of the induction period until it cannot be resolved at the optimized conditions (1 mg of MOFs, 9 mW LED power). Nevertheless, the long induction period under current conditions is beneficial for unravelling the catalytic mechanism using XAS.

Figure 5.11b shows the in situ XANES spectra of Co-Ru-UIO-67(bpy) to track the change of oxidation state and structure at Co center during HER photocatalysis. Notable changes were observed in two regions of the spectrum, i.e., enlarged inset region I (edge feature) and region II (above-edge oscillations), where both features gradually shift to lower energy during catalysis. The edge shift to lower energy was further confirmed by comparing the first derivative spectra (Figure 5.11c), which can be attributed to the reduction of CoII to CoI during catalysis. The shift in above-edge oscillations (region II) to lower energy are indicative of lengthening in Co−L distances where L is any coordinating atom. This structural change is likely associated

with the reduction of Co center because larger degree of charge density on Co results in decreasing electrostatic attraction between Co center and ligand species, thus causing the larger bond distances observed.

It is interesting to note that the change of XANES spectrum stops after ~2 h, consistent with the time frame of induction period, suggesting that the structural change observed above is associated with the induction period. These results also suggest that the induction period must be related to a chemical change that occurs in the early portion of photocatalysis, namely, the formation of some intermediate chemical species that must build up before catalysis turnover occurs. Meanwhile, upon LED illumination, the original orange solution changes to a dark gray color, which occurs gradually until the induction period ends and occurs immediately in the system when the induction period is not observed, suggesting that the color change of the MOF particles is also correlated with the induction period. When the LED light is turned off, the solution color can slowly return to its original color, which is accompanied by the returning of the XANES spectra to the original state (Figure 5.11d). These results together suggest that the intermediate species accumulated after induction period is the active species for photocatalytic reaction rather than permanent degradation of the sample.

In order to uncover the nature of this intermediate species, we collected the in-situ EXAFS spectra of the system after the induction period ends. As shown in Figure 5.11e, the whole spectrum of the intermediate species moves to lower energy compared to the spectrum before illumination, consistent with the above in situ

XANES results, suggesting that the intermediate species is Co(I) state with elongated

Table 5.4 EXAFS fit results for in situ experiment performed using the process described in chapter 2. Additional parameters: WEo = -4.386, S_0^2 = 1 (all paths) for Pre-Illumination, ΔE_0 = -5.580, S_0^2 = 1 (all paths) for Intermediate Species.

	Pre Illumination			Intermediate Species		
Vector	N	R(Å)	$\sigma^2 x10^{-3}$ (Å^2)	N	R(Å)	$\sigma^2 x10^{-3}$ (Å^2)
Co-N	2	1.98	1	2	2.11	1
Co-Solv.	0.38*	1.95	6	2.37*	1.94	6
Co-Cl	2	2.25	10	2	2.28	10
Co-C	2,2	2.76,2.92	1	2,2	2.80,2.96	1
Co-C-N	4,4	3.25,3.32	1	4,4	2.24,3.31	1

Co−L distance. The enlarged Co−L bond distance was further confirmed by the Fourier-transformed XAFS spectrum (Figure 5.11f), where the peak representing the first shell (Co−N) distance is shifted to larger distance during photocatalysis, in agreement with XANES observations. To quantitatively analyze the structure of the intermediate species, FEFF with the same model utilized above was used to fit the EXAFS spectrum. The resulting fitting parameters are listed in Table 5.4. It is noted that the pre-illumination parameters show a significantly shorter distance compared to the powder Co-Ru-UIO-67(bpy) sample as well as a lower solvent coordination number, although this result is unsurprising because the local structure of Co is sensitive to solvent environment as discussed above. Compared to the structure before illumination, the parameters of the intermediate species show significant increase in Co−N (1.98 Å increases to 2.11 Å) and Co−Cl (2.25 Å increases to 2.28 Å) distances in the first shell and increased Co−C distances in the second shell, in agreement with

qualitative observation of R space spectra. Additionally, it was observed that the solvent coordination number increased from 0.38 to 2.37 during catalysis, which we interpret as most Co atoms being uncoordinated before catalysis and most Co atoms being coordinated by two additional atoms during catalysis, considering the uncertainty in coordination number during the fit (ca. ± 0.5 atoms). The change in coordination number could be due to multiple scenarios such as the coordination of solvent molecules to Co^{I}, coordination of TEOA to Co^{I}, or coordination of byproducts to any remaining Co^{II} in addition to Co^{I}. As such, we cannot definitively assign this change. However, because of the long stability of the catalysis system and the results of ex situ EXAFS fitting, we can conclude that this coordination is a dynamic event during catalysis in solution and does not interfere with catalysis activity or permanently change the local structure of the catalytic Co center. Following the scheme presented in Figure 3c, the only possible intermediate species based on in situ experiments is Co^{I}, suggesting that the consumption of Co^{I} via protonation is likely the rate-determining step in HER photocatalysis. As a result, a long-lived Co^{I} species would certainly benefit HER reaction, which reasonably explains the observed superhigh H_2 generation efficiency, as efficient CS process, i.e., ultrafast ET with inhibited charge recombination, occurs from Ru PS to Co catalyst in our Co-Ru-UIO-67(bpy) system.

5.3 Conclusion

In summary, we report a new robust, cost-effective single-site MOF photocatalyst by

incorporation of Co active center and Ru-based photosensitizer moiety into the framework. This hybrid MOF not only exhibits exceptional hydrogen evolution activity from H2O/acetonitrile solution but also demonstrate recyclability for at least 15 h. Using the combination of advanced ultrafast absorption spectroscopy and in situ XAS, we not only captured the active intermediate species for catalysis, i.e., Co^{I} species formed after ET process from Ru PS to Co catalyst in MOF, but also uncovered that the consumption of this active species is the rate-limiting step in photocatalysis. We thus conclude that the long-lived Co^{I} species due to efficient CS process is essential for efficient H_2 generation. This is likely the direct result of the heterogeneous nature of MOFs, which not only enhance the durability of the incorporated PS and molecular catalyst significantly but also serve as versatile platform for efficient coupling of these functional components, enabling efficient solar-to-fuel conversion.

Chapter 6.

PHOTOINDUCED CHARGE SEPARATION AND STRUCTURAL DYNAMICS IN CE-TCPP METAL ORGANIC FRAMEWORKS

6.1 Introduction

The direct conversion of water or CO_2 by solar energy into fuel is a promising approach to address global energy and environmental issues.[231-233] However, it remains a great challenge to drive such reaction in an efficient way and an appropriate catalyst is highly desired to promote the reaction in an reasonable rate.[234] In the past decades, extensive efforts have been devoted to exploring visible light driving water splitting or CO_2 reduction by using either molecular metal complexes or heterogeneous catalysts based on semiconductors.[157, 235-236] For example, molecular systems based on noble metal complexes such as Ru,[237-238] Re[239-240] or Ir[241] have been used as CO_2 reduction catalysts. Moreover, a large number of homogeneous systems using Ru,[242] Fe[162] or Co[161, 243] have also been used as catalysts for water splitting. While these homogeneous systems have demonstrated high efficiency and selectivity for CO_2 reduction or water splitting, and can facilitate mechanistic analysis due to precise structure control, the further development of these systems is largely hampered by the use of noble metals, poor stability of the molecular catalyst, as well as the difficulty in recycling. On the other hand, heterogeneous semiconductor systems have shown great potential in long-term stability and can be easily recycled

but they typically suffer from poor structural flexibility as well as the difficulty in characterizing their mechanistic origins for photocatalysis.[166, 168, 244]

As an emerging class of nano-porous materials, metal organic frameworks (MOFs) offer a new opportunity by taking advantage of both homogenous and heterogeneous catalysts for photocatalysis. MOFs are created by assembling metal-containing secondary building units (SBUs) with organic linkers.[112, 245-246] With flexible metal SBUs and organic linkers, MOFs are able to integrate light-harvesting materials and catalysts into a single matrix.[182, 247-248] In addition, the high crystallinity and porous nature of MOFs may facilitate charge transport and diffusion of reactants during the photocatalytic reaction.[249-250] Due to these reasons, a large number of MOFs with built-in photosensitizer and molecular catalyst have been used for water splitting and CO_2 reduction.[251-257] However, majority of these work are centered on their catalytic performance and stability rather than fundamental mechanism. As these photocatalytic reactions heavily rely on the light harvesting and charge separation (CS) events after photoexcitation, it is essential to gain an intimate knowledge of these fundamental aspects,[196, 258-259] which is expected to provide guidance on engineering photoactive MOFs for solar-to-fuel conversion. In this work, we report the excited state and CS dynamics of a porphyrin-based Ce-TCPP MOF by femtosecond optical transient absorption spectroscopy (OTA) and X-ray transient absorption spectroscopy (XTA). We show that the excitation of Ce-TCPP MOFs leads to the formation of a long-lived charge separated state with ligand-to-metal cluster charge transfer character.

6.2 Results and Discussion

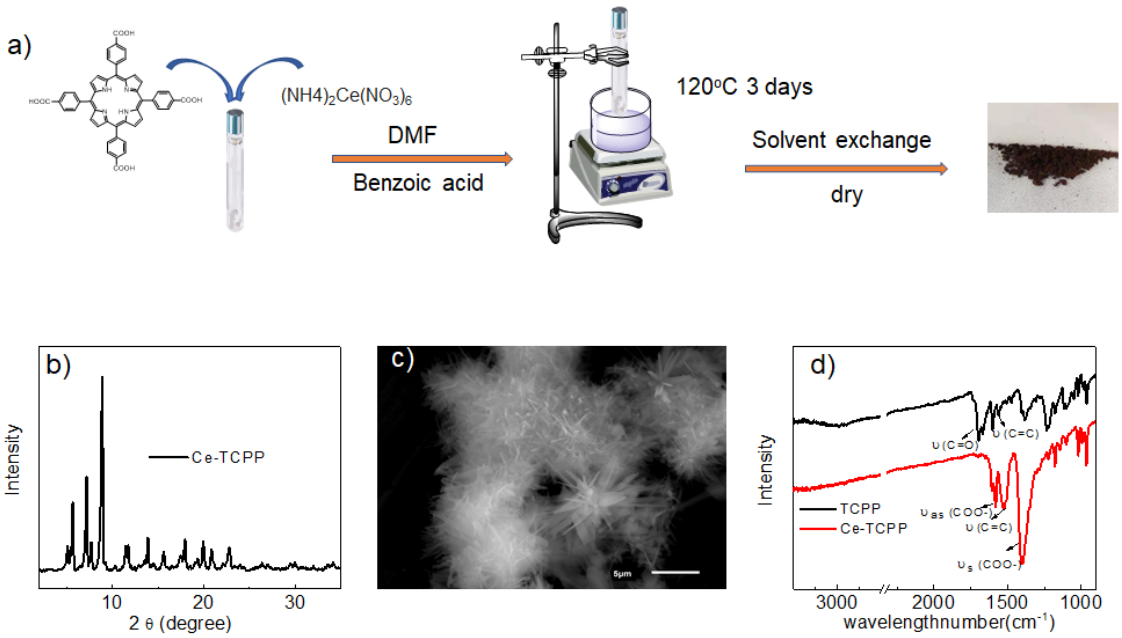

Figure 6.1 Synthetic scheme (a), XRD patterns (b), and SEM image (c) of Ce-TCPP. (d) Fourier-transform infrared (FT-IR) spectra of TCPP and Ce-TCPP.

As shown in Figure 6.1a, the 3D Cerium based MOFs (Ce-TCPP) was synthesized by the solvothermal reaction. The obtained product was characterized by Powder XRD (Figure 6.1b) and SEM (Figure 6.1c), which shows a needle-like shape. The porosity of Ce-TCPP MOFs was confirmed by N_2 sorption measurement (Figure 6.2). The BET surface area is 332.56 m^2/g, which was comparable to literature results of similar TCPP MOF.[260] The formation of Ce-TCPP MOFs was further supported by the Fourier-transform infrared (FT-IR) spectroscopy (Figure 6.1d), where we observed the disappearance of C=O stretching at 1700 cm^{-1} which is present in TCPP resulting from free -COOH, the shift of C=C valence vibration of phenyl rings from 1559 cm^{-1} to 1526 cm^{-1}, as well as the two new peaks at 1587 cm^{-1} and 1400 cm^{-1}, which can be

assigned to asymmetric and symmetric vibrational stretching of COO^-, respectively.[261-263] These results together suggest the successful coordination of carboxyl group in TCPP with Ce metal ion in Ce-TCPP MOFs.

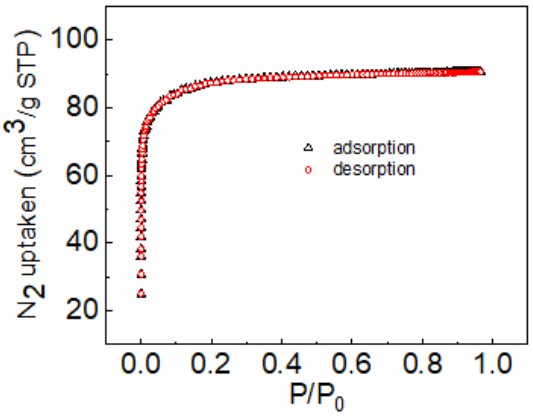

Figure 6.2 N_2 adsorption/desorption isotherm of Ce-TCPP.

In addition to the bulk structure, the local coordination environment at Ce center in Ce-TCPP MOFs was confirmed by X-ray absorption spectroscopy (XAS). The X-ray absorption near edge structure (XANES) spectra of Ce-TCPP MOFs and two reference samples, i.e. hexagonal $CeCl_3$ $7H_2O$ (Ce^{3+}) and cubic CeO_2 (Ce^{4+}), are shown in Figure 6.3a. The main feature at ~ 5725.5 eV in the spectrum of $CeCl_3$ is the absorption white line corresponding to the dipole allowed transition from Ce 2p to 5d mixed with $4f^1$ final state,[264] supporting that Ce in $CeCl_3$ has the trivalent state (Ce^{3+}). In contrast, XANES spectrum of CeO_2 exhibits two distinct features at ~ 5731 eV and 5737.5 eV, which can be attributed to the mixed-valence behavior of tetravalent Cerium (Ce^{4+}) in its final state ($4f^1 5dt_{2g}L$ and $4f^0 5d$. L denotes the oxygen 2p hole).[265] Unlike two reference samples, the XANES spectrum of Ce-TCPP MOF shows the

main absorption edge at 5725.5 eV and a weak feature at 5737.5 eV, which can be assigned to the $4f^1$ and $4f^0$ absorption peak, respectively, suggesting the co-existence of Ce^{3+}/Ce^{4+} valence state in Ce-TCPP MOF. This is further supported by the energy difference (~ 12 eV) between these two features, which agrees well with the Coulomb interaction of Ce 2p and Ce 4f orbitals.[266-268]

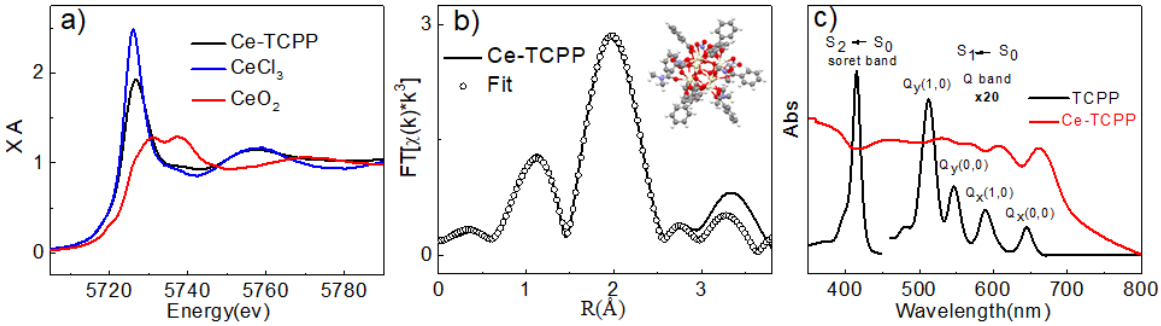

Figure 6.3 XANES spectra (a) of Ce-TCPP (black), $CeCl_3$ (blue) and CeO_2 (red). The Fourier-transformed R-space (b) spectra of Ce-TCPP (inset shows the fitting model). The data are shown as open points and FEFF fits are shown as solid lines. UV-visible absorption spectrum of TCPP (c) (black) and the diffuse reflectance spectrum of Ce-TCPP (red).

To gain deeper insight of the local coordination environment, we quantitatively fitted the extended X-ray absorption fine structure (EXAFS) spectrum of Ce-TCPP (Figure 6.4a) using Demeter X-ray absorption analysis package. The fitting parameters are listed in Table 6.1, and the EXAFS data and the resulting best fit in R-space and k-space are present in Figure 6.3b and Figure 6.4b, respectively. From the best fitting, the bond distance of Ce to O in Ce-TCPP was found to be between 2.20 Å to 2.55 Å. The Ce-O distances are within the range of distances reported in literature for Ce_6O_8 core (2.206–2.234 Å for core Ce-O, 2.522–2.563 Å and 2.429 Å for the remaining Ce-O),[269-270] suggesting the validity of our fitting model. Figure 6.3c shows

the UV-visible absorption spectrum of TCPP and diffuse reflectance spectrum of Ce-TCPP MOFs. It was found that TCPP exhibits an intense Soret band centered at 415 nm (S_0-S_2 transition) and the relatively weaker Q bands (S_0-S_1 transition) which

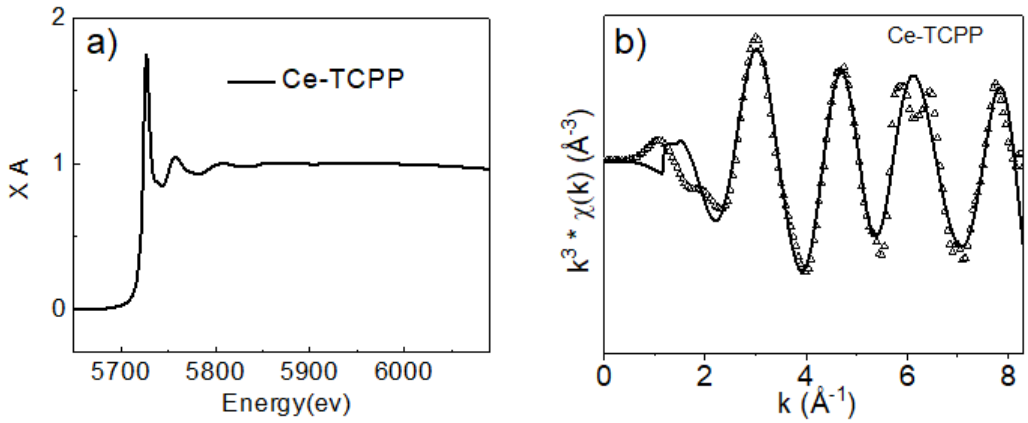

Figure 6.4 Full EXAFS spectra (a) and the Fourier-transformed k-space (b) spectra of Ce-TCPP. The data are shown as open points and FEFF fits as solid lines.

Table 6.1 EXAFS fit results for Ce-TCPP. The corresponding fit figure is shown in Figure S2. Additional parameters: ΔEo = 5.72, $S_0^2 = 1$ (all paths).

Ce-TCPP			
vector	**N**	**R(Å)**	**σ^2x10^{-3}(Å^2)**
Ce-O_1	2	2.203(+/- 0.02)	6.7
Ce-O_2	2	2.430(+/- 0.02)	1
Ce-O_3	2	2.435(+/- 0.02)	2.6
Ce-O_4	2	2.552(+/- 0.02)	1

spread over a wide range in the visible region with four distinct peaks at 512 nm (Q_y), 547nm (Q_y), 588nm (Q_x) and 645nm (Q_x).[271-273] In contrast, Ce-TCPP MOFs show broad absorption extended to ~700 nm due to ligand to metal charge transfer (LMCT) interactions.[274-275] The Soret and Q bands of Ce-TCPP MOFs shows a prominent red-

shift compared to TCPP, which can be attributed to the planarity change caused by deformation of TCPP during incorporation: the non-planarity confirmation of TCPP in

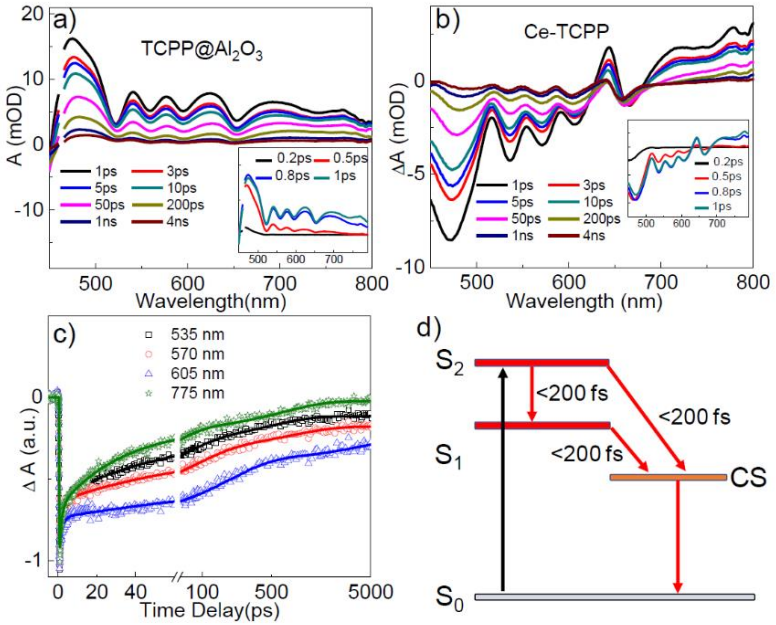

Figure 6.5 Femtosecond OTA spectra of TCPP/Al_2O_3 (a) and Ce-TCPP (b) following 400 nm excitation. The insets show the early time OTA spectra. (c) Q band ground state bleach (GSB) recovery of Ce-TCPP. (d) Enery diagram of Ce-TCPP.

Ce-TCPP MOF destabilizes the porphyrin HOMOs while the LUMOs were not affected significantly.[276-277] Moreover, the strong coupling of the well-arranged TCPP monomers (J-aggregation)[274] may also contribute to the red-shift, which has been observed in other porphyrin- based MOFs reported previously.[262, 278]

Femtosecond optical transient absorption spectroscopy (OTA) was performed with selective excitation of TCPP Soret band to examine the excited state (ES) dynamics of Ce-TCPP MOFs. To better understand the effect of porous nature on ES dynamics in MOFs, we first measured the OTA spectra of TCPP on Al_2O_3 thin film, which represents a control sample for intrinsic ES dynamics of TCPP in heterogeneous

environment. As shown in Figure 6.5a and 6.6a, OTA spectra of TCPP/Al_2O_3 thin film consist of a negative band centered at 415 nm (Figure 6.6a) and a broad positive absorption feature from 450 nm overlapping with several distinct bleach signal at 520 nm, 563 nm, 596 nm and 653 nm (Figure 6.5a). These features have been well studied

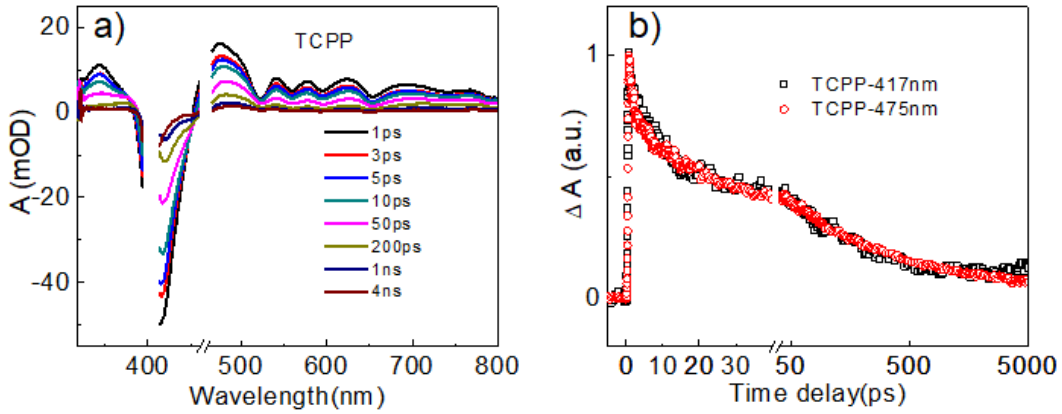

Figure 6.6 (a) Femtosecond OTA spectra of TCPP on Al_2O_3 film. (b) Comparison of ES decay and ground-state bleach recovery of TCPP on Al_2O_3 film. GSB recovery at 417 nm was reversed for better comparison.

and can be attributed to TCPP Soret band ground state bleach (GSB), ES absorption (ESA), and Q band GSB, respectively. The recovery of Soret GSB and the decay of ES follow the same kinetics (Figure 6.6b), together with the presence of the isosbestic point at 451 nm, suggesting that the decay of ES molecules to their GS is the only relaxation process in TCPP/Al2O3 after excitation.

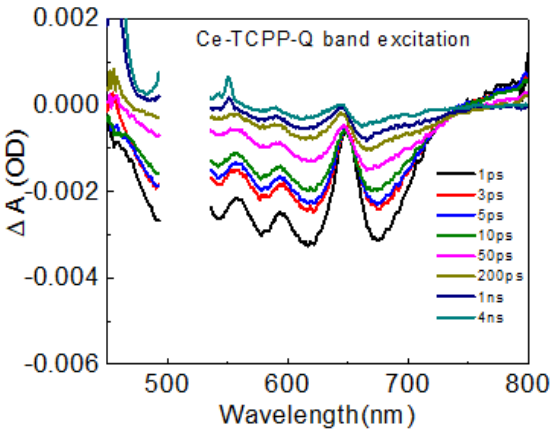

Figure 6.7 Femtosecond OTA spectra of Ce-TCPP with Q band excitation.

Compared to TCPP, the OTA spectra of Ce-TCPP MOFs are dramatically different. As shown in Figure 6.5b, the OTA spectra of Ce-TCPP exhibit the Soret and Q band GSB with a red-shift in the range of 450 nm to 670 nm, which is consistent with its UV-visible ground state diffuse reflectance spectrum. However, the positive features pertaining to ESA are missing in the region < 600 nm even at early times (< 1 ps) (inset of Figure 6.5b). We attribute this difference to the ultrafast (<120 fs) formation of a new charge separated state evolved from singlet excited state (i.e. S_2 & S_1) (Figure 6.5d), as superfast charge separation (CS) was also observed for Q band excitation (Figure 6.7). The CS was further confirmed by the observation of the transient feature at > 700 nm region as the fingerprint absorption of one electron oxidized $TCPP^{*+}$.[279-283] Figure 6.5c compares the kinetic traces of Q band bleach at 535 nm, 570 nm, 605 nm, and 664 nm, where a clear rising component was observed

Table 6.2 Multiexponential fit parameters for TA experiments corresponding to the fits shown in Figure 3c in the main text.

	A_1(%)	τ_1(ps)	A_2(%)	τ_2(ps)	A_3(%)	τ_3(ps)	A_4(%)	τ_4
535nm	-41.1		-32		-14.8		-12	
570nm	-36.4	1.5	-21.2	49.2	-23.3	262	-19.2	>>5ns
605nm	-26.8		-2.74		-38		-32.4	
664nm	-12.5		12.4		-32.7		-42.4	

and can be assigned to the increased population of thermally relaxed Q_x state after excitation or due to the overlap with feature at > 650 nm region. These results, similar to previous reports accounting for electron transfer process in MOFs,[278, 284] implying that fast electron transfer (ET) occurs from TCPP ligand to Ce metal cluster. The kinetic traces of Ce-TCPP can be fitted by a four-exponential function with parameters listed in Table 6.2. Unfortunately, we are not able to accurately determine the lifetime of the CS state due to the long-lived component (>> 5ns) which is beyond our OTA time window. Nevertheless, we can conclude that the presence of long-lived CS state after ET is beneficial for applications in photocatalysis.

The formation of CS is further supported by directly monitoring the electron density changes at Ce center following selective excitation of TCPP ligand using X-ray transient absorption (XTA) spectroscopy. Figure 4a shows the XANES spectrum of Ce-TCPP at Ce L3 edge and the difference spectra obtained by subtracting the ground state (laser-off) spectrum from spectrum collected at different delay times (100 ps, 1n s, 10 ns and 100 ns) following 400 nm laser excitation. The positive feature observed at 5723.7 eV indicates that the edge energy of Ce shifts to lower energy, suggesting the formation of reduced Ce Center in Ce-TCPP MOFs. This is

further supported by the negative feature observed at 5725.5 eV: the decreased number of empty 4f orbitals prohibits the excitation of 2p core electrons, resulting in the decreased absorption intensity. The intensity of this negative feature decreases gradually from 100 ps to 10 ns until 100 ns where no transient signal was observed (Figure 6.8), suggesting that this is a long-lived transient species. These results together confirmed the formation of a long-lived CS state due to LMCT after photoexcitation of Ce-TCPP MOFs, consistent with OTA results above.

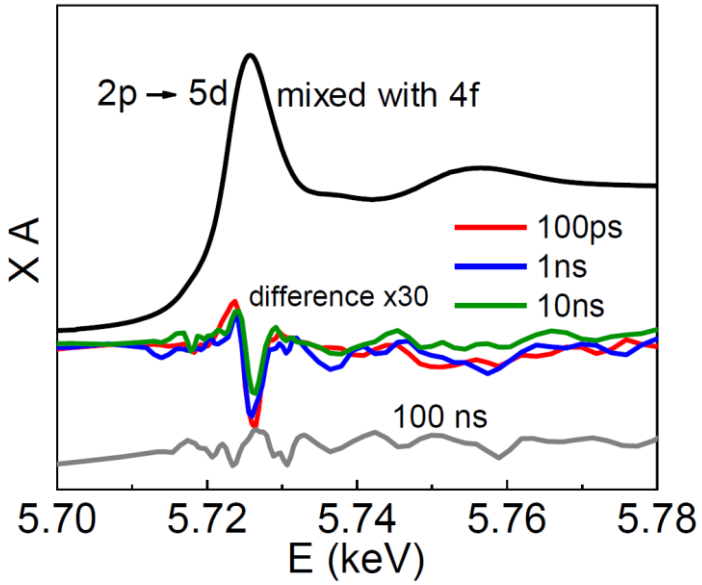

Figure 6.8 XANES spectrum of Ce-TCPP MOFs at Ce L3-edge (black plot) and the difference XANES spectra at 100 ps (red), 1ns (blue), 10ns (green), and 100 ns (gray) obtained by subtracting the laser-off spectrum from laser-on spectrum.

6.3 Conclusion

In summary, we have synthesized Ce-TCPP constructed from free-base TCPP ligand and Cerium ammonium nitrate. The bulk and local structure of Ce-TCPP

MOFs were confirmed by XRD, FTIR, UV-visible spectroscopy, and XAS, where both Ce3+ and Ce4+ coexist in MOF. Using OTA spectroscopy, we show that ultrafast charge transfer occurs from TCPP ligand to Ce center in Ce-TCPP following the excitation of TCPP ligand, forming a long-lived charge separated state. The formation of this charge separated state was further confirmed by XTA, where the reduction of Ce center was observed due to excitation of TCPP ligand. The observed ultrafast charge transfer process which results into the formation of long-lived charge separated state is expected to be beneficial for photocatalysis and thus imply the potential application of Ce-TCPP MOFs in solar energy conversion.

Chapter 7.

2D COVALENT ORGANIC FRAMEWORKS AS INTRINSIC PHOTOCATALYSTS FOR VISIBLE LIGHT-DRIVEN CO_2 REDUCTION

7.1 Introduction

Efficiently capturing CO_2 and simultaneously converting it to chemical fuels driven by solar energy is a promising approach to address energy crisis and climate issues.[285-287] The essential challenge in reaching this elusive goal is to formulate a rationally designed photocatalytic system that can effectively couple a given photosensitizer (PS) with an appropriate molecular catalyst (MC), thereby enabling efficient photosensitization of multi-electron reduction catalysis.[288-290] While many molecular- or semiconductor-based photocatalytic systems have been designed, they all suffer difficulties, such as poor adsorption of CO_2, inappropriate architecture of active sites, wasteful rapid charge recombination or low selectivity etc.[3, 135, 285, 291]

As an emerging class of crystalline porous materials, covalent organic frameworks (COFs) represent a versatile platform offering new promise for photocatalytic CO_2 reduction.[292-302] COFs are built from periodic organic building blocks via covalent bond formation, providing an innovative approach for the construction of robust photocatalytic materials with built-in PS (i.e. extended π-conjugation) and MC (e.g. incorporated via postsynthetic modification), thereby facilitating efficient charge

separation (CS) and precise determination of the nature of the incorporated catalytic active sites. Moreover, these structurally diverse materials, with large surface areas and readily tunable pore sizes are expected to provide an ideal scaffold for CO_2 adsorption, diffusion, and activation. However, this undeniable potential has yet to be realized, with some recently studied initial systems exhibiting moderate efficiencies.[303-306] Given the inherent advantages of COFs as photocatalytic materials and their potential impact on the global energy crisis,[307-311] no time should be wasted in undertaking a well-designed plan to further develop useful devices.

Addressing this pressing need, in this work, we report a newly designed COF photocatalyst with an effective photoactive 2D triazine COF as PS and a precisely incorporated tricarbonylchloro(bipyridyl) Re complex ($Re(bpy)(CO)_3Cl$) as CO_2 reduction MC (denoted Re-COF). We show that this Re-COF hyb rid catalyst can effectively reduce CO_2 to CO with high selectivity (98%) and durability upon visible light illumination. More importantly, the combination of *in situ* and time-resolved optical (TA) and X-ray (XTA) absorption spectroscopic techniques uncovered the active sites and key intermediate species that are responsible for CO_2 reduction.

7.2 Results and discussion

The 2D triazine COF was synthesized from 2,2-bipyridyl-5,5-dialdehyde (BPDA) and 4,4',4''-(1,3,5-triazine-2,4,6-triyl) trianiline (TTA) by solvothermal reactions (Scheme 7.1a). The formation of imine linkages between aldehyde and TTA in COF was confirmed by Fourier transform infrared (FT-IR) spectrum (Figure 7.1a), where

we observed the formation of C=N stretching modes at 1626 cm^{-1} that is characteristic of imine in COF and the vanishing of amino band (3213-3435 cm^{-1}) and aldehyde band (1673-1692 cm^{-1}) that were present in the starting materials, i.e. TTA

Scheme 7.1. a) The synthesis of COF and Re-COF. (b) Side view and (c) unit cell of AA stacking COF. (d) Proposed catalytic mechanism for CO_2 reduction.

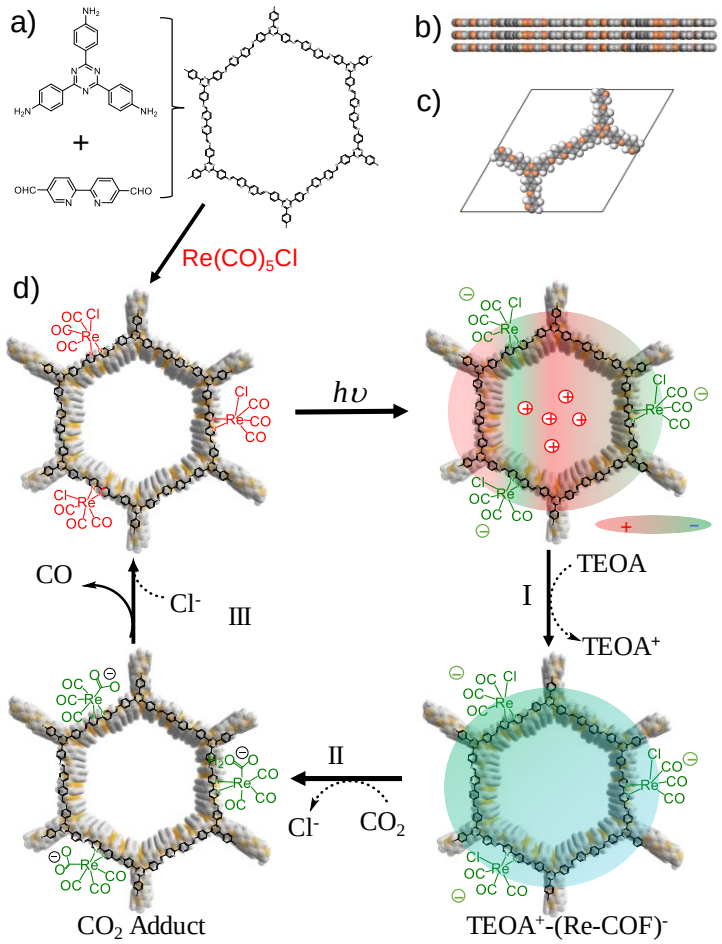

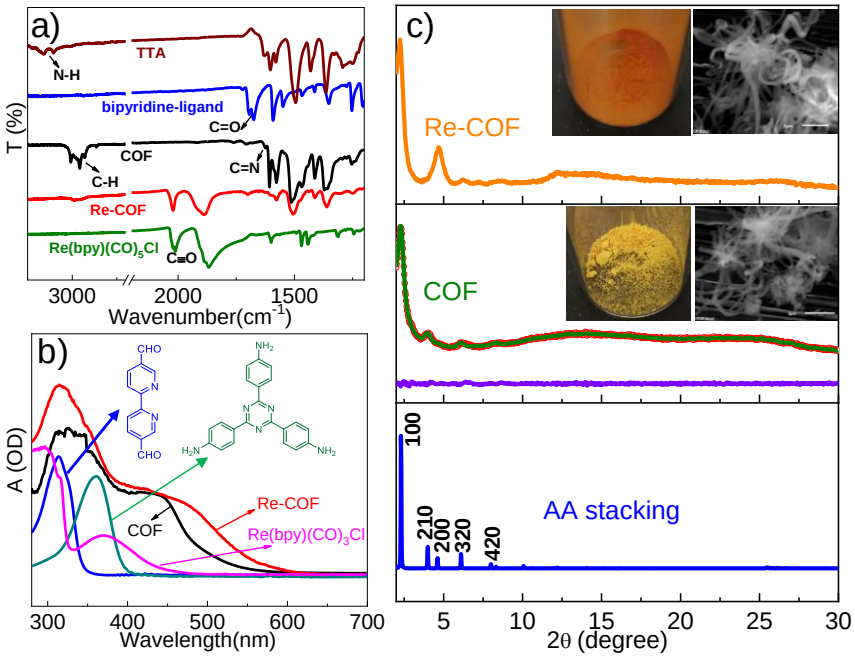

Figure 7.1 FT-IR (a) and diffuse reflectance UV-visible spectra (b) of COF, Re-COF and their starting materials. (c) Powder XRD patterns of Re-COF and COF obtained experimentally (green), through Pawley refinement (red), and via simulation using AA stacking mode (blue). The purple plot in the middle panel is the difference pattern between experimental and simulated data.

and BPDA, respectively.[297-298, 312-314] The formation of the COF macrostructure was further supported by the additional absorption band (~ 440 nm) observed in its diffuse reflectance UV-visible spectrum (Figure 7.1b), which arises from the delocalized intramolecular charge transfer (ICT) band due to π-conjugation of TTA and BPDA.[315-317] Powder XRD patterns of COF show prominent diffraction peaks (Figure 7.1c), indicating its crystalline nature. The lattice model was simulated using Material Studio 8.0,[312] from which we obtained the most probable structure of COF with AA stacking mode (Scheme 1b and 1c). Pawley refinement of the simulated structure yields XRD patterns that agree well with the experimental data, as indicated by the negligible difference between the simulated and experimental data (middle panel of

Figure 7.1c), suggesting the validity of computational model.

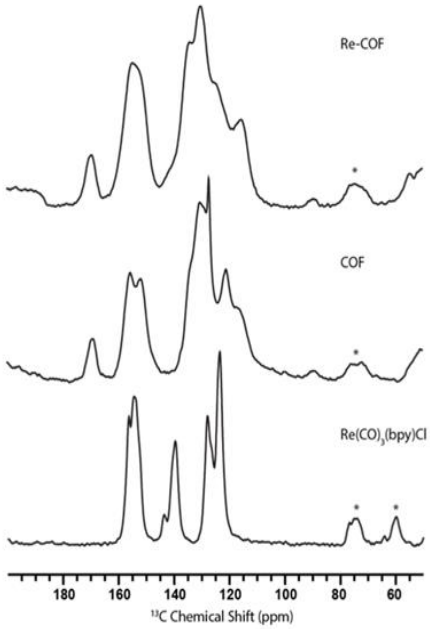

Figure 7.2 ^{13}C NMR spectrum for Re-COF, COF and $Re(CO)_3(bpy)Cl$, signal marked with star are spinning side bands.

Re moiety was then incorporated into the COF via direct reaction between bipyridine ligand and $Re(CO)_5Cl$ to form Re-COF (Scheme 1a).[318] This is confirmed by the additional peaks at 1887 cm^{-1}, 1916 cm^{-1} and 2022 cm^{-1} in FT-IR spectrum of Re-COF, which correspond to -CO vibrational stretching of Re complex (Figure 7.1a).[318-320] The XRD patterns (Figure 7.1c) of Re-COF, match well with the simulated data of COF, indicating the preservation of its crystal parameters after Re incorporation. This is further supported by the ^{13}C NMR spectrum (Figure 7.2) and SEM images (Inset of Figure 7.1c) of Re-COF and COF. In addition, the local coordination structure of Re complex in Re-COF measured using X-ray absorption spectroscopy (XAS) retains that of $Re(bpy)(CO)_3Cl$ (Figure 7.3 and Table 7.1),

suggesting that $Re(bpy)(CO)_3Cl$ are well preserved after being incorporated into the COF framework. However, it is notable that the UV-visible spectrum of Re-COF are extended to broader region (Figure 1b). This can be attributed to either the vibronic broadening of COFs,[321] or the increased delocalization due to the chelation of $Re(bpy)(CO)_3Cl$. The permanent porosity of COF and Re-COF was confirmed by N_2 sorption measurements at 77 K (Figure 7.4).

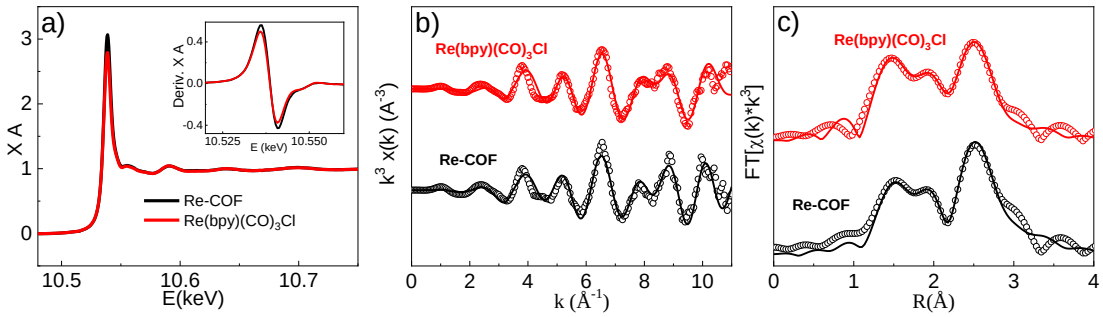

Figure 7.3 The X-ray absorption (XAS) spectra of Re-COF and $Re(bpy)(CO)_3Cl$ complex in energy (a), k-space (b), and R-space at Re L3-edge. The open circles and solid lines in (b) and (c) are experimental and fitted results, respectively.

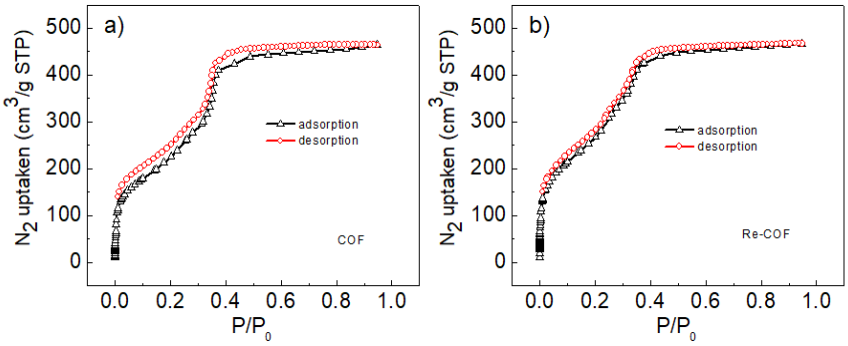

Figure 7.4 N2 adsorption isotherm of (a) COF and (b) Re-COF

Table 7.1 The fitting parameters for steady-state XAS data for Re-COF and $Re(bpy)(CO)_3Cl$ at Re L3-edge.

Re-COF				$Re(bpy)(CO)_3Cl$		
vector	N	R(Å)	$\sigma^2 x\ 10^{-3}(Å^2)$	N	R(Å)	$\sigma^2 x\ 10^{-3}(Å^2)$
Re-C	2, 1	1.86, 2.05	1, 10	2, 1	1.90, 1.98	1, 10
Re-N	2	2.24	1	2	2.18	1
Re-Cl	1	2.42	9.17	1	2.49	5.81

As light absorption and CS are the key initial step to determine whether Re-COF can be used as photocatalyst for CO_2 reduction, we first examined the CS dynamics in Re-COF using TA spectroscopy following 530 nm excitation (where the TA spectra of $Re(bpy)(CO)_3Cl$ show negligible signal). Figure 7.5a shows the TA spectra of COF consisting of a negative band centered at 500 nm and a positive feature centered at 600 nm, which can be assigned to the stimulated emission (SE)[322-323] and ES absorption of ICT,[323-324] respectively. As indicated by the kinetic trace of excited ICT absorption (COF@ICT, Figure 7.5b), the formation of the excited ICT state (fast-rising component) is ultrafast with ~200 fs time constant and the charge recombination (CR) time is 19.4 ps (Table 7.2). Compared to the spectra of COF, the TA spectra of Re-COF show a similar SE band at 500 nm and the formation of the

Table 7.2 The fitting parameters for the kinetic traces at 600 nm for COF and Re-COF

Sample	τ_1,ps (A_1,%)	τ_2,ps (A_2,%)	τ_3,ps (A_3,%)	τ_4,ps (A_4,%)	τ_{ave},ps
COF	0.2[r] (100)	41.1 (36.1)	7.1 (63.9)		19.4
Re-COF	0.2[r] (100)	1.5 (39.9)	12.4 (38.0)	751 (22.1)	171

[r]the rising component in a multi-exponential decay function

excited ICT state (Figure 7.5c). However, its excited ICT band is much broader than

that in COF with additional absorption beyond 650 nm, which can be attributed to its broader ground state (GS) spectrum. More interestingly, this excited ICT state of Re-COF (Re-COF@ICT, Figure 7.5b) exhibits much longer lifetime (τ = 171 ps) than that of COF, suggesting that the incorporation of $Re(bpy)(CO)_3Cl$ inhibits CR in Re-COF.

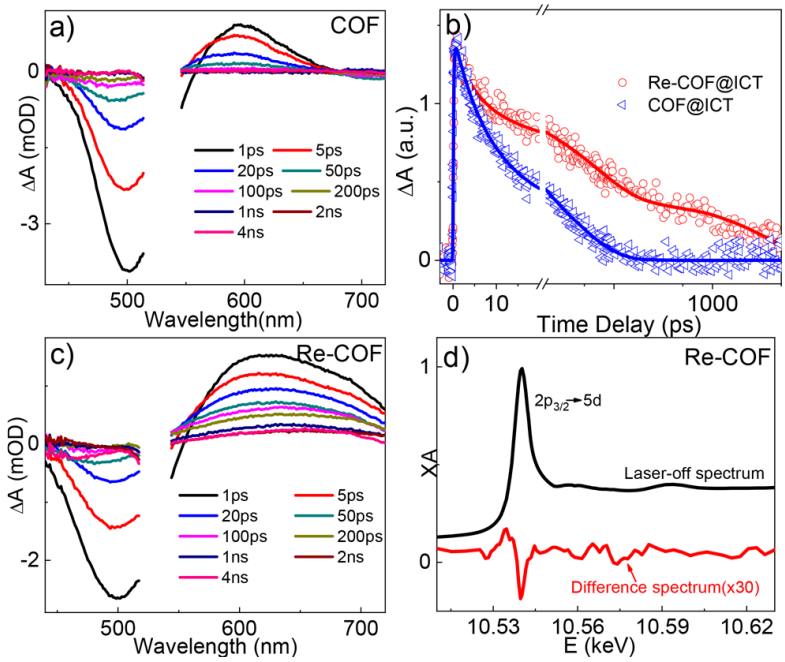

Figure 7.5 Transient optical spectra of COF (a) and Re-COF (c) following 530 nm excitation. (b) The comparison of kinetics for ICT of COF and Re-COF. (d) The XANES spectrum of Re-COF at Re L_3-edge. The bottom panel is the difference spectrum after subtracting the laser-off spectrum from laser-on spectrum collected at 150 ps delay time.

To gain insight on the role of $Re(bpy)(CO)_3Cl$ play in elongating the excited ICT lifetime, we directly examined the electron density at the Re center in Re-COF following the excitation of COF using element specific XTA spectroscopy. Figure

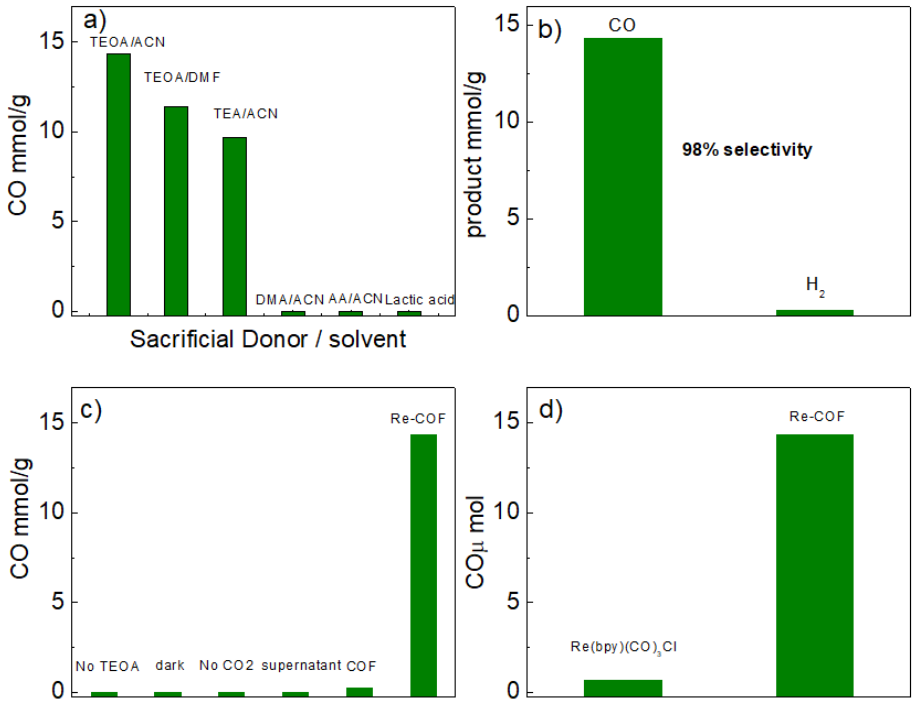

Figure 7.6 Optimization of light-driven CO_2 reduction reaction. (a) The amount of CO produced using different solvents and sacrificial donors. (b) The selectivity of Re-COF for CO_2 reduction. (c) The amount of CO generated under the conditions without TEOA, in the dark, without CO_2, supernatant after catalysis, and replacing Re-COF by COF. (d) The comparison of the amount of CO generated between Re-COF and homogeneous $Re(bpy)(CO)_3Cl$ with $2.7x10^{-7}$ mol of Re complex in both samples.

7.5d shows the X-ray absorption near edge structure (XANES) spectrum of Re-COF collected at Re L_3-edge, which is featured by a prominent white line transition corresponding to dipole allowed $2p_{3/2}$-$5d$ transition.[325-326] Also shown in Figure 7.5d is the transient XANES spectrum of Re-COF, i.e. the difference spectrum obtained by subtracting the GS spectrum from the spectrum collected at 150 ps. The distinct positive signal observed at 10.531 keV directly supports that Re edge shifts to lower energy, suggesting that photoexcitation of Re-COF leads to the reduction of Re center in Re-COF. This is further supported by the negative feature observed at 10.538 keV:

the reduction of Re decreased the number of empty d orbitals, prohibiting $2p_{3/2}$ -5*d*

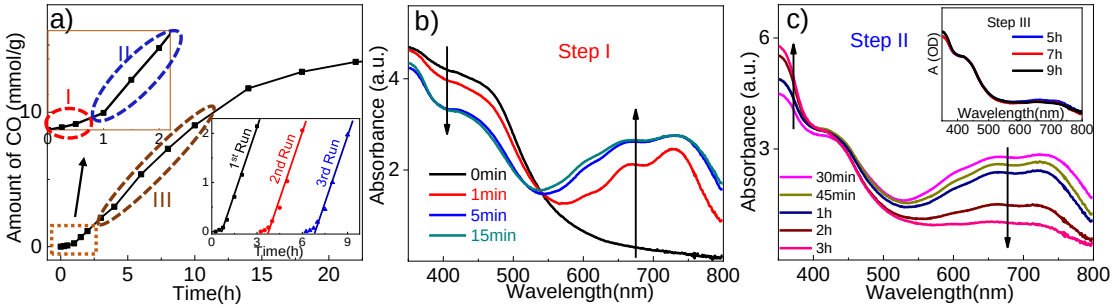

Figure 7.7 (a) Amount of CO produced as a function of time. The top left inset shows the zoomed in profile in the first 2 hours' reaction, and the lower right inset shows the recyclability of the system after three 3-hour experiments. The *in situ* diffuse reflectance UV-visible spectra of Re-COF under standard photocatalytic conditions within 15 min (b) and 3 h (c). The inset of c shows the *in-situ* spectra collected from 5 h to 9 h.

transition and thus decreasing its absorption intensity. These results, together with elongated ICT lifetime observed in TA studies, suggest that the electrons in the excited ICT state of Re-COF are partially located in $Re(bpy)(CO)_3Cl$, i.e., electron transfer (ET) indeed occurs from COF to Re complex, which well explains the retarded CR process in Re-COF.

The demonstration of ET from COFs to $Re(bpy)(CO)_3Cl$ suggests the feasibility of using Re-COF as photocatalytic systems for solar fuel conversion. Accordingly, we proceeded to examine its photocatalytic activity for CO_2 reduction usder Xe lamp (cut-off wavelength = 420 nm) illumination. Under the optimized conditions (Figure 7.6), The system can generate ~15 mmol CO/g of Re-COF steadily for >20 h after ~ 15 min induction period, accounting for a TON of 48 (Figure 7.7a) and 22 times better

than its homogeneous counterpart (Figure 7.6). Since no products have been detected in the liquid phase and only 2% H_2 was produced in the gas phase (Figure 7.6), this system has high selectivity for CO_2 reduction to generate CO (98%). Isotopic experiment using $^{13}CO_2$ was performed under the same catalytic conditions, and the produced ^{13}CO (m/z = 29) shown by gas chromatography mass spectrometry (Figure 7.8) confirms that the generated CO comes from CO_2. The recycling experiments after every three hours of reaction show that the catalytic activity persists for at least 3 cycles (lower right inset of Figure 7.7a).

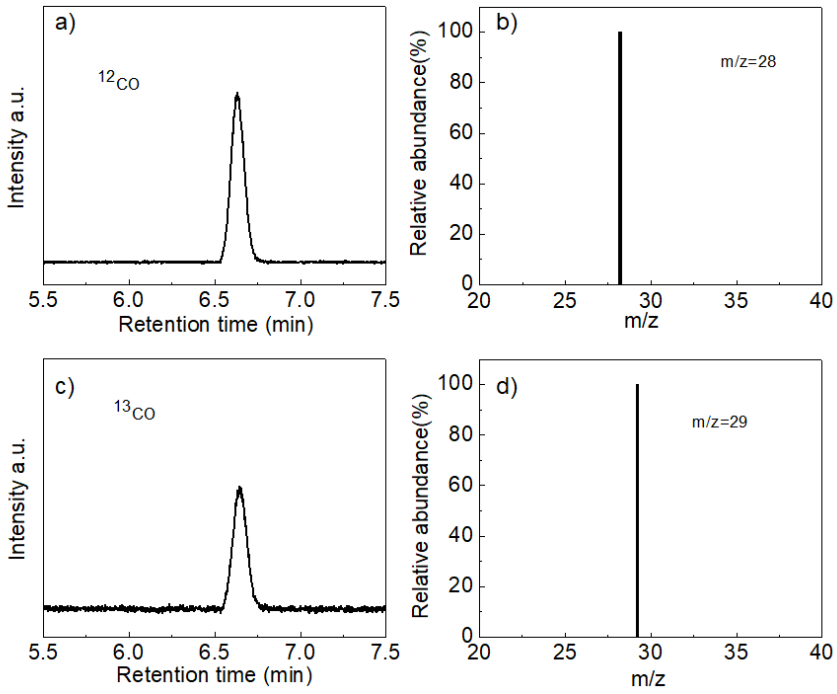

Figure 7.8 GCMS chromatograms and mass analysis of CO obtained from the photocatalytic CO2 reduction reaction under (a) ^{12}CO2 and (b) ^{13}CO2 atmosphere after 4 h photoirradiation using Xe lamp. (c) *m/z* 28 is assigned to ^{12}CO. (d) *m/z* 29 is assigned to ^{13}CO.

To gain more mechanistic insight, we collected the *in situ* diffuse reflectance UV-

visible spectra of the catalytic system under the standard catalytic conditions. As shown in Figure 7.7b, immediately following illumination, prominent new absorption in the 550-800 nm region that resembles the broad absorption of the ICT band in TA was observed and can thus be attributed to the formation of the excited ICT state. The intensity of this ICT band increases in the first 15 mins, accompanied by the depletion of absorption at 400-500 nm with an isosbestic point at 539 nm, suggesting that such spectral evolution corresponds to the same process. While similar spectral evolution was observed in the system without CO_2, significantly less evolution was observed in the absence of TEOA (Figure 7.9), which suggests that reduction quenching of Re-COF by TEOA with the formation of a formal $TEOA^+$-$(COF\text{-}Re)^-$ CS state contributes to the evolution. The time window for this spectral evolution agrees well with the induction period observed in catalytic reaction and can thus be attributed to the accumulation of $TEOA^+$-$(COF\text{-}Re)^-$ CS state before catalysis initiates (Step I in Figure 7.7a).

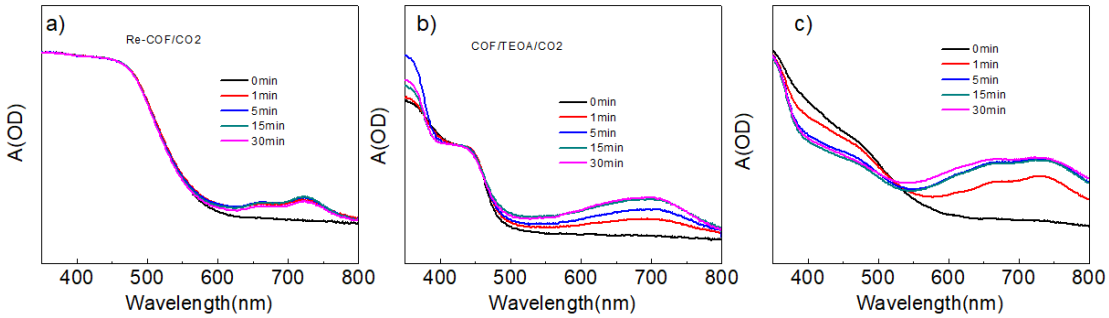

Figure 7.9 The in situ diffuse reflectance UV-visible spectra of control systems within 30 min (step I). (a) Re-COF/CO_2, (b) COF/TEOA/CO_2, (c) Re-COF/TEOA/N_2.

After the induction period, the broad absorption at 550-800 nm decreases

significantly within 3 h while the feature at < 430 nm grows and a new isosbestic point is observed at 430 nm (Step II, Figure 7.7c), which results in a distinct spectral feature from that of Step I and suggests the formation of a new intermediate species. Note that negligible or very slight evolution corresponding to Step II was observed in the system without CO_2 or by replacing Re-COF by COF (Figure 7.10), suggesting that the intermediate species formed during Step II is associated with CO_2 and Re-moiety. After Step II, the evolution of the spectra stops (Step III, inset of Figure 7.7c), which is consistent with the time window for steady generation of CO, suggesting that the system reaches an equilibrium state.

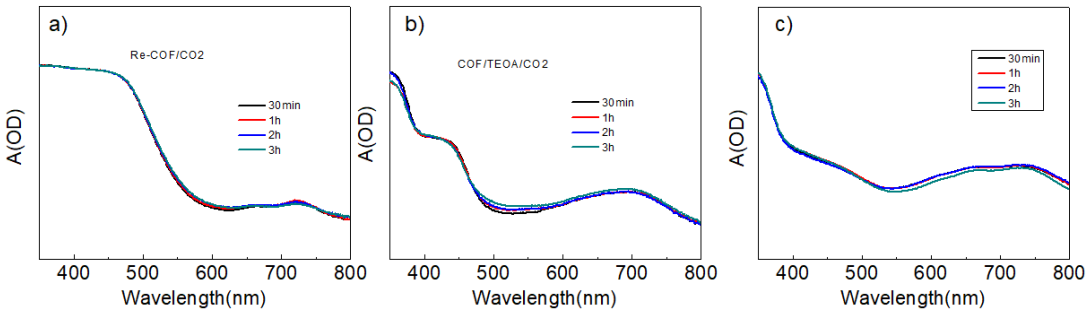

Figure 7.10 The in situ diffuse reflectance UV-visible spectra of control systems from 30 min. to 3 h (step II). (a) Re-COF/CO_2, (b) COF/TEOA/CO_2, (c) Re-COF/TEOA/N_2.

Taking together, these spectroscopic results point to a mechanistic pathway proposed in Scheme 7.1d. Upon illumination, the catalytic cycle initiates with the formation of ICT state which is quickly reduced by TEOA, forming a $TEOA^+$-(COF-Re)$^-$ CS state (Step I). This formal CS state with reduced Re-COF is then able to capture CO_2 to form the next intermediate species (Step II). According to previous literature,[290, 318-320, 327-328] this intermediate species is likely the CO_2 adducts such as

$TEOA^+$-(COF-Re[CO_2])$^-$ or/and $TEOA^+$-(COF-Re[CO_2H])$^-$, which is formed after the dissociation of Cl^- from Re-moiety. As the spectra persist during steady state generation of CO (Step III), the consumption of the CO_2 adducts to eventually form CO represents the rate limiting step of the catalytic reaction, although multiple processes might be involved before CO is released.[34-36, 43-44]

7.3 Conclusion and future work

In conclusion, we report a newly designed COF hybrid catalyst by incorporating Re(bpy)$(CO)_3$Cl into the framework of 2D triazine COF via post-synthetic modification. We show that this system can efficiently reduce CO_2 with better activity than its homogenous counterpart and high selectivity and stability. Using TA and XTA spectroscopy, we show that this system can undergo facile ICT through ET from photoexcited COF to Re moiety. Using *in situ* diffuse reflectance UV-visible spectroscopy, we unraveled three key intermediate species that are responsible for CS, induction period, and rate limiting step in CO_2 reduction. These results not only demonstrated the great potential of COFs as effective solar fuel photocatalysts but also provided unprecedented new insight into the catalytic mechanism for CO_2 reduction.

Inspired by this study, the future work should focus on investigating the light harvesting and excited state dynamics of COFs, which is one of the key properties that dictate the function of COFs for photocatalysis. We synthesized highly emissive C-sp2 COFs based on star shaped donor-accepter pairs. The understanding of

fundamental photophysical events in such COFs by using transient absorption spectroscopy and TCSPC will provide guidance in material design, which facilitate solar to fuel application of COFs.

REFERENCES

1. Iea, I., Key World Energy Statistics 2014. **2014**, 1-82.

2. Yu, Z.; Li, F.; Sun, L., Recent Advances in Dye-sensitized Photoelectrochemical Cells for Solar Hydrogen Production Based on Molecular Components. *Energy Environ. Sci.* **2015,** *8* (3), 760-775.

3. White, J. L.; Baruch, M. F.; Pander, J. E.; Hu, Y.; Fortmeyer, I. C.; Park, J. E.; Zhang, T.; Liao, K.; Gu, J.; Yan, Y.; Shaw, T. W.; Abelev, E.; Bocarsly, A. B., Light-Driven Heterogeneous Reduction of Carbon Dioxide: Photocatalysts and Photoelectrodes. *Chem. Rev.* **2015,** *115* (23), 12888-12935.

4. McConnell, I.; Li, G. H.; Brudvig, G. W., Energy Conversion in Natural and Artificial Photosynthesis. *Chem. Biol.* **2010,** *17* (5), 434-447.

5. Hagfeldt, A.; Boschloo, G.; Sun, L. C.; Kloo, L.; Pettersson, H., Dye-Sensitized Solar Cells. *Chem. Rev.* **2010,** *110* (11), 6595-6663.

6. Purchase, R. L.; de Groot, H. J. M., Biosolar cells: global artificial photosynthesis needs responsive matrices with quantum coherent kinetic control for high yield. *Interface Focus* **2015,** *5* (3), 16.

7. Siegbahn, P. E. M., Structures and Energetics for O2 Formation in Photosystem II. *Acc. Chem. Res.* **2009,** *42* (12), 1871-1880.

8. Fleming, G. R.; Schlau-Cohen, G. S.; Amarnath, K.; Zaks, J., Design principles of photosynthetic light-harvesting. *Faraday Discuss.* **2012,** *155* (0), 27-41.

9. Herek, J. L.; Wohlleben, W.; Cogdell, R. J.; Zeidler, D.; Motzkus, M., Quantum control of energy flow in light harvesting. *Nature* **2002,** *417* (6888), 533-535.

10. Tachibana, Y.; Vayssieres, L.; Durrant, J. R., Artificial photosynthesis for solar water-splitting. *Nat. Photonics* **2012,** *6* (8), 511-518.

11. Abramavicius, D.; Valkunas, L., Artificial Photosynthesis: Theoretical Background In *Artificial Photosynthesis*, Bruno, R., Ed. Academic Press Ltd-Elsevier Science Ltd: London, 2016; Vol. 79, pp 129-167.

12. Eckenhoff, W. T.; Eisenberg, R., Molecular systems for light driven hydrogen production. *Dalton Trans.* **2012,** *41* (42), 13004-13021.

13. Thoi, V. S.; Sun, Y.; Long, J. R.; Chang, C. J., Complexes of earth-abundant metals for catalytic electrochemical hydrogen generation under aqueous conditions. *Chem. Soc. Rev.* **2013,** *42* (6), 2388-2400.

14. Costentin, C.; Robert, M.; Savéant, J.-M., Catalysis of the electrochemical reduction of carbon dioxide. *Chem. Soc. Rev.* **2013,** *42* (6), 2423-2436.

15. Fujishima, A.; Honda, K., ELECTROCHEMICAL PHOTOLYSIS OF WATER AT A SEMICONDUCTOR ELECTRODE. *Nature* **1972,** *238* (5358), 37-+.

16. Gloaguen, F.; Lawrence, J. D.; Rauchfuss, T. B., Biomimetic Hydrogen Evolution Catalyzed by an Iron Carbonyl Thiolate. *J. Am. Chem. Soc.* **2001,** *123* (38), 9476-9477.

17. Fillol, J. L.; Codolà, Z.; Garcia-Bosch, I.; Gómez, L.; Pla, J. J.; Costas, M., Efficient water oxidation catalysts based on readily available iron coordination complexes. *Nat. Chem.* **2011,** *3* (10), 807-813.

18. Costentin, C.; Drouet, S.; Robert, M.; Savéant, J.-M., A Local Proton Source Enhances CO_2 Electroreduction to CO by a Molecular Fe Catalyst *Science* **2012,** *338* (6103), 90.

19. Kadowaki, H.; Saito, N.; Nishiyama, H.; Kobayashi, H.; Shimodaira, Y.; Inoue, Y., Overall splitting of water by RuO2-loaded PbWO4 photocatalyst with d(10)s(2)-d(0) configuration. *J. Phys. Chem. C* **2007,** *111* (1), 439-444.

20. Kato, H.; Kudo, A., Water splitting into H_2 and O2 on alkali tantalate photocatalysts ATaO(3) (A = Li, Na, and K). *J. Phys. Chem. B* **2001,** *105* (19), 4285-4292.

21. Kapoor, M. P.; Inagaki, S.; Yoshida, H., Novel Zirconium-titanium Phosphates Mesoporous Materials for Hydrogen Production by Photoinduced Water Splitting. *J. Phys. Chem. B* **2005,** *109* (19), 9231-9238.

22. Kudo, A.; Domen, K.; Maruya, K.; Onishi, T., Photocatalytic Activities of TiO_2 Loaded With NiO. *Chem. Phys. Lett.* **1987,** *133* (6), 517-519.

23. Zhang, B.; Sun, L., Artificial Photosynthesis: Opportunities and Challenges of Molecular Catalysts. *Chem. Soc. Rev.* **2019,** *48* (7), 2216-2264.

24. Zhang, Q.; Shreeve, J. n. M., Metal–Organic Frameworks as High Explosives: A New Concept for Energetic Materials. *Angew. Chem. Int. Ed.* **2014,** *53* (10), 2540-2542.

25. Furukawa, H.; Cordova, K. E.; O'Keeffe, M.; Yaghi, O. M., The Chemistry and Applications of Metal-Organic Frameworks. *Science* **2013,** *341* (6149), 1230444.

26. Zhou, H.-C.; Long, J. R.; Yaghi, O. M., Introduction to Metal–Organic Frameworks. *Chem. Rev.* **2012,** *112* (2), 673-674.

27. Yaghi, O. M.; O'Keeffe, M.; Ockwig, N. W.; Chae, H. K.; Eddaoudi, M.; Kim, J., Reticular Synthesis and The Design of New Materials. *Nature* **2003,** *423* (6941), 705-714.

28. Ferey, G., Hybrid porous solids: past, present, future. *Chem. Soc. Rev.* **2008,** *37* (1), 191-214.

29. Ferey, G.; Serre, C.; Devic, T.; Maurin, G.; Jobic, H.; Llewellyn, P. L.; De Weireld, G.; Vimont, A.; Daturi, M.; Chang, J. S., Why hybrid porous solids capture greenhouse gases? *Chem. Soc. Rev.* **2011,** *40* (2), 550-562.

30. Kreno, L. E.; Leong, K.; Farha, O. K.; Allendorf, M.; Van Duyne, R. P.; Hupp, J. T., Metal-Organic Framework Materials as Chemical Sensors. *Chem. Rev.* **2012,** *112* (2), 1105-1125.

31. Li, J. R.; Kuppler, R. J.; Zhou, H. C., Selective gas adsorption and separation in metal-organic frameworks. *Chem. Soc. Rev.* **2009,** *38* (5), 1477-1504.

32. Yuan, Y. P.; Yin, L. S.; Cao, S. W.; Xu, G. S.; Li, C. H.; Xue, C., Improving photocatalytic hydrogen production of metal-organic framework UiO-66 octahedrons by dye-sensitization. *Appl. Catal. B-Environ.* **2015,** *168*, 572-576.

33. Wang, D. K.; Huang, R. K.; Liu, W. J.; Sun, D. R.; Li, Z. H., Fe-Based MOFs for Photocatalytic CO2 Reduction: Role of Coordination Unsaturated Sites and Dual Excitation Pathways. *ACS Catal.* **2014,** *4* (12), 4254-4260.

34. Chaemchuen, S.; Kabir, N. A.; Zhou, K.; Verpoort, F., Metal–organic Frameworks For Upgrading Biogas via CO_2 Adsorption to Biogas Green Energy. *Chem. Soc. Rev.* **2013,** *42* (24), 9304-9332.

35. Dolgopolova, E. A.; Rice, A. M.; Martin, C. R.; Shustova, N. B., Photochemistry and Photophysics of MOFs: Steps Towards MOF-based Sensing Enhancements. *Chem. Soc. Rev.* **2018,** *47* (13), 4710-4728.

36. Dhakshinamoorthy, A.; Asiri, A. M.; García, H., Metal–Organic Framework (MOF) Compounds: Photocatalysts for Redox Reactions and Solar Fuel Production. *Angew. Chem. Int. Ed.* **2016,** *55* (18), 5414-5445.

37. Meyer, K.; Ranocchiari, M.; van Bokhoven, J. A., Metal Organic Frameworks for Photo-catalytic Water Splitting. *Energy Environ. Sci.* **2015,** *8* (7), 1923-1937.

38. Sun, D. R.; Liu, W. J.; Qiu, M.; Zhang, Y. F.; Li, Z. H., Introduction of a Mediator For Enhancing Photocatalytic Performance via Post-synthetic Metal Exchange in Metal-Organic Frameworks (MOFs). *Chem. Commun.* **2015,** *51* (11), 2056-2059.

39. Xiao, J.-D.; Shang, Q.; Xiong, Y.; Zhang, Q.; Luo, Y.; Yu, S.-H.; Jiang, H.-L., Boosting Photocatalytic Hydrogen Production of a Metal–Organic Framework Decorated with Platinum Nanoparticles: The Platinum Location Matters. *Angew. Chem. Int. Ed.* **2016,** *128* (32), 9535-9539.

40. Lee, C. Y.; Farha, O. K.; Hong, B. J.; Sarjeant, A. A.; Nguyen, S. T.; Hupp, J. T., Light-Harvesting Metal–Organic Frameworks (MOFs): Efficient Strut-to-Strut Energy Transfer in Bodipy and Porphyrin-Based MOFs. *J. Am. Chem. Soc.* **2011,** *133* (40), 15858-15861.

41. Li, Y.; Zhang, S. S.; Song, D. T., A Luminescent Metal-Organic Framework as a Turn-On Sensor for DMF Vapor. *Angew. Chem. Int. Ed.* **2013,** *52* (2), 710-713.

42. Lin, X. M.; Gao, G. M.; Zheng, L. Y.; Chi, Y. W.; Chen, G. N., Encapsulation of Strongly Fluorescent Carbon Quantum Dots in Metal- Organic Frameworks for Enhancing Chemical Sensing. *Anal. Chem.* **2014,** *86* (2), 1223-1228.

43. Buso, D.; Jasieniak, J.; Lay, M. D. H.; Schiavuta, P.; Scopece, P.; Laird, J.; Amenitsch, H.; Hill, A. J.; Falcaro, P., Highly Luminescent Metal-Organic Frameworks Through Quantum Dot Doping. *Small* **2012,** *8* (1), 80-88.

44. Lu, G.; Li, S. Z.; Guo, Z.; Farha, O. K.; Hauser, B. G.; Qi, X. Y.; Wang, Y.; Wang, X.; Han, S. Y.; Liu, X. G.; DuChene, J. S.; Zhang, H.; Zhang, Q. C.; Chen, X. D.; Ma, J.; Loo, S. C. J.; Wei, W. D.; Yang, Y. H.; Hupp, J. T.; Huo, F. W., Imparting functionality to a metal-organic framework material by controlled nanoparticle encapsulation. *Nat. Chem.* **2012,** *4* (4), 310-316.

45. Jin, S. Y.; Son, H. J.; Farha, O. K.; Wiederrecht, G. P.; Hupp, J. T., Energy Transfer from Quantum Dots to Metal-Organic Frameworks for Enhanced Light Harvesting. *J. Am. Chem. Soc.* **2013,** *135* (3), 955-958.

46. Zhang, Y. M.; Lan, D.; Wang, Y. R.; Cao, H.; Jiang, H., MOF-5 decorated hierarchical ZnO nanorod arrays and its photoluminescence. *Physica E* **2011,** *43* (6), 1219-1223.

47. Liu, J.; Chen, L.; Cui, H.; Zhang, J.; Zhang, L.; Su, C.-Y., Applications of metal–organic frameworks in heterogeneous supramolecular catalysis. *Chem. Soc. Rev.*

2014, *43* (16), 6011-6061.

48. Henschel, A.; Gedrich, K.; Kraehnert, R.; Kaskel, S., Catalytic properties of MIL-101. *Chem. Commun.* **2008,** (35), 4192-4194.

49. Gandara, F.; Puebla, E. G.; Iglesias, M.; Proserpio, D. M.; Snejko, N.; Monge, M. A., Controlling the Structure of Arenedisulfonates toward Catalytically Active Materials. *Chem. Mater.* **2009,** *21* (4), 655-661.

50. Ravon, U.; Domine, M. E.; Gaudillere, C.; Desmartin-Chomel, A.; Farrusseng, D., MOFs as acid catalysts with shape selectivity properties. *New J. Chem.* **2008,** *32* (6), 937-940.

51. Wang, D. K.; Li, Z. H., Bi-functional NH2-MIL-101(Fe) for one-pot tandem photo-oxidation/Knoevenagel condensation between aromatic alcohols and active methylene compounds. *Catal. Sci.* **2015,** *5* (3), 1623-1628.

52. Chen, L. Y.; Peng, Y.; Wang, H.; Gua, Z. Z.; Duana, C. Y., Synthesis of Au@ZIF-8 Single- or Multi-Core-Shell Structures For Photocatalysis. *Chem. Commun.* **2014,** *50* (63), 8651-8654.

53. An, Y.; Liu, Y.; An, P.; Dong, J.; Xu, B.; Dai, Y.; Qin, X.; Zhang, X.; Whangbo, M.-H.; Huang, B., NiII Coordination to an Al-Based Metal–Organic Framework Made from 2-Aminoterephthalate for Photocatalytic Overall Water Splitting. *Angew. Chem. Int. Ed.* **2017,** *56* (11), 3036-3040.

54. Wang, C.; deKrafft, K. E.; Lin, W. B., Pt Nanoparticles@Photoactive Metal-Organic Frameworks: Efficient Hydrogen Evolution via Synergistic Photoexcitation and Electron Injection. *J. Am. Chem. Soc.* **2012,** *134* (17), 7211-7214.

55. Zhou, T. H.; Du, Y. H.; Borgna, A.; Hong, J. D.; Wang, Y. B.; Han, J. Y.; Zhang, W.; Xu, R., Postc-synthesis Modification of a Metalc-Organic Framework to Construct a Bifunctional Photocatalyst for Hydrogen Production. *Energy Environ. Sci.* **2013,** *6* (11), 3229-3234.

56. Silva, C. G.; Luz, I.; Xamena, F.; Corma, A.; Garcia, H., Water Stable Zr-Benzenedicarboxylate Metal-Organic Frameworks as Photocatalysts for Hydrogen Generation. *Chem.: Eur. J* **2010,** *16* (36), 11133-11138.

57. He, J.; Wang, J. Q.; Chen, Y. J.; Zhang, J. P.; Duan, D. L.; Wang, Y.; Yan, Z. Y., A Dye-sensitized Pt@UiO-66(Zr) Metal-Organic Framework For Visible-light Photocatalytic Hydrogen Production. *Chem. Commun.* **2014,** *50* (53), 7063-7066.

58. Toyao, T.; Saito, M.; Dohshi, S.; Mochizuki, K.; Iwata, M.; Higashimura, H.;

Horiuchi, Y.; Matsuoka, M., Development of a Ru Complex-incorporated MOF Photocatalyst for Hydrogen Production Under Visible-light Irradiation. *Chem. Commun.* **2014,** *50* (51), 6779-6781.

59. deKrafft, K. E.; Wang, C.; Lin, W. B., Metal-Organic Framework Templated Synthesis of Fe2O3/TiO2 Nanocomposite for Hydrogen Production. *Adv. Mater.* **2012,** *24* (15), 2014-2018.

60. Nasalevich, M. A.; Becker, R.; Ramos-Fernandez, E. V.; Castellanos, S.; Veber, S. L.; Fedin, M. V.; Kapteijn, F.; Reek, J. N. H.; van der Vlugt, J. I.; Gascon, J., Co@NH2-MIL-125(Ti): Cobaloxime-derived Metal-organic Framework-Based Composite For Light-driven H_2 Production. *Energy Environ. Sci.* **2015,** *8* (1), 364-375.

61. He, J.; Yan, Z.; Wang, J.; Xie, J.; Jiang, L.; Shi, Y.; Yuan, F.; Yu, F.; Sun, Y., Significantly Enhanced Photocatalytic Hydrogen Evolution Under Visible Light Over CdS Embedded on Metal–Organic Frameworks. *Chem. Commun.* **2013,** *49* (60), 6761-6763.

62. Wen, M.; Cui, Y.; Kuwahara, Y.; Mori, K.; Yamashita, H., Non-Noble-Metal Nanoparticle Supported on Metal–Organic Framework as an Efficient and Durable Catalyst for Promoting H2 Production from Ammonia Borane under Visible Light Irradiation. *ACS Appl. Mater. Interfaces* **2016,** *8* (33), 21278-21284.

63. Pullen, S.; Fei, H.; Orthaber, A.; Cohen, S. M.; Ott, S., Enhanced Photochemical Hydrogen Production by a Molecular Diiron Catalyst Incorporated into a Metal–Organic Framework. *J. Am. Chem. Soc.* **2013,** *135* (45), 16997-17003.

64. Fu, Y. H.; Sun, D. R.; Chen, Y. J.; Huang, R. K.; Ding, Z. X.; Fu, X. Z.; Li, Z. H., An Amine-Functionalized Titanium Metal-Organic Framework Photocatalyst with Visible-Light-Induced Activity for CO_2 Reduction. *Angew. Chem. Int. Ed.* **2012,** *51* (14), 3364-3367.

65. Sun, D. R.; Fu, Y. H.; Liu, W. J.; Ye, L.; Wang, D. K.; Yang, L.; Fu, X. Z.; Li, Z. H., Studies on Photocatalytic CO2 Reduction over NH2-Uio-66(Zr) and Its Derivatives: Towards a Better Understanding of Photocatalysis on Metal-Organic Frameworks. *Chem.: Eur. J* **2013,** *19* (42), 14279-14285.

66. Sun, D. R.; Gao, Y. H.; Fu, J. L.; Zeng, X. C.; Chen, Z. N.; Li, Z. H., Construction of a supported Ru complex on bifunctional MOF-253 for photocatalytic CO2 reduction under visible light. *Chem. Commun.* **2015,** *51* (13), 2645-2648.

67. Chambers, M. B.; Wang, X.; Elgrishi, N.; Hendon, C. H.; Walsh, A.; Bonnefoy, J.; Canivet, J.; Quadrelli, E. A.; Farrusseng, D.; Mellot-Draznieks, C.; Fontecave, M.,

Photocatalytic Carbon Dioxide Reduction with Rhodium-based Catalysts in Solution and Heterogenized within Metal-Organic Frameworks. *ChemSusChem* **2015,** *8* (4), 603-608.

68. Wang, S. B.; Wang, X. C., Photocatalytic CO2 reduction by CdS promoted with a zeolitic imidazolate framework. *Appl. Catal. B-Environ.* **2015,** *162*, 494-500.

69. Liu, Q.; Low, Z. X.; Li, L. X.; Razmjou, A.; Wang, K.; Yao, J. F.; Wang, H. T., ZIF-8/Zn2GeO4 nanorods with an enhanced CO2 adsorption property in an aqueous medium for photocatalytic synthesis of liquid fuel. *J. Mater. Chem. A* **2013,** *1* (38), 11563-11569.

70. Kajiwara, T.; Fujii, M.; Tsujimoto, M.; Kobayashi, K.; Higuchi, M.; Tanaka, K.; Kitagawa, S., Photochemical Reduction of Low Concentrations of CO2 in a Porous Coordination Polymer with a Ruthenium(II)–CO Complex. *Angew. Chem. Int. Ed.* **2016,** *55* (8), 2697-2700.

71. Wilson, R., Euler's gem: the polyhedron formula and the birth of topology. *BSHM Bull.* **2009,** *24* (3), 196-198.

72. Huang, N.; Wang, P.; Jiang, D., Covalent organic frameworks: a materials platform for structural and functional designs. *Nat Rev Mater* **2016,** *1* (10), 16068.

73. Tilford, R. W.; Gemmill, W. R.; zur Loye, H.-C.; Lavigne, J. J., Facile Synthesis of a Highly Crystalline, Covalently Linked Porous Boronate Network. *Chem. Mater.* **2006,** *18* (22), 5296-5301.

74. Côté, A. P.; El-Kaderi, H. M.; Furukawa, H.; Hunt, J. R.; Yaghi, O. M., Reticular Synthesis of Microporous and Mesoporous 2D Covalent Organic Frameworks. *J. Am. Chem. Soc.* **2007,** *129* (43), 12914-12915.

75. Xie, Y.-F.; Ding, S.-Y.; Liu, J.-M.; Wang, W.; Zheng, Q.-Y., Triazatruxene based covalent organic framework and its quick-response fluorescence-on nature towards electron rich arenes. *J. Mater. Chem. C* **2015,** *3* (39), 10066-10069.

76. Xu, L.; Ding, S.-Y.; Liu, J.; Sun, J.; Wang, W.; Zheng, Q.-Y., Highly crystalline covalent organic frameworks from flexible building blocks. *Chem. Commun.* **2016,** *52* (25), 4706-4709.

77. Spitler, E. L.; Dichtel, W. R., Lewis acid-catalysed formation of two-dimensional phthalocyanine covalent organic frameworks. *Nat. Chem.* **2010,** *2* (8), 672-677.

78. Ding, X.; Guo, J.; Feng, X.; Honsho, Y.; Guo, J.; Seki, S.; Maitarad, P.; Saeki, A.; Nagase, S.; Jiang, D., Synthesis of Metallophthalocyanine Covalent Organic

Frameworks That Exhibit High Carrier Mobility and Photoconductivity. *Angew. Chem. Int. Ed.* **2011,** *50* (6), 1289-1293.

79. Alahakoon, S. B.; Thompson, C. M.; Nguyen, A. X.; Occhialini, G.; McCandless, G. T.; Smaldone, R. A., An azine-linked hexaphenylbenzene based covalent organic framework. *Chem. Commun.* **2016,** *52* (13), 2843-2845.

80. Xu, S.-Q.; Zhan, T.-G.; Wen, Q.; Pang, Z.-F.; Zhao, X., Diversity of Covalent Organic Frameworks (COFs): A 2D COF Containing Two Kinds of Triangular Micropores of Different Sizes. *ACS Macro Lett.* **2016,** *5* (1), 99-102.

81. Dalapati, S.; Jin, S.; Gao, J.; Xu, Y.; Nagai, A.; Jiang, D., An Azine-Linked Covalent Organic Framework. *J. Am. Chem. Soc.* **2013,** *135* (46), 17310-17313.

82. Chen, X.; Huang, N.; Gao, J.; Xu, H.; Xu, F.; Jiang, D., Towards covalent organic frameworks with predesignable and aligned open docking sites. *Chem. Commun.* **2014,** *50* (46), 6161-6163.

83. Dalapati, S.; Jin, E.; Addicoat, M.; Heine, T.; Jiang, D., Highly Emissive Covalent Organic Frameworks. *J. Am. Chem. Soc.* **2016,** *138* (18), 5797-5800.

84. Zhou, T.-Y.; Xu, S.-Q.; Wen, Q.; Pang, Z.-F.; Zhao, X., One-Step Construction of Two Different Kinds of Pores in a 2D Covalent Organic Framework. *J. Am. Chem. Soc.* **2014,** *136* (45), 15885-15888.

85. Côté, A. P.; Benin, A. I.; Ockwig, N. W.; Keeffe, M.; Matzger, A. J.; Yaghi, O. M., Porous, Crystalline, Covalent Organic Frameworks. *Science* **2005,** *310* (5751), 1166.

86. Uribe-Romo, F. J.; Hunt, J. R.; Furukawa, H.; Klöck, C.; O'Keeffe, M.; Yaghi, O. M., A Crystalline Imine-Linked 3-D Porous Covalent Organic Framework. *J. Am. Chem. Soc.* **2009,** *131* (13), 4570-4571.

87. Uribe-Romo, F. J.; Doonan, C. J.; Furukawa, H.; Oisaki, K.; Yaghi, O. M., Crystalline Covalent Organic Frameworks with Hydrazone Linkages. *J. Am. Chem. Soc.* **2011,** *133* (30), 11478-11481.

88. Guo, J.; Xu, Y.; Jin, S.; Chen, L.; Kaji, T.; Honsho, Y.; Addicoat, M. A.; Kim, J.; Saeki, A.; Ihee, H.; Seki, S.; Irle, S.; Hiramoto, M.; Gao, J.; Jiang, D., Conjugated organic framework with three-dimensionally ordered stable structure and delocalized π clouds. *Nat. Commun.* **2013,** *4* (1), 2736.

89. Fang, Q.; Zhuang, Z.; Gu, S.; Kaspar, R. B.; Zheng, J.; Wang, J.; Qiu, S.; Yan, Y., Designed synthesis of large-pore crystalline polyimide covalent organic frameworks. *Nat. Commun.* **2014,** *5* (1), 4503.

90. Kuhn, P.; Antonietti, M.; Thomas, A., Porous, Covalent Triazine-Based Frameworks Prepared by Ionothermal Synthesis. *Angew. Chem. Int. Ed.* **2008,** *47* (18), 3450-3453.

91. Jin, E.; Asada, M.; Xu, Q.; Dalapati, S.; Addicoat, M. A.; Brady, M. A.; Xu, H.; Nakamura, T.; Heine, T.; Chen, Q.; Jiang, D., Two-dimensional sp² carbon–conjugated covalent organic frameworks. *Science* **2017,** *357* (6352), 673.

92. Lyu, H.; Diercks, C. S.; Zhu, C.; Yaghi, O. M., Porous Crystalline Olefin-Linked Covalent Organic Frameworks. *J. Am. Chem. Soc.* **2019,** *141* (17), 6848-6852.

93. Ding, S.-Y.; Gao, J.; Wang, Q.; Zhang, Y.; Song, W.-G.; Su, C.-Y.; Wang, W., Construction of Covalent Organic Framework for Catalysis: Pd/COF-LZU1 in Suzuki–Miyaura Coupling Reaction. *J. Am. Chem. Soc.* **2011,** *133* (49), 19816-19822.

94. Chan-Thaw, C. E.; Villa, A.; Katekomol, P.; Su, D.; Thomas, A.; Prati, L., Covalent Triazine Framework as Catalytic Support for Liquid Phase Reaction. *Nano Lett.* **2010,** *10* (2), 537-541.

95. Rozhko, E.; Bavykina, A.; Osadchii, D.; Makkee, M.; Gascon, J., Covalent organic frameworks as supports for a molecular Ni based ethylene oligomerization catalyst for the synthesis of long chain olefins. *J. Catal.* **2017,** *345*, 270-280.

96. Shi, X.; Yao, Y.; Xu, Y.; Liu, K.; Zhu, G.; Chi, L.; Lu, G., Imparting Catalytic Activity to a Covalent Organic Framework Material by Nanoparticle Encapsulation. *ACS Appl. Mater. Interfaces* **2017,** *9* (8), 7481-7488.

97. Pachfule, P.; Kandambeth, S.; Díaz Díaz, D.; Banerjee, R., Highly stable covalent organic framework–Au nanoparticles hybrids for enhanced activity for nitrophenol reduction. *Chem. Commun.* **2014,** *50* (24), 3169-3172.

98. Xu, H.; Chen, X.; Gao, J.; Lin, J.; Addicoat, M.; Irle, S.; Jiang, D., Catalytic covalent organic frameworks via pore surface engineering. *Chem. Commun.* **2014,** *50* (11), 1292-1294.

99. Vyas, V. S.; Haase, F.; Stegbauer, L.; Savasci, G.; Podjaski, F.; Ochsenfeld, C.; Lotsch, B. V., A tunable azine covalent organic framework platform for visible light-induced hydrogen generation. *Nat. Commun.* **2015,** *6* (1), 8508.

100. Banerjee, T.; Haase, F.; Savasci, G.; Gottschling, K.; Ochsenfeld, C.; Lotsch, B. V., Single-Site Photocatalytic H2 Evolution from Covalent Organic Frameworks with Molecular Cobaloxime Co-Catalysts. *J. Am. Chem. Soc.* **2017,** *139* (45), 16228-16234.

101. Wang, X.; Chen, L.; Chong, S. Y.; Little, M. A.; Wu, Y.; Zhu, W.-H.; Clowes, R.; Yan, Y.; Zwijnenburg, M. A.; Sprick, R. S.; Cooper, A. I., Sulfone-containing covalent organic frameworks for photocatalytic hydrogen evolution from water. *Nat. Chem.* **2018,** *10* (12), 1180-1189.

102. Bi, S.; Yang, C.; Zhang, W.; Xu, J.; Liu, L.; Wu, D.; Wang, X.; Han, Y.; Liang, Q.; Zhang, F., Two-dimensional semiconducting covalent organic frameworks via condensation at arylmethyl carbon atoms. *Nat. Commun.* **2019,** *10* (1), 2467.

103. Jin, E. Q.; Lan, Z. A.; Jiang, Q. H.; Geng, K. Y.; Li, G. S.; Wang, X. C.; Jiang, D. L., 2D sp(2) Carbon-Conjugated Covalent Organic Frameworks for Photocatalytic Hydrogen Production from Water. *Chem* **2019,** *5* (6), 1632-1647.

104. Hou, C. C.; Li, T. T.; Cao, S.; Chen, Y.; Fu, W. F., Incorporation of a Ru(dcbpy)(bpy)$_2$ (2+) photosensitizer and a Pt(dcbpy)Cl-2 catalyst into metal-organic frameworks for photocatalytic hydrogen evolution from aqueous solution. *J. Mater. Chem. A* **2015,** *3* (19), 10386-10394.

105. Eggleston, D. S.; Goldsby, K. A.; Hodgson, D. J.; Meyer, T. J., Structural variations induced by changes in oxidation state and their role in electron transfer. Crystal and molecular structures of cis-[Ru(bpy)$_2$Cl$_2$]3.5H$_2$O and cis-[Ru(bpy)2Cl2]Cl.2H2O. *Inorg. Chem.* **1985,** *24* (26), 4573-4580.

106. Zhou, H. C.; Long, J. R.; Yaghi, O. M., Introduction to Metal-Organic Frameworks. *Chem. Rev.* **2012,** *112* (2), 673-674.

107. Cook, T. R.; Zheng, Y. R.; Stang, P. J., Metal-Organic Frameworks and Self-Assembled Supramolecular Coordination Complexes: Comparing and Contrasting the Design, Synthesis, and Functionality of Metal-Organic Materials. *Chem. Rev.* **2013,** *113* (1), 734-777.

108. Wang, C.; Liu, D. M.; Lin, W. B., Metal-Organic Frameworks as A Tunable Platform for Designing Functional Molecular Materials. *J. Am. Chem. Soc.* **2013,** *135* (36), 13222-13234.

109. Kitagawa, S.; Kitaura, R.; Noro, S., Functional porous coordination polymers. *Angew. Chem. Int. Ed.* **2004,** *43* (18), 2334-2375.

110. Moulton, B.; Zaworotko, M. J., From molecules to crystal engineering: Supramolecular isomerism and polymorphism in network solids. *Chem. Rev.* **2001,** *101* (6), 1629-1658.

111. Farha, O. K.; Spokoyny, A. M.; Mulfort, K. L.; Hawthorne, M. F.; Mirkin, C. A.; Hupp, J. T., Synthesis and hydrogen sorption properties of carborane based metal-

organic framework materials. *J. Am. Chem. Soc.* **2007,** *129* (42), 12680-+.

112. Furukawa, H.; Cordova, K. E.; O'Keeffe, M.; Yaghi, O. M., The Chemistry and Applications of Metal-Organic Frameworks. *Science* **2013,** *341* (6149), 974-+.

113. Foo, M. L.; Matsuda, R.; Kitagawa, S., Functional Hybrid Porous Coordination Polymers. *Chem. Mater.* **2014,** *26* (1), 310-322.

114. Sumida, K.; Rogow, D. L.; Mason, J. A.; McDonald, T. M.; Bloch, E. D.; Herm, Z. R.; Bae, T. H.; Long, J. R., Carbon Dioxide Capture in Metal-Organic Frameworks. *Chem. Rev.* **2012,** *112* (2), 724-781.

115. Rowsell, J. L. C.; Spencer, E. C.; Eckert, J.; Howard, J. A. K.; Yaghi, O. M., Gas adsorption sites in a large-pore metal-organic framework. *Science* **2005,** *309* (5739), 1350-1354.

116. Kesanli, B.; Cui, Y.; Smith, M. R.; Bittner, E. W.; Bockrath, B. C.; Lin, W. B., Highly interpenetrated metal-organic frameworks for hydrogen storage. *Angew. Chem. Int. Ed.* **2005,** *44* (1), 72-75.

117. Hu, Z. C.; Deibert, B. J.; Li, J., Luminescent metal-organic frameworks for chemical sensing and explosive detection. *Chem. Soc. Rev.* **2014,** *43* (16), 5815-5840.

118. Zhang, T.; Lin, W. B., Metal-organic frameworks for artificial photosynthesis and photocatalysis. *Chem. Soc. Rev.* **2014,** *43* (16), 5982-5993.

119. Dhakshinamoorthy, A.; Asiri, A. M.; Garcia, H., Metal-Organic Framework (MOF) Compounds: Photocatalysts for Redox Reactions and Solar Fuel Production. *Angew. Chem. Int. Ed.* **2016,** *55* (18), 5414-5445.

120. Corma, A.; Garcia, H.; Xamena, F., Engineering Metal Organic Frameworks for Heterogeneous Catalysis. *Chem. Rev.* **2010,** *110* (8), 4606-4655.

121. Yoon, M.; Srirambalaji, R.; Kim, K., Homochiral Metal-Organic Frameworks for Asymmetric Heterogeneous Catalysis. *Chem. Rev.* **2012,** *112* (2), 1196-1231.

122. Jiang, J. C.; Yaghi, O. M., Bronsted Acidity in Metal-Organic Frameworks. *Chem. Rev.* **2015,** *115* (14), 6966-6997.

123. Ma, L. Q.; Abney, C.; Lin, W. B., Enantioselective catalysis with homochiral metal-organic frameworks. *Chem. Soc. Rev.* **2009,** *38* (5), 1248-1256.

124. Lee, J.; Farha, O. K.; Roberts, J.; Scheidt, K. A.; Nguyen, S. T.; Hupp, J. T., Metal-organic framework materials as catalysts. *Chem. Soc. Rev.* **2009,** *38* (5), 1450-

1459.

125. Pimentel, B. R.; Parulkar, A.; Zhou, E. K.; Brunelli, N. A.; Lively, R. P., Zeolitic Imidazolate Frameworks: Next-Generation Materials for Energy-Efficient Gas Separations. *ChemSusChem* **2014,** *7* (12), 3202-3240.

126. Phan, A.; Doonan, C. J.; Uribe-Romo, F. J.; Knobler, C. B.; O'Keeffe, M.; Yaghi, O. M., Synthesis, Structure, and Carbon Dioxide Capture Properties of Zeolitic Imidazolate Frameworks. *Acc. Chem. Res.* **2010,** *43* (1), 58-67.

127. Esken, D.; Turner, S.; Lebedev, O. I.; Van Tendeloo, G.; Fischer, R. A., Au@ZIFs: Stabilization and Encapsulation of Cavity-Size Matching Gold Clusters inside Functionalized Zeolite Imidazolate Frameworks, ZIFs. *Chem. Mater.* **2010,** *22* (23), 6393-6401.

128. Dang, T. T.; Ramalingam, B.; Shan, S. P.; Seayad, A. M., An Efficient Palladium-Catalyzed N-Alkylation of Amines Using Primary and Secondary Alcohols. *ACS Catal.* **2013,** *3* (11), 2536-2540.

129. Xamena, F.; Casanova, O.; Tailleur, R. G.; Garcia, H.; Corma, A., Metal organic frameworks (MOFs) as catalysts: A combination of Cu2+ and Co2+ MOFs as an efficient catalyst for tetralin oxidation. *J. Catal.* **2008,** *255* (2), 220-227.

130. Chizallet, C.; Lazare, S.; Bazer-Bachi, D.; Bonnier, F.; Lecocq, V.; Soyer, E.; Quoineaud, A. A.; Bats, N., Catalysis of Transesterification by a Nonfunctionalized Metal-Organic Framework: Acido-Basicity at the External Surface of ZIF-8 Probed by FTIR and ab Initio Calculations. *J. Am. Chem. Soc.* **2010,** *132* (35), 12365-12377.

131. Tran, U. P. N.; Le, K. K. A.; Phan, N. T. S., Expanding Applications of Metal-Organic Frameworks: Zeolite Imidazolate Framework ZIF-8 as an Efficient Heterogeneous Catalyst for the Knoevenagel Reaction. *ACS Catal.* **2011,** *1* (2), 120-127.

132. Jiang, H. L.; Liu, B.; Akita, T.; Haruta, M.; Sakurai, H.; Xu, Q., Au@ZIF-8: CO Oxidation over Gold Nanoparticles Deposited to Metal-Organic Framework. *J. Am. Chem. Soc.* **2009,** *131* (32), 11302-+.

133. Kuo, C. H.; Tang, Y.; Chou, L. Y.; Sneed, B. T.; Brodsky, C. N.; Zhao, Z. P.; Tsung, C. K., Yolk-Shell Nanocrystal@ZIF-8 Nanostructures for Gas-Phase Heterogeneous Catalysis with Selectivity Control. *J. Am. Chem. Soc.* **2012,** *134* (35), 14345-14348.

134. Yang, H.; He, X. W.; Wang, F.; Kang, Y.; Zhang, J., Doping copper into ZIF-67 for enhancing gas uptake capacity and visible-light-driven photocatalytic

degradation of organic dye. *J. Mater. Chem.* **2012,** *22* (41), 21849-21851.

135. Wang, S. B.; Yao, W. S.; Lin, J. L.; Ding, Z. X.; Wang, X. C., Cobalt Imidazolate Metal-Organic Frameworks Photosplit CO_2 under Mild Reaction Conditions. *Angew. Chem. Int. Ed.* **2014,** *53* (4), 1034-1038.

136. Isimjan, T. T.; Kazemian, H.; Rohani, S.; Ray, A. K., Photocatalytic activities of Pt/ZIF-8 loaded highly ordered TiO2 nanotubes. *J. Mater. Chem.* **2010,** *20* (45), 10241-10245.

137. Dey, C.; Banerjee, R., Controlled synthesis of a catalytically active hybrid metal-oxide incorporated zeolitic imidazolate framework (MOZIF). *Chem. Commun.* **2013,** *49* (59), 6617-6619.

138. Corma, A.; Garcia, H., Zeolite-based photocatalysts. *Chem. Commun.* **2004,** (13), 1443-1459.

139. Pattengale, B.; Yang, S. Z.; Ludwig, J.; Huang, Z. Q.; Zhang, X. Y.; Huang, J., Exceptionally Long-Lived Charge Separated State in Zeolitic Imidazolate Framework: Implication for Photocatalytic Applications. *J. Am. Chem. Soc.* **2016,** *138* (26), 8072-8075.

140. Zhang, Q. Q.; Zhang, C. K.; Cao, L. Y.; Wang, Z.; An, B.; Lin, Z. K.; Huang, R. Y.; Zhang, Z. M.; Wang, C.; Lin, W. B., Forster Energy Transport in Metal-Organic Frameworks Is Beyond Step-by-Step Hopping. *J. Am. Chem. Soc.* **2016,** *138* (16), 5308-5315.

141. Lee, C. Y.; Farha, O. K.; Hong, B. J.; Sarjeant, A. A.; Nguyen, S. T.; Hupp, J. T., Light-Harvesting Metal-Organic Frameworks (MOFs): Efficient Strut-to-Strut Energy Transfer in Bodipy and Porphyrin-Based MOFs. *J. Am. Chem. Soc.* **2011,** *133* (40), 15858-15861.

142. Kent, C. A.; Mehl, B. P.; Ma, L. Q.; Papanikolas, J. M.; Meyer, T. J.; Lin, W. B., Energy Transfer Dynamics in Metal-Organic Frameworks. *J. Am. Chem. Soc.* **2010,** *132* (37), 12767-12769.

143. Son, H. J.; Jin, S. Y.; Patwardhan, S.; Wezenberg, S. J.; Jeong, N. C.; So, M.; Wilmer, C. E.; Sarjeant, A. A.; Schatz, G. C.; Snurr, R. Q.; Farha, O. K.; Wiederrecht, G. P.; Hupp, J. T., Light-Harvesting and Ultrafast Energy Migration in Porphyrin-Based Metal-Organic Frameworks. *J. Am. Chem. Soc.* **2013,** *135* (2), 862-869.

144. Nazeeruddin, M. K.; Kay, A.; Rodicio, I.; Humphrybaker, R.; Muller, E.; Liska, P.; Vlachopoulos, N.; Gratzel, M., Conversion of Light to Electricity by Cis-X2Bis(2,2'-Bipyridyl-4,4'-Dicarboxylated)Ruthenium(II) Charge-Transfer Sensitizers

(X = Cl-, Br-, I-, CN-, and SCN-) on Nanocrystalline TiO_2 Electrodes. *J. Am. Chem. Soc.* **1993,** *115* (14), 6382-6390.

145. Xia, W.; Zhu, J. H.; Guo, W. H.; An, L.; Xia, D. G.; Zou, R. Q., Well-defined Carbon Polyhedrons Prepared From Nano Metal-Organic Frameworks for Oxygen Reduction. *J. Mater. Chem. A* **2014,** *2* (30), 11606-11613.

146. Damrauer, N. H.; McCusker, J. K., Ultrafast dynamics in the metal-to-ligand charge transfer excited-state evolution of Ru(4,4 '-diphenyl-2,2 '-bipyridine)(3) (2+). *J. Phys. Chem. A* **1999,** *103* (42), 8440-8446.

147. Argazzi, R.; Bignozzi, C. A.; Heimer, T. A.; Castellano, F. N.; Meyer, G. J., Enhanced Spectral Sensitivity From Ruthenium(II) Polypyridy Based Photovoltaic Devices. *Inorg. Chem.* **1994,** *33* (25), 5741-5749.

148. Yang, L. L.; Yu, L.; Sun, M.; Gao, C., Zeolitic imidazole framework-67 as an efficient heterogeneous catalyst for the synthesis of ethyl methyl carbonate. *Catal. Commun.* **2014,** *54*, 86-90.

149. Tang, Y.; Pattengale, B.; Ludwig, J.; Atifi, A.; Zinovev, A. V.; Dong, B.; Kong, Q. Y.; Zuo, X. B.; Zhang, X. Y.; Huang, J., Direct Observation of Photoinduced Charge Separation in Ruthenium Complex/Ni(OH)(2) Nanoparticle Hybrid. *Sci Rep* **2015,** *5*, 6.

150. Du, P. W.; Knowles, K.; Eisenberg, R., A homogeneous system for the photogeneration of hydrogen from water based on a platinum(II) terpyridyl acetylide chromophore and a molecular cobalt catalyst. *J. Am. Chem. Soc.* **2008,** *130* (38), 12576-+.

151. Du, P. W.; Schneider, J.; Luo, G. G.; Brennessel, W. W.; Eisenberg, R., Visible Light-Driven Hydrogen Production from Aqueous Protons Catalyzed by Molecular Cobaloxime Catalysts (vol 48, pg 4962, 2009). *Inorg. Chem.* **2009,** *48* (17), 8646-8646.

152. Shen, L. J.; Luo, M. B.; Huang, L. J.; Feng, P. Y.; Wu, L., A Clean and General Strategy To Decorate a Titanium Metal Organic Framework with Noble-Metal Nanoparticles for Versatile Photocatalytic Applications. *Inorg. Chem.* **2015,** *54* (4), 1191-1193.

153. Horiuchi, Y.; Toyao, T.; Saito, M.; Mochizuki, K.; Iwata, M.; Higashimura, H.; Anpo, M.; Matsuoka, M., Visible-Light-Promoted Photocatalytic Hydrogen Production by Using an Amino-Functionalized Ti(IV) Metal-Organic Framework. *J. Phys. Chem. C* **2012,** *116* (39), 20848-20853.

154. Zhang, Z. M.; Zhang, T.; Wang, C.; Lin, Z. K.; Long, L. S.; Lin, W. B., Photosensitizing Metal Organic Framework Enabling Visible-Light-Driven Proton Reduction by a Wells-Dawson-Type Polyoxometalate. *J. Am. Chem. Soc.* **2015,** *137* (9), 3197-3200.

155. Gratzel, M., Artificial Photosynthesis - Water Cleavage into Hydrogen and Oxygen by Visible-Light. *Accounts of Chemical Research* **1981,** *14* (12), 376-384.

156. Chen, X. B.; Shen, S. H.; Guo, L. J.; Mao, S. S., Semiconductor-based Photocatalytic Hydrogen Generation. *Chem. Rev.* **2010,** *110* (11), 6503-6570.

157. Wen, F. Y.; Li, C., Hybrid Artificial Photosynthetic Systems Comprising Semiconductors as Light Harvesters and Biomimetic Complexes as Molecular Cocatalysts. *Acc. Chem. Res.* **2013,** *46* (11), 2355-2364.

158. Bard, A. J.; Fox, M. A., Artificial Photosynthesis - Solar Splitting of Water to Hydrogen and Oxygen. *Acc. Chem. Res.* **1995,** *28* (3), 141-145.

159. Han, Z. J.; Qiu, F.; Eisenberg, R.; Holland, P. L.; Krauss, T. D., Robust Photogeneration of H-2 in Water Using Semiconductor Nanocrystals and a Nickel Catalyst. *Science* **2012,** *338* (6112), 1321-1324.

160. Das, A.; Han, Z. J.; Haghighi, M. G.; Eisenberg, R., Photogeneration of hydrogen from water using CdSe nanocrystals demonstrating the importance of surface exchange. *Proc. Natl. Acad. Sci. U. S. A.* **2013,** *110* (42), 16716-16723.

161. McNamara, W. R.; Han, Z. J.; Alperin, P. J.; Brennessel, W. W.; Holland, P. L.; Eisenberg, R., A Cobalt-Dithiolene Complex for the Photocatalytic and Electrocatalytic Reduction of Protons. *J. Am. Chem. Soc.* **2011,** *133* (39), 15368-15371.

162. Gartner, F.; Sundararaju, B.; Surkus, A. E.; Boddien, A.; Loges, B.; Junge, H.; Dixneuf, P. H.; Beller, M., Light-Driven Hydrogen Generation: Efficient Iron-Based Water Reduction Catalysts. *Angew. Chem. Int. Ed.* **2009,** *48* (52), 9962-9965.

163. Han, Z. J.; McNamara, W. R.; Eum, M. S.; Holland, P. L.; Eisenberg, R., A Nickel Thiolate Catalyst for the Long-Lived Photocatalytic Production of Hydrogen in a Noble-Metal-Free System. *Angew. Chem. Int. Ed.* **2012,** *51* (7), 1667-1670.

164. Fihri, A.; Artero, V.; Pereira, A.; Fontecave, M., Efficient H-2-producing photocatalytic systems based on cyclometalated iridium- and tricarbonylrhenium-diimine photosensitizers and cobaloxime catalysts. *Dalton Trans.* **2008,** (41), 5567-5569.

165. Sakata, T.; Kawai, T.; Hashimoto, K., Photochemical Diode Model of Pt-Tio2 Particle and Its Photocatalytic Activity. *Chem. Phys. Lett.* **1982,** *88* (1), 50-54.

166. Acharya, K. P.; Khnayzer, R. S.; O'Connor, T.; Diederich, G.; Kirsanova, M.; Klinkova, A.; Roth, D.; Kinder, E.; Imboden, M.; Zamkov, M., The Role of Hole Localization in Sacrificial Hydrogen Production by Semiconductor-Metal Heterostructured Nanocrystals. *Nano Lett.* **2011,** *11* (7), 2919-2926.

167. Berr, M.; Vaneski, A.; Susha, A. S.; Rodriguez-Fernandez, J.; Doblinger, M.; Jackel, F.; Rogach, A. L.; Feldmann, J., Colloidal CdS nanorods decorated with subnanometer sized Pt clusters for photocatalytic hydrogen generation. *Appl. Phys. Lett.* **2010,** *97* (9).

168. Amirav, L.; Alivisatos, A. P., Photocatalytic Hydrogen Production with Tunable Nanorod Heterostructures. *J. Phys. Chem. Lett.* **2010,** *1* (7), 1051-1054.

169. Yan, H. J.; Yang, J. H.; Ma, G. J.; Wu, G. P.; Zong, X.; Lei, Z. B.; Shi, J. Y.; Li, C., Visible-light-driven hydrogen production with extremely high quantum efficiency on Pt-PdS/CdS photocatalyst. *J. Catal.* **2009,** *266* (2), 165-168.

170. Rosi, N. L.; Eckert, J.; Eddaoudi, M.; Vodak, D. T.; Kim, J.; O'Keeffe, M.; Yaghi, O. M., Hydrogen storage in microporous metal-organic frameworks. *Science* **2003,** *300* (5622), 1127-1129.

171. Li, Z.; Xiao, J. D.; Jiang, H. L., Encapsulating a Co(II) Molecular Photocatalyst in Metal-Organic Framework for Visible-Light-Driven H-2 Production: Boosting Catalytic Efficiency via Spatial Charge Separation. *ACS Catal.* **2016,** *6* (8), 5359-5365.

172. Zhang, T.; Manna, K.; Lin, W. B., Metal-Organic Frameworks Stabilize Solution-Inaccessible Cobalt Catalysts for Highly Efficient Broad-Scope Organic Transformations. *J. Am. Chem. Soc.* **2016,** *138* (9), 3241-3249.

173. Rimoldi, M.; Nakamura, A.; Vermeulen, N. A.; Henkelis, J. J.; Blackburn, A. K.; Hupp, J. T.; Stoddart, J. F.; Farha, O. K., A metal-organic framework immobilised iridium pincer complex. *Chem. Sci.* **2016,** *7* (8), 4980-4984.

174. Kim, D.; Whang, D. R.; Park, S. Y., Self-healing of molecular catalyst and photosensitizer on metal-organic framework: robust molecular system for photocatalytic H_2 evolution from water. *J. Am. Chem. Soc.* **2016,** *138* (28), 8698-701.

175. de Miguel, M.; Ragon, F.; Devic, T.; Serre, C.; Horcajada, P.; Garcia, H., Evidence of photoinduced charge separation in the metal-organic framework MIL-125(Ti)-NH_2. *ChemPhysChem* **2012,** *13* (16), 3651-4.

176. Laurier, K. G.; Fron, E.; Atienzar, P.; Kennes, K.; Garcia, H.; Van der Auweraer, M.; De Vos, D. E.; Hofkens, J.; Roeffaers, M. B., Delayed electron-hole pair recombination in iron(III)-oxo metal-organic frameworks. *Phys. Chem. Chem. Phys.* **2014,** *16* (11), 5044-7.

177. Fateeva, A.; Chater, P. A.; Ireland, C. P.; Tahir, A. A.; Khimyak, Y. Z.; Wiper, P. V.; Darwent, J. R.; Rosseinsky, M. J., A water-stable porphyrin-based metal-organic framework active for visible-light photocatalysis. *Angew. Chem. Int. Ed. Engl.* **2012,** *51* (30), 7440-4.

178. Takaishi, S.; DeMarco, E. J.; Pellin, M. J.; Farha, O. K.; Hupp, J. T., Solvent-assisted linker exchange (SALE) and post-assembly metallation in porphyrinic metal-organic framework materials. *Chem. Sci.* **2013,** *4* (4), 1509-1513.

179. Barron, P. M.; Wray, C. A.; Hu, C. H.; Guo, Z. Y.; Choe, W., A Bioinspired Synthetic Approach for Building Metal-Organic Frameworks with Accessible Metal Centers. *Inorg. Chem.* **2010,** *49* (22), 10217-10219.

180. Xu, H. Q.; Hu, J. H.; Wang, D. K.; Li, Z. H.; Zhang, Q.; Luo, Y.; Yu, S. H.; Jiang, H. L., Visible-Light Photoreduction of CO2 in a Metal-Organic Framework: Boosting Electron-Hole Separation via Electron Trap States. *J. Am. Chem. Soc.* **2015,** *137* (42), 13440-13443.

181. Fateeva, A.; Chater, P. A.; Ireland, C. P.; Tahir, A. A.; Khimyak, Y. Z.; Wiper, P. V.; Darwent, J. R.; Rosseinsky, M. J., A Water-Stable Porphyrin-Based Metal-Organic Framework Active for Visible-Light Photocatalysis. *Angew. Chem. Int. Ed.* **2012,** *51* (30), 7440-7444.

182. Maza, W. A.; Padilla, R.; Morris, A. J., Concentration Dependent Dimensionality of Resonance Energy Transfer in a Postsynthetically Doped Morphologically Homologous Analogue of UiO-67 MOF with a Ruthenium(II) Polypyridyl Complex. *J. Am. Chem. Soc.* **2015,** *137* (25), 8161-8168.

183. Zhang, S. Q.; Li, L. N.; Zhao, S. G.; Sun, Z. H.; Luo, J. H., Construction of Interpenetrated Ruthenium Metal-Organic Frameworks as Stable Photocatalysts for CO2 Reduction. *Inorg. Chem.* **2015,** *54* (17), 8375-8379.

184. Hou, C. C.; Li, T. T.; Cao, S.; Chen, Y.; Fu, W. F., Incorporation of a [Ru(dcbpy)(bpy)(2)](2+) photosensitizer and a Pt(dcbpy)Cl-2 catalyst into metal-organic frameworks for photocatalytic hydrogen evolution from aqueous solution. *J. Mater. Chem. A* **2015,** *3* (19), 10386-10394.

185. Nguyen, H. G. T.; Schweitzer, N. M.; Chang, C.-Y.; Drake, T. L.; So, M. C.; Stair, P. C.; Farha, O. K.; Hupp, J. T.; Nguyen, S. T., Vanadium-Node-Functionalized

UiO-66: A Thermally Stable MOF-Supported Catalyst for the Gas-Phase Oxidative Dehydrogenation of Cyclohexene. *ACS Catal.* **2014,** *4* (8), 2496-2500.

186. Kataoka, Y.; Sato, K.; Miyazaki, Y.; Masuda, K.; Tanaka, H.; Naito, S.; Mori, W., Photocatalytic hydrogen production from water using porous material [Ru-2(p-BDC)(2)](n). *Energy Environ. Sci.* **2009,** *2* (4), 397-400.

187. Wang, C.; Xie, Z. G.; deKrafft, K. E.; Lin, W. L., Doping Metal-Organic Frameworks for Water Oxidation, Carbon Dioxide Reduction, and Organic Photocatalysis. *J. Am. Chem. Soc.* **2011,** *133* (34), 13445-13454.

188. Huang, R. Y.; Peng, Y.; Wang, C.; Shi, Z.; Lin, W. B., A Rhenium-Functionalized Metal-Organic Framework as a Single-Site Catalyst for Photochemical Reduction of Carbon Dioxide. *Eur. J. Inorg. Chem.* **2016,** (27), 4358-4362.

189. Sasan, K.; Lin, Q. P.; Mao, C. Y.; Feng, P. Y., Incorporation of iron hydrogenase active sites into a highly stable metal-organic framework for photocatalytic hydrogen generation. *Chem. Commun.* **2014,** *50* (72), 10390-10393.

190. Pullen, S.; Fei, H. H.; Orthaber, A.; Cohen, S. M.; Ott, S., Enhanced Photochemical Hydrogen Production by a Molecular Diiron Catalyst Incorporated into a Metal-Organic Framework. *J. Am. Chem. Soc.* **2013,** *135* (45), 16997-17003.

191. Kim, D.; Whang, D. R.; Park, S. Y., Self-Healing of Molecular Catalyst and Photosensitizer on Metal-Organic Framework: Robust Molecular System for Photocatalytic H-2 Evolution from Water. *J. Am. Chem. Soc.* **2016,** *138* (28), 8698-8701.

192. Kim, D.; Whang, D. R.; Park, S. Y., Self-Healing of Molecular Catalyst and Photosensitizer on Metal–Organic Framework: Robust Molecular System for Photocatalytic H2 Evolution from Water. *J. Am. Chem. Soc.* **2016,** *138* (28), 8698-8701.

193. Wang, C.; Liu, D.; Lin, W., Metal–Organic Frameworks as A Tunable Platform for Designing Functional Molecular Materials. *J. Am. Chem. Soc.* **2013,** *135* (36), 13222-13234.

194. Kent, C. A.; Mehl, B. P.; Ma, L.; Papanikolas, J. M.; Meyer, T. J.; Lin, W., Energy Transfer Dynamics in Metal−Organic Frameworks. *J. Am. Chem. Soc.* **2010,** *132* (37), 12767-12769.

195. Manna, K.; Zhang, T.; Lin, W., Postsynthetic Metalation of Bipyridyl-Containing Metal–Organic Frameworks for Highly Efficient Catalytic Organic Transformations. *J. Am. Chem. Soc.* **2014,** *136* (18), 6566-6569.

196. Maza, W. A.; Morris, A. J., Photophysical Characterization of a Ruthenium(II) Tris(2,2′-bipyridine)-Doped Zirconium UiO-67 Metal–Organic Framework. *J. Phys. Chem. C* **2014,** *118* (17), 8803-8817.

197. Roy, S.; Pascanu, V.; Pullen, S.; González Miera, G.; Martín-Matute, B.; Ott, S., Catalyst accessibility to chemical reductants in metal–organic frameworks. *Chem. Commun.* **2017,** *53* (22), 3257-3260.

198. So, M. C.; Wiederrecht, G. P.; Mondloch, J. E.; Hupp, J. T.; Farha, O. K., Metal–organic framework materials for light-harvesting and energy transfer. *Chem. Commun.* **2015,** *51* (17), 3501-3510.

199. Kent, C. A.; Liu, D.; Ma, L.; Papanikolas, J. M.; Meyer, T. J.; Lin, W., Light Harvesting in Microscale Metal–Organic Frameworks by Energy Migration and Interfacial Electron Transfer Quenching. *J. Am. Chem. Soc.* **2011,** *133* (33), 12940-12943.

200. Kent, C. A.; Liu, D.; Meyer, T. J.; Lin, W., Amplified Luminescence Quenching of Phosphorescent Metal–Organic Frameworks. *J. Am. Chem. Soc.* **2012,** *134* (9), 3991-3994.

201. Tsai, Y. W.; Tseng, Y. L.; Sarma, L. S.; Liu, D. G.; Lee, J. F.; Hwang, B. J., Genesis of Pt clusters in reverse micelles investigated by in situ X-ray absorption spectroscopy. *J. Phys. Chem. B* **2004,** *108* (24), 8148-8152.

202. Horsley, J. A., Relationship between the Area of L2,3 X-Ray Absorption-Edge Resonances and the D Orbital Occupancy in Compounds of Platinum and Iridium. *J. Chem. Phys.* **1982,** *76* (3), 1451-1458.

203. Esswein, A. J.; Nocera, D. G., Hydrogen production by molecular photocatalysis. *Chem. Rev.* **2007,** *107* (10), 4022-4047.

204. Lewis, N. S.; Nocera, D. G., Powering the planet: Chemical challenges in solar energy utilization. *Proc. Natl. Acad. Sci. U. S. A.* **2006,** *103* (43), 15729-15735.

205. Moore, G. F.; Brudvig, G. W., Energy conversion in photosynthesis: a paradigm for solar fuel production. *Annu Rev Conden Ma P* **2011,** *2*, 303-327.

206. Reece, S. Y.; Hamel, J. A.; Sung, K.; Jarvi, T. D.; Esswein, A. J.; Pijpers, J. J. H.; Nocera, D. G., Wireless solar water splitting using silicon-based semiconductors and earth-abundant catalysts. *Science* **2011,** *334* (6056), 645-648.

207. Youngblood, W. J.; Lee, S. H.; Kobayashi, Y.; Hernandez-Pagan, E. A.; Hoertz, P. G.; Moore, T. A.; Moore, A. L.; Gust, D.; Mallouk, T. E., Photoassisted

overall water splitting in a visible light-absorbing dye-sensitized photoelectrochemical cell. *J. Am. Chem. Soc.* **2009,** *131* (3), 926-7.

208. Gartner, F.; Sundararaju, B.; Surkus, A. E.; Boddien, A.; Loges, B.; Junge, H.; Dixneuf, P. H.; Beller, M., Light-Driven Hydrogen Generation: Efficient Iron-Based Water Reduction Catalysts. *Angew. Chem. Int. Ed.* **2009,** *48* (52), 9962-9965.

209. Na, Y.; Wang, M.; Pan, J. X.; Zhang, P.; Akermark, B.; Sun, L. C., Visible light-driven electron transfer and hydrogen generation catalyzed by bioinspired [2Fe2S] complexes. *Inorg. Chem.* **2008,** *47* (7), 2805-2810.

210. Lazarides, T.; McCormick, T.; Du, P. W.; Luo, G. G.; Lindley, B.; Eisenberg, R., Making hydrogen from water using a homogeneous system without noble metals. *J. Am. Chem. Soc.* **2009,** *131* (26), 9192-4.

211. Dempsey, J. L.; Brunschwig, B. S.; Winkler, J. R.; Gray, H. B., Hydrogen evolution catalyzed by cobaloximes. *Acc. Chem. Res.* **2009,** *42* (12), 1995-2004.

212. Llabrés i Xamena, F. X.; Corma, A.; Garcia, H., Applications for metal−organic frameworks (MOFs) as quantum dot semiconductors. *J. Phys. Chem. C* **2007,** *111* (1), 80-85.

213. Feng, D.; Gu, Z. Y.; Li, J. R.; Jiang, H. L.; Wei, Z.; Zhou, H. C., Zirconium-metalloporphyrin PCN-222: mesoporous metal-organic frameworks with ultrahigh stability as biomimetic catalysts. *Angew. Chem. Int. Ed.* **2012,** *51* (41), 10307-10.

214. Bai, Y.; Dou, Y.; Xie, L. H.; Rutledge, W.; Li, J. R.; Zhou, H. C., Zr-based metal-organic frameworks: design, synthesis, structure, and applications. *Chem. Soc. Rev.* **2016,** *45* (8), 2327-67.

215. Kim, D.; Whang, D. R.; Park, S. Y., Self-healing of molecular catalyst and photosensitizer on metal-organic framework: robust molecular system for photocatalytic H_2 evolution from water. *J. Am. Chem. Soc.* **2016,** *138* (28), 8698-701.

216. Laurier, K. G.; Fron, E.; Atienzar, P.; Kennes, K.; Garcia, H.; Van der Auweraer, M.; De Vos, D. E.; Hofkens, J.; Roeffaers, M. B., Delayed electron-hole pair recombination in iron(III)-oxo metal-organic frameworks. *PCCP* **2014,** *16* (11), 5044-7.

217. Fateeva, A.; Chater, P. A.; Ireland, C. P.; Tahir, A. A.; Khimyak, Y. Z.; Wiper, P. V.; Darwent, J. R.; Rosseinsky, M. J., A water-stable porphyrin-based metal-organic framework active for visible-light photocatalysis. *Angew. Chem. Int. Ed.* **2012,** *51* (30), 7440-4.

218. Sawano, T.; Lin, Z. K.; Boures, D.; An, B.; Wang, C.; Lin, W. B., Metal-Organic Frameworks Stabilize Mono(phosphine)-Metal Complexes for Broad-Scope Catalytic Reactions. *J. Am. Chem. Soc.* **2016,** *138* (31), 9783-9786.

219. Burgess, S. A.; Kassie, A.; Baranowski, S. A.; Fritzsching, K. J.; Schmidt-Rohr, K.; Brown, C. M.; Wade, C. R., Improved Catalytic Activity and Stability of a Palladium Pincer Complex by Incorporation into a Metal–Organic Framework. *J. Am. Chem. Soc.* **2016,** *138* (6), 1780-1783.

220. Fei, H. H.; Cohen, S. M., A robust, catalytic metal-organic framework with open 2,2 '- bipyridine sites. *Chem. Commun.* **2014,** *50* (37), 4810-4812.

221. Yu, X.; Cohen, S. M., Photocatalytic metal-organic frameworks for the aerobic oxidation of arylboronic acids. *Chem. Commun.* **2015,** *51* (48), 9880-9883.

222. Xie, P. H.; Hou, Y. J.; Zhang, B. W.; Cao, Y.; Wu, F.; Tian, W. J.; Shen, J. C., Spectroscopic and electrochemical properties of ruthenium(II) polypyridyl complexes. *J Chem Soc Dalton* **1999,** (23), 4217-4221.

223. Katz, M. J.; Brown, Z. J.; Colon, Y. J.; Siu, P. W.; Scheidt, K. A.; Snurr, R. Q.; Hupp, J. T.; Farha, O. K., A facile synthesis of UiO-66, UiO-67 and their derivatives. *Chem. Commun.* **2013,** *49* (82), 9449-9451.

224. Nickerl, G.; Leistner, M.; Helten, S.; Bon, V.; Senkovska, I.; Kaskel, S., Integration of accessible secondary metal sites into MOFs for H_2S removal. *Inorg Chem Front* **2014,** *1* (4), 325-330.

225. Galoisy, L.; Cormier, L.; Calas, G.; Briois, V., Environment of Ni, Co and Zn in low alkali borate glasses: information from EXAFS and XANES spectra. *J. Non-Cryst. Solids* **2001,** *293*, 105-111.

226. Wu, Z. Y.; Xian, D. C.; Hu, T. D.; Xie, Y. N.; Tao, Y.; Natoli, C. R.; Paris, E.; Marcelli, A., Quadrupolar transitions and medium-range-order effects in metal K-edge x-ray absorption spectra of 3d transition-metal compounds. *Phys. Rev. B* **2004,** *70* (3), 033104

227. Gonzalez, M. I.; Bloch, E. D.; Mason, J. A.; Teat, S. J.; Long, J. R., Single-Crystal-to-Single-Crystal Metalation of a Metal–Organic Framework: A Route toward Structurally Well-Defined Catalysts. *Inorg. Chem.* **2015,** *54* (6), 2995-3005.

228. Ravel, B.; Newville, M., ATHENA, ARTEMIS, HEPHAESTUS: data analysis for X-ray absorption spectroscopy using IFEFFIT. *J. Synchrotron Radiat.* **2005,** *12* (4), 537-541.

229. Bairu, S. G.; Mghanga, E.; Hasan, J.; Kola, S.; Rao, V. J.; Bhanuprakash, K.; Giribabu, L.; Wiederrecht, G. P.; da Silva, R.; Rego, L. G. C.; Ramakrishna, G., Ultrafast Interfacial Charge-Transfer Dynamics in a Donor-pi-Acceptor Chromophore Sensitized TiO2 Nanocomposite. *J. Phys. Chem. C* **2013,** *117* (9), 4824-4835.

230. Taira, N.; Saitoh, M.; Hashimoto, S.; Moon, H. R.; Yoon, K. B., Effect of electron-acceptor strength of zeolite on the luminescence decay rate of Ru(bpy)(3)(2+) incorporated within zeolites. *Photochem. Photobiol. Sci* **2006,** *5* (9), 822-827.

231. Aresta, M.; Dibenedetto, A.; Angelini, A., Catalysis for the Valorization of Exhaust Carbon: from CO2 to Chemicals, Materials, and Fuels. Technological Use of CO2. *Chem. Rev.* **2014,** *114* (3), 1709-1742.

232. Kim, D.; Sakimoto, K. K.; Hong, D. C.; Yang, P. D., Artificial Photosynthesis for Sustainable Fuel and Chemical Production. *Angew. Chem. Int. Ed.* **2015,** *54* (11), 3259-3266.

233. Sakakura, T.; Choi, J.-C.; Yasuda, H., Transformation of Carbon Dioxide. *Chem. Rev.* **2007,** *107* (6), 2365-2387.

234. Rakowski Dubois, M.; Dubois, D. L., Development of Molecular Electrocatalysts for CO2 Reduction and H2 Production/Oxidation. *Acc. Chem. Res.* **2009,** *42* (12), 1974-1982.

235. Berardi, S.; Drouet, S.; Francas, L.; Gimbert-Surinach, C.; Guttentag, M.; Richmond, C.; Stoll, T.; Llobet, A., Molecular artificial photosynthesis. *Chem. Soc. Rev.* **2014,** *43* (22), 7501-7519.

236. Kuehnel, M. F.; Orchard, K. L.; Dalle, K. E.; Reisner, E., Selective Photocatalytic CO2 Reduction in Water through Anchoring of a Molecular Ni Catalyst on CdS Nanocrystals. *J. Am. Chem. Soc.* **2017,** *139* (21), 7217-7223.

237. Fujita, E., Photochemical carbon dioxide reduction with metal complexes. *Coord. Chem. Rev.* **1999,** *185-6*, 373-384.

238. Ishida, H.; Tanaka, K.; Tanaka, T., Electrochemical CO2 reduction catalyzed by ruthenium complexes [Ru(bpy)2(CO)2]2+ and [Ru(bpy)2(CO)Cl]+. Effect of pH on the formation of CO and HCOO. *Organometallics* **1987,** *6* (1), 181-186.

239. Huckaba, A. J.; Sharpe, E. A.; Delcamp, J. H., Photocatalytic Reduction of CO2 with Re-Pyridyl-NHCs. *Inorg. Chem.* **2016,** *55* (2), 682-690.

240. Hayashi, Y.; Kita, S.; Brunschwig, B. S.; Fujita, E., Involvement of a

Binuclear Species with the Re−C(O)O−Re Moiety in CO2 Reduction Catalyzed by Tricarbonyl Rhenium(I) Complexes with Diimine Ligands: Strikingly Slow Formation of the Re−Re and Re−C(O)O−Re Species from Re(dmb)(CO)3S (dmb = 4,4‘-Dimethyl-2,2‘-bipyridine, S = Solvent). *J. Am. Chem. Soc.* **2003,** *125* (39), 11976-11987.

241. Kang, P.; Cheng, C.; Chen, Z.; Schauer, C. K.; Meyer, T. J.; Brookhart, M., Selective Electrocatalytic Reduction of CO2 to Formate by Water-Stable Iridium Dihydride Pincer Complexes. *J. Am. Chem. Soc.* **2012,** *134* (12), 5500-5503.

242. Hu, P.; Diskin-Posner, Y.; Ben-David, Y.; Milstein, D., Reusable Homogeneous Catalytic System for Hydrogen Production from Methanol and Water. *ACS Catal.* **2014,** *4* (8), 2649-2652.

243. Artero, V.; Chavarot-Kerlidou, M.; Fontecave, M., Splitting Water with Cobalt. *Angew. Chem. Int. Ed.* **2011,** *50* (32), 7238-7266.

244. Chi, J. Q.; Zeng, X. J.; Shang, X.; Dong, B.; Chai, Y. M.; Liu, C. G.; Marin, M.; Yin, Y. D., Embedding RhPx in N, P Co-Doped Carbon Nanoshells Through Synergetic Phosphorization and Pyrolysis for Efficient Hydrogen Evolution. *Adv. Funct. Mater.* **2019,** *29* (33), 11.

245. Jiao, L.; Seow, J. Y. R.; Skinner, W. S.; Wang, Z. U.; Jiang, H. L., Metal-organic frameworks: Structures and functional applications. *Mater. Today* **2019,** *27*, 43-68.

246. Wasson, M. C.; Lyu, J.; Islamoglu, T.; Farha, O. K., Linker Competition within a Metal–Organic Framework for Topological Insights. *Inorg. Chem.* **2019,** *58* (2), 1513-1517.

247. Yang, S.; Pattengale, B.; Lee, S.; Huang, J., Real-Time Visualization of Active Species in a Single-Site Metal–Organic Framework Photocatalyst. *ACS Energy Lett.* **2018,** *3* (3), 532-539.

248. Wang, C.; Xie, Z.; deKrafft, K. E.; Lin, W., Doping Metal–Organic Frameworks for Water Oxidation, Carbon Dioxide Reduction, and Organic Photocatalysis. *J. Am. Chem. Soc.* **2011,** *133* (34), 13445-13454.

249. Dhakshinamoorthy, A.; Li, Z. H.; Garcia, H., Catalysis and photocatalysis by metal organic frameworks. *Chem. Soc. Rev.* **2018,** *47* (22), 8134-8172.

250. Xiao, J.-D.; Jiang, H.-L., Metal–Organic Frameworks for Photocatalysis and Photothermal Catalysis. *Acc. Chem. Res.* **2019,** *52* (2), 356-366.

251. Fei, H.; Sampson, M. D.; Lee, Y.; Kubiak, C. P.; Cohen, S. M., Photocatalytic CO2 Reduction to Formate Using a Mn(I) Molecular Catalyst in a Robust Metal–Organic Framework. *Inorg. Chem.* **2015,** *54* (14), 6821-6828.

252. Kornienko, N.; Zhao, Y.; Kley, C. S.; Zhu, C.; Kim, D.; Lin, S.; Chang, C. J.; Yaghi, O. M.; Yang, P., Metal–Organic Frameworks for Electrocatalytic Reduction of Carbon Dioxide. *J. Am. Chem. Soc.* **2015,** *137* (44), 14129-14135.

253. Li, R.; Zhang, W.; Zhou, K., Metal-Organic-Framework-Based Catalysts for Photoreduction of CO2. *Adv. Mater.* **2018,** *30* (35), 31.

254. Shakya, D. M.; Ejegbavwo, O. A.; Rajeshkumar, T.; Senanayake, S. D.; Brandt, A. J.; Farzandh, S.; Acharya, N.; Ebrahim, A. M.; Frenkel, A. I.; Rui, N.; Tate, G. L.; Monnier, J. R.; Vogiatzis, K. D.; Shustova, N. B.; Chen, D. A., Selective Catalytic Chemistry at Rhodium(II) Nodes in Bimetallic Metal–Organic Frameworks. *Angew. Chem. Int. Ed.* **2019,** *58* (46), 16533-16537.

255. Rice, A. M.; Leith, G. A.; Ejegbavwo, O. A.; Dolgopolova, E. A.; Shustova, N. B., Heterometallic Metal–Organic Frameworks (MOFs): The Advent of Improving the Energy Landscape. *ACS Energy Lett.* **2019,** *4* (8), 1938-1946.

256. Usov, P. M.; Ahrenholtz, S. R.; Maza, W. A.; Stratakes, B.; Epley, C. C.; Kessinger, M. C.; Zhu, J.; Morris, A. J., Cooperative electrochemical water oxidation by Zr nodes and Ni-porphyrin linkers of a PCN-224 MOF thin film. *J. Mater. Chem. A* **2016,** *4* (43), 16818-16823.

257. Otake, K.-i.; Ye, J.; Mandal, M.; Islamoglu, T.; Buru, C. T.; Hupp, J. T.; Delferro, M.; Truhlar, D. G.; Cramer, C. J.; Farha, O. K., Enhanced Activity of Heterogeneous Pd(II) Catalysts on Acid-Functionalized Metal–Organic Frameworks. *ACS Catal.* **2019,** *9* (6), 5383-5390.

258. Hanna, L.; Kucheryavy, P.; Liu, C.; Zhang, X.; Lockard, J. V., Long-Lived Photoinduced Charge Separation in a Trinuclear Iron-μ3-oxo-based Metal–Organic Framework. *J. Phys. Chem. C* **2017,** *121* (25), 13570-13576.

259. Shaikh, S. M.; Chakraborty, A.; Alatis, J.; Cai, M.; Danilov, E.; Morris, A. J., Light harvesting and energy transfer in a porphyrin-based metal organic framework. *Faraday Discuss.* **2019,** *216*, 174-190.

260. Rhauderwiek, T.; Heidenreich, N.; Reinsch, H.; Oien-Odegaard, S.; Lomachenko, K. A.; Rutt, U.; Soldatov, A. V.; Lillerud, K. P.; Stock, N., Co-Ligand Dependent Formation and Phase Transformation of Four Porphyrin-Based Cerium Metal-Organic Frameworks. *Cryst. Growth Des.* **2017,** *17* (6), 3462-3474.

261. Rahimi, R.; Shariatinia, S.; Zargari, S.; Berijani, M. Y.; Ghaffarinejad, A.; Shojaie, Z. S., Synthesis, characterization, and photocurrent generation of a new nanocomposite based Cu-TCPP MOF and ZnO nanorod. *RSC Adv.* **2015,** *5* (58), 46624-46631.

262. Liu, J. X.; Zhou, W. C.; Liu, J. X.; Fujimori, Y.; Higashino, T.; Imahori, H.; Jiang, X.; Zhao, J. J.; Sakurai, T.; Hattori, Y.; Matsuda, W.; Seki, S.; Garlapati, S. K.; Dasgupta, S.; Redel, E.; Sunag, L. C.; Woll, C., A new class of epitaxial porphyrin metal-organic framework thin films with extremely high photocarrier generation efficiency: promising materials for all-solid-state solar cells. *J. Mater. Chem. A* **2016,** *4* (33), 12739-12747.

263. Lin, A.; Ibrahim, A. A.; Arab, P.; El-Kaderi, H. M.; El-Shall, M. S., Palladium Nanoparticles Supported on Ce-Metal-Organic Framework for Efficient CO Oxidation and Low-Temperature CO2 Capture. *ACS Appl. Mater. Interfaces.* **2017,** *9* (21), 17961-17968.

264. Sugimoto, T.; Joseph, B.; Paris, E.; Iadecola, A.; Mizokawa, T.; Demura, S.; Mizuguchi, Y.; Takano, Y.; Saini, N. L., Role of the Ce valence in the coexistence of superconductivity and ferromagnetism of CeO1-xFxBiS2 revealed by Ce L-3-edge x-ray absorption spectroscopy. *Phys. Rev. B* **2014,** *89* (20).

265. Jacobs, G.; Patterson, P. M.; Williams, L.; Chenu, E.; Sparks, D.; Thomas, G.; Davis, B. H., Water-gas shift: in situ spectroscopic studies of noble metal promoted ceria catalysts for CO removal in fuel cell reformers and mechanistic implications. *Appl. Catal. A-Gen.* **2004,** *262* (2), 177-187.

266. Thole, B. T.; Vanderlaan, G.; Fuggle, J. C.; Sawatzky, G. A.; Karnatak, R. C.; Esteva, J. M., 3D X-RAY-ABSORPTION LINES AND THE 3D94FN+1 MULTIPLETS OF THE LANTHANIDES. *Phys. Rev. B* **1985,** *32* (8), 5107-5118.

267. Matsuyama, H.; Harada, I.; Kotani, A., Roles of 4f-5d exchange interactions in magnetic circular X-ray dichroism at the rare-earth L(2,3) edges. *J. Phys. Soc. Jpn.* **1997,** *66* (2), 337-340.

268. Kotani, A.; Kvashnina, K. O.; Glatzel, P.; Parlebas, J. C.; Schmerber, G., Single Impurity Anderson Model versus Density Functional Theory for Describing Ce L-3 X-Ray Absorption Spectra of CeFe2: Resolution of a Recent Controversy. *Phys. Rev. Lett.* **2012,** *108* (3), 5.

269. Mathey, L.; Paul, M.; Coperet, C.; Tsurugi, H.; Mashima, K., Cerium(IV) Hexanuclear Clusters from Cerium(III) Precursors: Molecular Models for Oxidative Growth of Ceria Nanoparticles. *Chem. Eur. J.* **2015,** *21* (38), 13454-13461.

270. Das, R.; Sarma, R.; Baruah, J. B., A hexanuclear cerium(IV) cluster with mixed coordination environment. *Inorg. Chem. Commun.* **2010,** *13* (6), 793-795.

271. Baskin, J. S.; Yu, H. Z.; Zewail, A. H., Ultrafast dynamics of Porphyrins in the condensed phase: I. Free base tetraphenylporphyrin. *J. Phys. Chem A* **2002,** *106* (42), 9837-9844.

272. Venkatesh, Y.; Venkatesan, M.; Ramakrishna, B.; Bangal, P. R., Ultrafast Time-Resolved Emission and Absorption Spectra of meso-Pyridyl Porphyrins upon Soret Band Excitation Studied by Fluorescence Up-Conversion and Transient Absorption Spectroscopy. *J. Phys. Chem B* **2016,** *120* (35), 9410-9421.

273. Kumar, P. H.; Venkatesh, Y.; Siva, D.; Ramakrishna, B.; Bangal, P. R., Ultrafast Relaxation Dynamics of 5,10,15,20-meso-Tetrakis Pentafluorophenyl Porphyrin Studied by Fluorescence Up-Conversion and Transient Absorption Spectroscopy. *J. Phys. Chem A* **2015,** *119* (8), 1267-1278.

274. McCarthy, B. D.; Hontz, E. R.; Yost, S. R.; Van Voorhis, T.; Dincă, M., Charge Transfer or J-Coupling? Assignment of an Unexpected Red-Shifted Absorption Band in a Naphthalenediimide-Based Metal–Organic Framework. *The J. Phys. Chem L* **2013,** *4* (3), 453-458.

275. Takashima, Y.; Furukawa, S.; Kitagawa, S., Control of the charge-transfer interaction between a flexible porous coordination host and aromatic guests by framework isomerism. *Crystengcomm* **2011,** *13* (10), 3360-3363.

276. Parusel, A. B. J.; Wondimagegn, T.; Ghosh, A., Do Nonplanar Porphyrins Have Red-Shifted Electronic Spectra? A DFT/SCI Study and Reinvestigation of a Recent Proposal. *J. Am. Chem. Soc.* **2000,** *122* (27), 6371-6374.

277. Haddad, R. E.; Gazeau, S.; Pecaut, J.; Marchon, J. C.; Medforth, C. J.; Shelnutt, J. A., Origin of the red shifts in the optical absorption bands of nonplanar tetraalkylporphyrins. *J. Am. Chem. Soc.* **2003,** *125* (5), 1253-1268.

278. Li, X. X.; Gong, C. H.; Gurzadyan, G. G.; Gelin, M. F.; Liu, J. X.; Sun, L. C., Ultrafast Relaxation Dynamics in Zinc Tetraphenylporphyrin Surface-Mounted Metal Organic Framework. *J. Phys. Chem C* **2018,** *122* (1), 50-61.

279. Harriman, A., LUMINESCENCE OF PORPHYRINS AND METALLOPORPHYRINS .3. HEAVY-ATOM EFFECTS. *J. Chem. Soc. Faraday Trans.* **1981,** *77*, 1281-1291.

280. Journal of Physical Chemistry CKalyanasundaram, K.; Neumannspallart, M., Photophysical and Redox Properties of Water-Soluble Porphyrins in Aqueous Media.

J. Phys. Chem. **1982,** *86* (26), 5163-5169.

281. Neta, P., ONE-ELECTRON TRANSFER-REACTIONS INVOLVING ZINC AND COBALT PORPHYRINS IN AQUEOUS-SOLUTIONS. *J. Phys. Chem.* **1981,** *85* (24), 3678-3684.

282. Keane, P. M.; Kelly, J. M., Triplet-state Dynamics of a Metalloporphyrin Photosensitiser (PtTMPyP4) in the Presence of Halides and Purine Mononucleotides. *Photochem. Photobiol. Sci* **2011,** *10* (10), 1578-1586.

283. Arcudi, F.; Strauss, V.; Dordevic, L.; Cadranel, A.; Guldi, D. M.; Prato, M., Porphyrin Antennas on Carbon Nanodots: Excited State Energy and Electron Transduction. *Angew. Chem. Int. Ed.* **2017,** *56* (40), 12097-12101.

284. Gutierrez, M.; Cohen, B.; Sanchez, F.; Douhal, A., Photochemistry of Zr-based MOFs: ligand-to-cluster charge transfer, energy transfer and excimer formation, what else is there? *Phys. Chem. Chem. Phys.* **2016,** *18* (40), 27761-27774.

285. Inoue, T.; Fujishima, A.; Konishi, S.; Honda, K., Photoelectrocatalytic Reduction of Carbon-Dioxide in Aqueous Suspensions of Semiconductor Powders. *Nature* **1979,** *277* (5698), 637-638.

286. D'Alessandro, D. M.; Smit, B.; Long, J. R., Carbon Dioxide Capture: Prospects for New Materials. *Angew. Chem. Int. Ed.* **2010,** *49* (35), 6058-6082.

287. Appel, A. M.; Bercaw, J. E.; Bocarsly, A. B.; Dobbek, H.; DuBois, D. L.; Dupuis, M.; Ferry, J. G.; Fujita, E.; Hille, R.; Kenis, P. J. A.; Kerfeld, C. A.; Morris, R. H.; Peden, C. H. F.; Portis, A. R.; Ragsdale, S. W.; Rauchfuss, T. B.; Reek, J. N. H.; Seefeldt, L. C.; Thauer, R. K.; Waldrop, G. L., Frontiers, Opportunities, and Challenges in Biochemical and Chemical Catalysis of CO2 Fixation. *Chem. Rev.* **2013,** *113* (8), 6621-6658.

288. Thoi, V. S.; Kornienko, N.; Margarit, C. G.; Yang, P. D.; Chang, C. J., Visible-Light Photoredox Catalysis: Selective Reduction of Carbon Dioxide to Carbon Monoxide by a Nickel N-Heterocyclic Carbene-Isoquinoline Complex. *J. Am. Chem. Soc.* **2013,** *135* (38), 14413-14424.

289. Barton, E. E.; Rampulla, D. M.; Bocarsly, A. B., Selective solar-driven reduction of CO2 to methanol using a catalyzed p-GaP based photoelectrochemical cell. *J. Am. Chem. Soc.* **2008,** *130* (20), 6342-+.

290. Smieja, J. M.; Benson, E. E.; Kumar, B.; Grice, K. A.; Seu, C. S.; Miller, A. J. M.; Mayer, J. M.; Kubiak, C. P., Kinetic and structural studies, origins of selectivity, and interfacial charge transfer in the artificial photosynthesis of CO. *Proc. Natl. Acad.*

Sci. U. S. A. **2012,** *109* (39), 15646-15650.

291. Wang, S. B.; Wang, X. C., Imidazolium Ionic Liquids, Imidazolylidene Heterocyclic Carbenes, and Zeolitic Imidazolate Frameworks for CO2 Capture and Photochemical Reduction. *Angew. Chem. Int. Ed.* **2016,** *55* (7), 2308-2320.

292. Diercks, C. S.; Yaghi, O. M., The atom, the molecule, and the covalent organic framework. *Science* **2017,** *355* (6328), 923-+.

293. Waller, P. J.; Gandara, F.; Yaghi, O. M., Chemistry of Covalent Organic Frameworks. ***Acc****. Chem. Res.* **2015,** *48* (12), 3053-3063.

294. Bessinger, D.; Ascherl, L.; Auras, F.; Bein, T., Spectrally Switchable Photodetection with Near-Infrared-Absorbing Covalent Organic Frameworks. *J. Am. Chem. Soc.* **2017,** *139* (34), 12035-12042.

295. Keller, N.; Bessinger, D.; Reuter, S.; Calik, M.; Ascherl, L.; Hanusch, F. C.; Auras, F.; Bein, T., Oligothiophene-Bridged Conjugated Covalent Organic Frameworks. *J. Am. Chem. Soc.* **2017,** *139* (24), 8194-8199.

296. Dalapati, S.; Jin, E. Q.; Addicoat, M.; Heine, T.; Jiang, D. L., Highly Emissive Covalent Organic Frameworks. *J. Am. Chem. Soc.* **2016,** *138* (18), 5797-5800.

297. Wan, S.; Gandara, F.; Asano, A.; Furukawa, H.; Saeki, A.; Dey, S. K.; Liao, L.; Ambrogio, M. W.; Botros, Y. Y.; Duan, X. F.; Seki, S.; Stoddart, J. F.; Yaghi, O. M., Covalent Organic Frameworks with High Charge Carrier Mobility. *Chem. Mater.* **2011,** *23* (18), 4094-4097.

298. Patra, B. C.; Khilari, S.; Manna, R. N.; Mondal, S.; Pradhan, D.; Pradhan, A.; Bhaumik, A., A Metal-Free Covalent Organic Polymer for Electrocatalytic Hydrogen Evolution. *ACS Catal.* **2017,** *7* (9), 6120-6127.

299. Ma, T. Q.; Kapustin, E. A.; Yin, S. X.; Liang, L.; Zhou, Z. Y.; Niu, J.; Li, L. H.; Wang, Y. Y.; Su, J.; Li, J.; Wang, X. G.; Wang, W. D.; Wang, W.; Sun, J. L.; Yaghi, O. M., Single-crystal x-ray diffraction structures of covalent organic frameworks. *Science* **2018,** *361* (6397), 48-52.

300. Ding, S. Y.; Dong, M.; Wang, Y. W.; Chen, Y. T.; Wang, H. Z.; Su, C. Y.; Wang, W., Thioether-Based Fluorescent Covalent Organic Framework for Selective Detection and Facile Removal of Mercury(II). *J. Am. Chem. Soc.* **2016,** *138* (9), 3031-3037.

301. Jin, E. Q.; Asada, M.; Xu, Q.; Dalapati, S.; Addicoat, M. A.; Brady, M. A.;

Xu, H.; Nakamura, T.; Heine, T.; Chen, Q. H.; Jiang, D. L., Two-dimensional sp(2) carbon-conjugated covalent organic frameworks. *Science* **2017,** *357* (6352), 673-676.

302. Huang, N.; Wang, P.; Jiang, D. L., Covalent organic frameworks: a materials platform for structural and functional designs. *Nat Rev Mater* **2016,** *1* (10).

303. Lin, S.; Diercks, C. S.; Zhang, Y. B.; Kornienko, N.; Nichols, E. M.; Zhao, Y. B.; Paris, A. R.; Kim, D.; Yang, P.; Yaghi, O. M.; Chang, C. J., Covalent organic frameworks comprising cobalt porphyrins for catalytic CO2 reduction in water. *Science* **2015,** *349* (6253), 1208-1213.

304. Yadav, R. K.; Kumar, A.; Park, N. J.; Kong, K. J.; Baeg, J. O., A highly efficient covalent organic framework film photocatalyst for selective solar fuel production from CO2. *J. Mater. Chem. A* **2016,** *4* (24), 9413-9418.

305. Nagai, A.; Chen, X.; Feng, X.; Ding, X. S.; Guo, Z. Q.; Jiang, D. L., A Squaraine-Linked Mesoporous Covalent Organic Framework. *Angew. Chem. Int. Ed.* **2013,** *52* (13), 3770-3774.

306. Chen, X.; Addicoat, M.; Jin, E. Q.; Zhai, L. P.; Xu, H.; Huang, N.; Guo, Z. Q.; Liu, L. L.; Irle, S.; Jiang, D. L., Locking Covalent Organic Frameworks with Hydrogen Bonds: General and Remarkable Effects on Crystalline Structure, Physical Properties, and Photochemical Activity. *J. Am. Chem. Soc.* **2015,** *137* (9), 3241-3247.

307. Banerjee, T.; Gottschling, K.; Savasci, G.; Ochsenfeld, C.; Lotsch, B. V., H2 Evolution with Covalent Organic Framework Photocatalysts. *ACS Energy Lett.* **2018,** *3*, 400-409.

308. Banerjee, T.; Haase, F.; Savasci, G.; Gottschling, K.; Ochsenfeld, C.; Lotsch, B. V., Single-Site Photocatalytic H-2 Evolution from Covalent Organic Frameworks with Molecular Cobaloxime Co-Catalysts. *J. Am. Chem. Soc.* **2017,** *139* (45), 16228-16234.

309. Lin, C. Y.; Zhang, D. T.; Zhao, Z. H.; Xia, Z. H., Covalent Organic Framework Electrocatalysts for Clean Energy Conversion. *Adv. Mater.* **2018,** *30* (5), 16.

310. Pachfule, P.; Acharjya, A.; Roeser, J.; Langenhahn, T.; Schwarze, M.; Schomacker, R.; Thomas, A.; Schmidt, J., Diacetylene Functionalized Covalent Organic Framework (COF) for Photocatalytic Hydrogen Generation. *J. Am. Chem. Soc.* **2018,** *140* (4), 1423-1427.

311.Sick, T.; Hufnagel, A. G.; Kampmann, J.; Kondofersky, I.; Calik, M.; Rotter, J. M.; Evans, A.; Doblinger, M.; Herbert, S.; Peters, K.; Bohm, D.; Knochel, P.; Medina,

D. D.; Fattakhova-Rohlfing, D.; Bein, T., Oriented Films of Conjugated 2D Covalent Organic Frameworks as Photocathodes for Water Splitting. *J. Am. Chem. Soc.* **2018,** *140* (6), 2085-2092.

312. Ding, S. Y.; Gao, J.; Wang, Q.; Zhang, Y.; Song, W. G.; Su, C. Y.; Wang, W., Construction of Covalent Organic Framework for Catalysis: Pd/COF-LZU1 in Suzuki-Miyaura Coupling Reaction. *J. Am. Chem. Soc.* **2011,** *133* (49), 19816-19822.

313. Lin, G. Q.; Ding, H. M.; Chen, R. F.; Peng, Z. K.; Wang, B. S.; Wang, C., 3D Porphyrin-Based Covalent Organic Frameworks. *J. Am. Chem. Soc.* **2017,** *139* (25), 8705-8709.

314. Stegbauer, L.; Schwinghammer, K.; Lotsch, B. V., A hydrazone-based covalent organic framework for photocatalytic hydrogen production. *Chem. Sci.* **2014,** *5* (7), 2789-2793.

315. Qian, H. L.; Dai, C.; Yang, C. X.; Yan, X. P., High-Crystallinity Covalent Organic Framework with Dual Fluorescence Emissions and Its Ratiometric Sensing Application. *ACS Appl. Mater. Interfaces* **2017,** *9* (29), 24999-25005.

316. Cho, Y. J.; Lee, A. R.; Kim, S. Y.; Cho, M. J.; Han, W. S.; Son, H. J.; Cho, D. W.; Kang, S. O., The influence of pi-conjugation on competitive pathways: charge transfer or electron transfer in new D-pi-A and D-pi-Si-pi-A dyads. *Phys. Chem. Chem. Phys.* **2016,** *18* (33), 22921-22928.

317. Pop, F.; Riobe, F.; Seifert, S.; Cauchy, T.; Ding, J.; Dupont, N.; Hauser, A.; Koch, M.; Avarvari, N., Tetrathiafulvalene-1,3,5-triazines as (Multi)Donor-Acceptor Systems with Tunable Charge Transfer: Structural, Photophysical, and Theoretical Investigations. *Inorg. Chem.* **2013,** *52* (9), 5023-5034.

318. Smieja, J. M.; Kubiak, C. P., Re(bipy-tBu)(CO)(3)Cl-improved Catalytic Activity for Reduction of Carbon Dioxide: IR-Spectroelectrochemical and Mechanistic Studies. *Inorg. Chem.* **2010,** *49* (20), 9283-9289.

319. Hayashi, Y.; Kita, S.; Brunschwig, B. S.; Fujita, E., Involvement of a binuclear species with the Re-C(O)O-Re moiety in CO2 reduction catalyzed by tricarbonyl rhenium(I) complexes with diimine ligands: Strikingly slow formation of the Re-Re and Re-C(O)O-Re species from Re(dmb)(CO)(3)S (dmb=4,4 '-dimethyl-2,2 '-bipyridine, S = solvent). *J. Am. Chem. Soc.* **2003,** *125* (39), 11976-11987.

320. Nganga, J. K.; Samanamu, C. R.; Tanski, J. M.; Pacheco, C.; Saucedo, C.; Batista, V. S.; Grice, K. A.; Ertem, M. Z.; Angeles-Boza, A. M., Electrochemical Reduction of CO2 Catalyzed by Re(pyridine-oxazoline)(CO)(3)Cl Complexes. *Inorg. Chem.* **2017,** *56* (6), 3214-3226.

321. Qiao, X. X.; Li, Q. Q.; Schaugaard, R. N.; Noffke, B. W.; Liu, Y. J.; Li, D. P.; Liu, L.; Raghavachari, K.; Li, L. S., Well-Defined Nanographene-Rhenium Complex as an Efficient Electrocatalyst and Photocatalyst for Selective CO_2 Reduction. *J. Am. Chem. Soc.* **2017,** *139* (11), 3934-3937.

322. Wang, Y. C.; Jiang, Y. H.; Hua, J. L.; Tian, H.; Qian, S. X., Optical Limiting Properties and Ultrafast Dynamics of Six-branched Styryl Derivatives Based on 1,3,5-triazine. *J. Appl. Phys.* **2011,** *110* (3).

323. Wang, Y. C.; Yin, S. H.; Liu, J. Y.; Yao, L.; Wang, G. Q.; Liu, D. J.; Jing, B.; Cheng, L. H.; Zhong, H. Y.; Shi, X. R.; Fang, Q.; Qian, S. X., Probing Ultrafast Excited State Dynamics and Nonlinear Absorption Properties of Three Star-shaped Conjugated Oligomers with 1,3,5-triazine Core. *RSC Adv.* **2014,** *4* (21), 10960-10967.

324. Zhou, Z. N.; Zhou, X. Y.; Wang, X. L.; Jiang, B.; Li, Y. L.; Chen, J. Q.; Xu, J. H., Ultrafast Excited-State Dynamics of Cytosine Aza-Derivative and Analogues. *J. Phys. Chem. A* **2017,** *121* (14), 2780-2789.

325. Zalis, S.; Milne, C. J.; El Nahhas, A.; Blanco-Rodriguez, A. M.; van der Veen, R. M.; Vlcek, A., Re and Br X-ray Absorption Near-Edge Structure Study of the Ground and Excited States of [ReBr(CO)(3)(bpy)] Interpreted by DFT and TD-DFT Calculations. *Inorg. Chem.* **2013,** *52* (10), 5775-5785.

326. El Nahhas, A.; van der Veen, R. M.; Penfold, T. J.; Pham, V. T.; Lima, F. A.; Abela, R.; Blanco-Rodriguez, A. M.; Zalis, S.; Vlcek, A.; Tavernelli, I.; Rothlisberger, U.; Milne, C. J.; Chergui, M., X-ray Absorption Spectroscopy of Ground and Excited Rhenium-Carbonyl Diimine-Complexes: Evidence for a Two-Center Electron Transfer. *J. Phys. Chem. A* **2013,** *117* (2), 361-369.

327. Choi, K. M.; Kim, D.; Rungtaweevoranit, B.; Trickett, C. A.; Barmanbek, J. T. D.; Alshammari, A. S.; Yang, P. D.; Yaghi, O. M., Plasmon-Enhanced PhotoCatalytic CO_2 Conversion within Metal Organic Frameworks under Visible Light. *J. Am. Chem. Soc.* **2017,** *139* (1), 356-362.

328. Abdellah, M.; El-Zohry, A. M.; Antila, L. J.; Windle, C. D.; Reisner, E.; Hammarstrom, L., Time-Resolved IR Spectroscopy Reveals a. Mechanism with TiO2 as a Reversible Electron Acceptor in a TiO_2-Re Catalyst System for CO2 Photoreduction. *J. Am. Chem. Soc.* **2017,** *139* (3), 1226-1232.